National Library
of Canada

Acquisitions and
Bibliographic Services Branch

395 Wellington Street
Ottawa, Ontario
K1A 0N4

Bibliothèque nationale
du Canada

Direction des acquisitions et
des services bibliographiques

395, rue Wellington
Ottawa (Ontario)
K1A 0N4

Your file Votre référence

Our file Notre référence

NOTICE

The quality of this microform is heavily dependent upon the quality of the original thesis submitted for microfilming. Every effort has been made to ensure the highest quality of reproduction possible.

If pages are missing, contact the university which granted the degree.

Some pages may have indistinct print especially if the original pages were typed with a poor typewriter ribbon or if the university sent us an inferior photocopy.

Reproduction in full or in part of this microform is governed by the Canadian Copyright Act, R.S.C. 1970, c. C-30, and subsequent amendments.

AVIS

La qualité de cette microforme dépend grandement de la qualité de la thèse soumise au microfilmage. Nous avons tout fait pour assurer une qualité supérieure de reproduction.

S'il manque des pages, veuillez communiquer avec l'université qui a conféré le grade.

La qualité d'impression de certaines pages peut laisser à désirer, surtout si les pages originales ont été dactylographiées à l'aide d'un ruban usé ou si l'université nous a fait parvenir une photocopie de qualité inférieure.

La reproduction, même partielle, de cette microforme est soumise à la Loi canadienne sur le droit d'auteur, SRC 1970, c. C-30, et ses amendements subséquents.

Canada

An NMR Study of Human Brain Tumours:
Phosphorus Chemical Shift Imaging *in vivo*
and
High Resolution Proton Spectroscopy of Biopsy Samples

Allison Rutter, B.Sc., M.Sc.

National Library
of Canada

Acquisitions and
Bibliographic Services Branch

395 Wellington Street
Ottawa, Ontario
K1A 0N4

Bibliothèque nationale
du Canada

Direction des acquisitions et
des services bibliographiques

395, rue Wellington
Ottawa (Ontario)
K1A 0N4

Your file Votre référence

Our file Notre référence

ISBN 0-315-95989-4

Acknowledgements

I would like thank my supervisor, Ian C. P. Smith, for his guidance and his enthusiasm. I am also grateful for the help and encouragement of John Saunders. I would like to thank Herman Hugenholtz for providing the brain tumour samples. There are too many people to name at NRC and Ottawa U. who have made these past four and a half years memorable. I will only mention Dave Wilkins with whom I shared an office and Annette Kuesel who among many other things read this thesis. Finally, and most importantly, I want to thank my partner, Ira, whose patience and encouragement made this thesis possible.

Abstract

Human brain tumours have been investigated using proton and phosphorus nuclear magnetic resonance (NMR). The localization technique, chemical shift imaging has been used to obtain phosphorus spectra of tumours in vivo. High resolution proton spectroscopy has been performed on biopsy samples and extracts of human brain tumours.

To obtain the localized phosphorus spectra, one dimensional chemical shift imaging with a surface coil was adapted to a 1.5 T Siemens Magnetom imager. The ratios of areas, PDE/ATP and PME/ATP were found to be higher in glioblastomas and astrocytomas than in normal brain. Pi/ATP and PCr/ATP were also high in astrocytomas. The pH of brain tumours ranged from alkaline to neutral, with meningiomas consistently having alkaline pH. A three dimensional localization sequence was written and tested on the Magnetom and used to obtain phosphorus spectra from the brains of normal volunteers.

One dimensional ^1H spectra, COSY spectra and T_2 data were obtained from ex vivo biopsy samples. A parameter, P, was defined as the ratio of the area between 3.4 and 3.1 ppm over the area between 1.5 ppm and 1.1 ppm. The parameter

distinguished glioblastomas from astrocytomas and normal brain. This area parameter, P, also appeared to be indicative of malignant potential or biological aggressiveness. Crosspeaks in the ex vivo proton COSY spectra of brain specimens could be used to classify glioblastomas, astrocytomas, metastases to the brain, meningiomas and normal brain in agreement with histopathological diagnosis. The T_2 values at 1.3 ppm were fitted to a two exponential equation. The longer component could be used to separate clearly glioblastomas from normal brain, normal brain having a much longer long T_2 component. Astrocytomas formed a continuum of values between glioblastomas and normal brain, with the grade of the astrocytoma roughly correlating with the value of the long T_2 component.

High resolution ^1H spectroscopy of perchloric acid extracts of biopsy samples was performed. The extracts confirmed that lactate, acetate, creatine and choline derivatives, NAA, glutamate, glutamine, alanine, valine and leucine were present in the samples. Comparisons of extract and ex vivo spectra indicated that the 1.3 ppm peak in the ex vivo spectra is predominantly due to the methylene moiety of lipids.

Table of Contents

Chapter 1

Chapter 2

Chapter 3

Chapter 4

Chapter 5

Chapter 6

Chapter 7

Chapter 8

Chapter 9

List of Figures

List of Tables

Abbreviations

NMR	nuclear magnetic resonance spectroscopy
MRI	magnetic resonance imaging
CPMG	Carr-Purcell-Meiboom-Gill pulse sequence
T_1	longitudinal relaxation time constant
T_2	transverse relaxation time constant
COSY	correlated spectroscopy
Pi	inorganic phosphate
PME	phosphomonoesters
PDE	phosphodiesters
PCr	phosphocreatine
ppm	parts per million
CSI	chemical shift imaging
ISIS	image selective in vivo spectroscopy
NAA	N-acetyl-aspartate
PPA	phenylphosphonic acid
DMMP	dimethylmethylphosphonate
CT	computed tomography
o.d.	outer diameter
PBS-D_2O	Dulbecco's phosphate-buffered saline in D_2O

CHAPTER 1

General Introduction

Cancer of the brain is a disease which continues to be lethal despite advances in many fields of medicine. Survival time is only marginally improved and malignant brain tumours are lethal in essentially all cases. Within this scenario, any technique which can yield more information and possibly aid in diagnosis is welcome. Nuclear magnetic resonance imaging has been shown to be of significant value in diagnosis and planning of treatment. This thesis is concerned with nuclear magnetic resonance spectroscopy. It too has shown potential for aiding in diagnosis and treatment planning. It is hoped that the research in this thesis will be a small step towards 1) a greater understanding of this disease (1, 2), 2) the elimination of invasive biopsies (3, 4) and 3) the improvement of diagnosis (5, 6).

1.1 Brain Neoplasms

Despite many advances, the outlook for a patient diagnosed with a brain tumour in the 1990's is gloomy. Happily, however, much progress has been made since the first documented craniotomy and excision of a glioma in 1884. The patient died 4 weeks later and for a number of years thereafter, glioma patients were treated for syphilis (thought at that time to be the cause) (7). Treatment today often includes surgical excision, radiotherapy and chemotherapy. Figure 1.1 (8) is compiled from a literature survey of studies reporting survival times for glioblastomas, the most malignant form of glioma. The mean survival time in months is plotted versus the year the study was performed. The plot represents 4381 cases; the mean survival rate after 1975 was 10.3 months and prior to 1975 was 6.6 months. The increase in survival time is due in part to the increase in chemotherapy and radiotherapy. In a 1969 study, surgery followed by combined radiotherapy and chemotherapy extended survival from 14 weeks (supportive care only) to 35 weeks (9). While the increase in survival time is promising, clearly more research is needed.

The incidence of primary central nervous system tumours is between 1/100,000 and 8/100,000. There appears to be a slightly higher incidence in men versus women; in a Finnish study of 3857 patients, 2100 were men and 1757 were women (10). Primary brain tumours are not a disease of the aged. Figure 1.2 illustrates the distribution by age and sex of incidences of glioblastomas and anaplastic astrocytomas (11). Note that the anaplastic astrocytoma, a slightly less

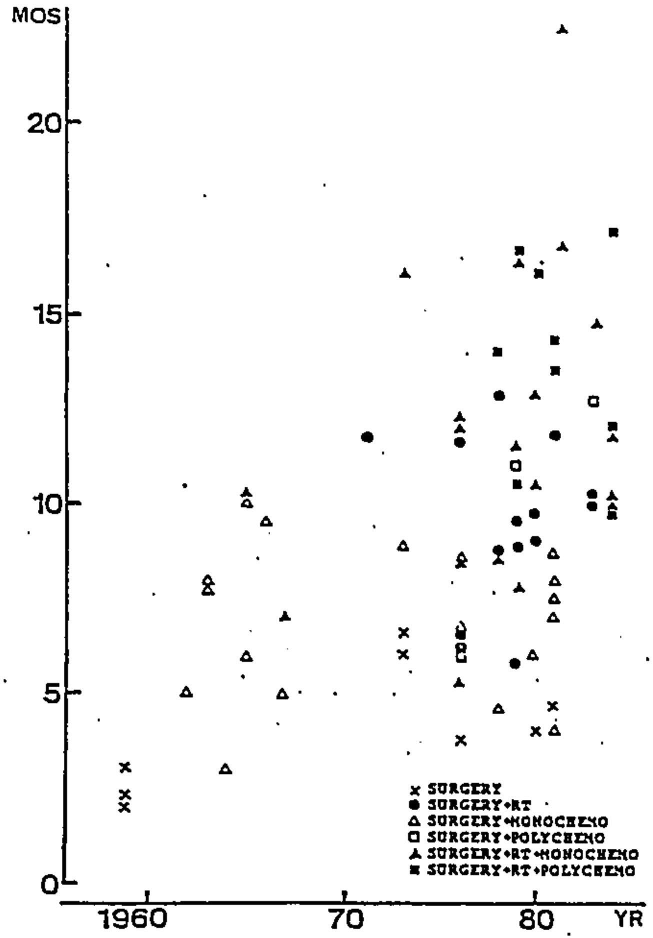

Figure 1.1: Data compiled from a literature survey of studies reporting survival times for glioblastomas. The mean survival time in months is plotted versus the year the study was performed. The plot represents 4381 cases. (taken from reference 8). (RT = radiotherapy treatment; MONOCHEMO = treatment with one chemotherapeutic; POLYCHEMO = treatment with multiple chemotherapeutics)

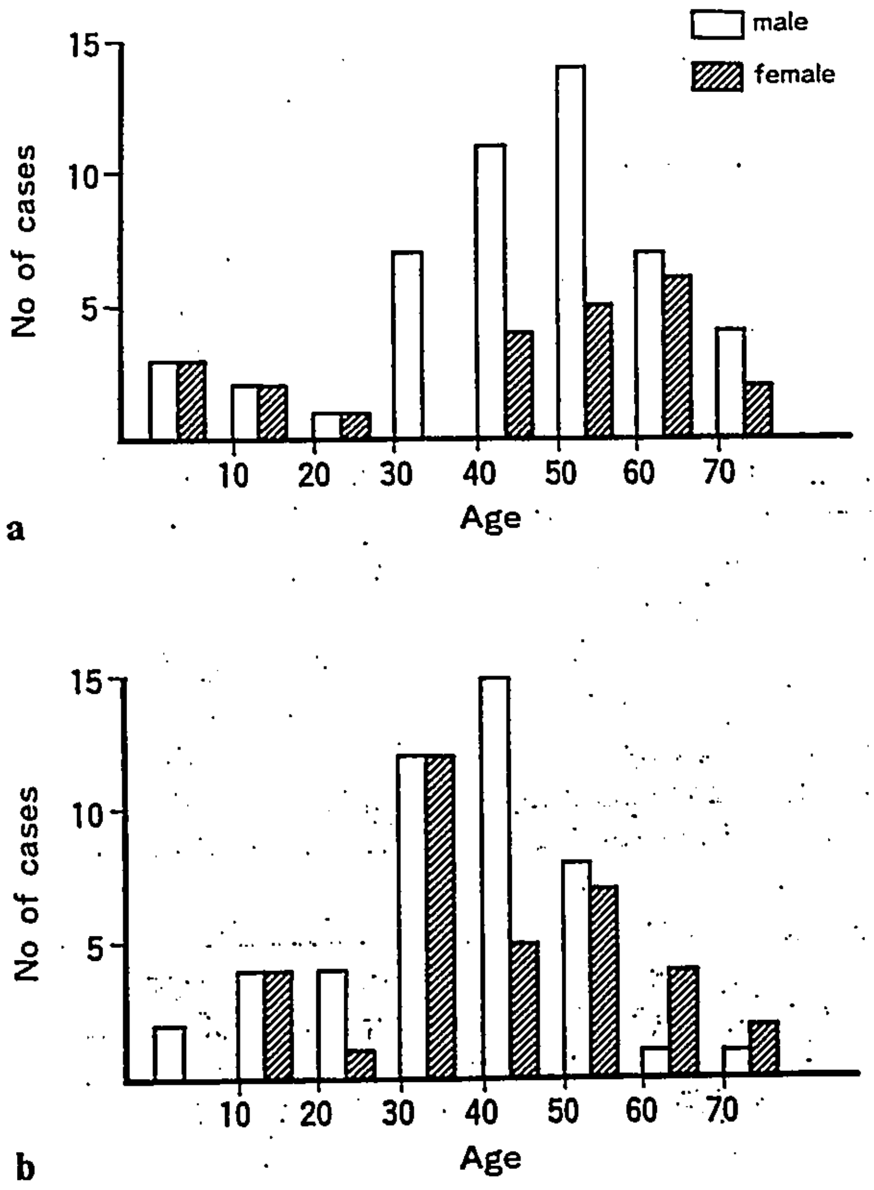

Figure 1.2: The distribution by age and sex of incidences of a) glioblastomas and b) anaplastic astrocytomas (taken from reference 11)

malignant glioma than the glioblastoma, (see section 1.2. below) has a peak incidence at 40 years of age as opposed to the glioblastoma at 50 years of age. Generally the less malignant tumours have a peak incidence at a lower age. The figure also reflects the higher incidence of these tumours in males. Possibly the most alarming statistic is the evidence that mortality and incidence are increasing. A British study indicates that male mortality rates from malignant brain neoplasms have risen from 4.55 per 100,000 in 1971-75 to 5.46 in 1981-87. The respective rates for females are 3.19 per 100,000 to 4.04 per 100,000 (12).

Cancer can be characterized by uncontrolled growth, invasiveness and metastasis. Metastasis is the transfer of disease from one organ or part to another not directly connected to it. Primary brain tumours are unique in that they rarely metastasize. Cancer, neoplasia, and malignancy can be used interchangeably. Other terms, often used in the description of cancer, are differentiation and anaplasia. Differentiation is defined as the acquiring or the possession of character or function different from that of the original type (13). Anaplasia is the lack of normal differentiation. Under the light microscope, cancer cells have large nuclei and more mitoses (dividing cells) are evident. Histologically, malignancy is generally characterized by disarray, with some degree of loss of normal tissue architecture.

In the brain tumours in adults predominantly arise from glial cells, ependymal cells and the supporting tissue of the brain. The glial cells form the glia (also called the neuroglia) and are the non-nervous cellular elements of the nervous tissue. Glial cells include the astrocytes, oligodendroglia and the microglia. The ependymal cells form a membrane in the brain. The supporting tissue of the brain includes the meninges or lining of the brain. The comprehensive list of primary brain tumours is shown in Table 1.1 and 1.2, classified according to the World Health Organization (WHO) scheme (14).

Classifications are necessary to allow communication to take place. Tumours of the brain are classified according to their appearance under the light-microscope. These classifications allow knowledge regarding the management of tumours to be communicated. In 1926 the first classification scheme for primary brain tumours was attempted (15). The basis for this classification was a comparison of the cells of the tumours with those of developing cells with respect to their degrees of differentiation. The scheme included categories such as pineoblastoma for malignant, poorly differentiated neoplasms of pineal cells and astrocytoma for neoplasms of astrocytes. This scheme was

- I. TUMOURS OF NEUROEPITHELIAL TISSUE
  - A. Astrocytic tumours
    - 1. Astrocytoma
      - (a) Fibrillary
      - (b) Protoplasmic
      - (c) Gemistocytic
    - 2. Pilocytic astrocytoma
    - 3. Subependymal giant-cell astrocytoma (ventricular tumour of tuberous sclerosis)
    - 4. Astroblastoma
    - 5. Anaplastic (malignant) astrocytoma
  - B. Oligodendroglial tumours
    - 1. Oligodendroglioma
    - 2. Mixed oligo-astrocytoma
    - 3. Anaplastic (malignant) oligodendroglioma
  - C. Ependymal and choroid plexus tumours
    - 1. Ependymoma
      Variants:
      - (a) Myxopapillary ependymoma
      - (b) Papillary ependymoma
      - (c) Subependymoma
    - 2. Anaplastic (malignant) ependymoma
    - 3. Choroid plexus papilloma
    - 4. Anaplastic (malignant) choroid plexus papilloma
  - D. Pineal cell tumours
    - 1. Pineocytoma (pinealocytoma)
    - 2. Pineoblastoma (pinealoblastoma)
  - E. Neuronal tumours
    - 1. Gangliocytoma
    - 2. Ganglioglioma
    - 3. Ganglioneuroblastoma
    - 4. Anaplastic (malignant) gangliocytoma and ganglioglioma
    - 5. Neuroblastoma
  - F. Poorly differentiated and embryonal tumours
    - 1. Glioblastoma
      Variants:
      - (a) Glioblastoma with sarcomatous component (mixed glioblastoma and sarcoma)
      - (b) Giant-cell glioblastoma
    - 2. Medulloblastoma
      Variants:
      - (a) Desmoplastic medulloblastoma
      - (b) Medullomyoblastoma
    - 3. Medulloepithelioma
    - 4. Primitive polar spongioblastoma
    - 5. Gliomatosis cerebri

Table 1.1: An outline of the World Health Organization scheme for classification of tumours of neuroepithelial tissue.

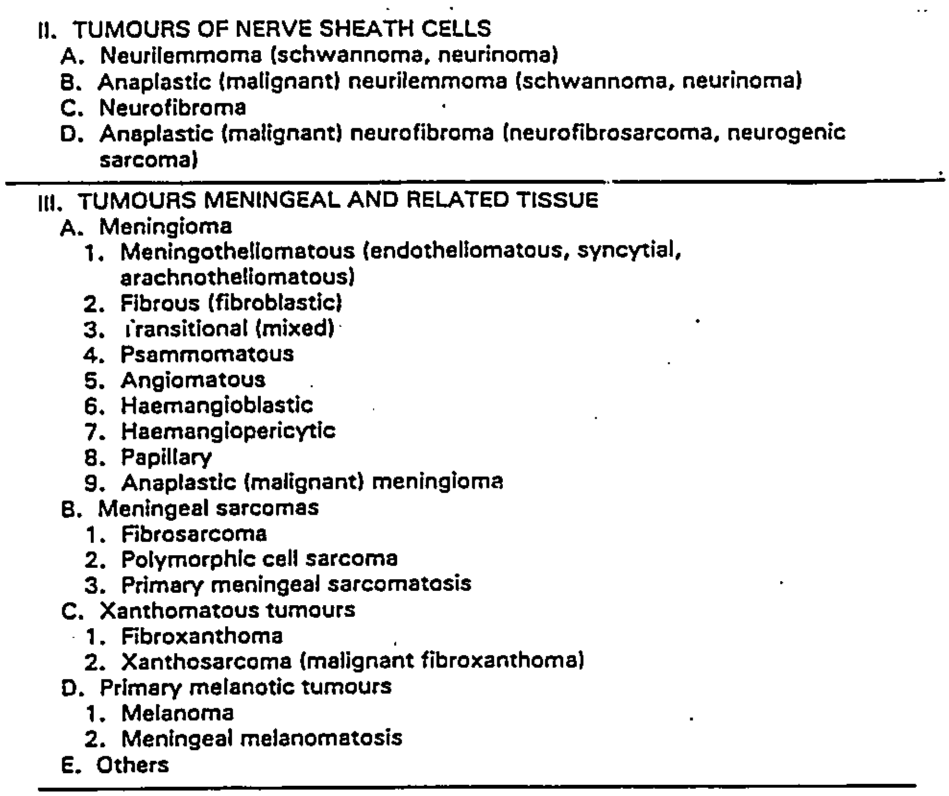

- II. TUMOURS OF NERVE SHEATH CELLS
  - A. Neurilemmoma (schwannoma, neurinoma)
  - B. Anaplastic (malignant) neurilemmoma (schwannoma, neurinoma)
  - C. Neurofibroma
  - D. Anaplastic (malignant) neurofibroma (neurofibrosarcoma, neurogenic sarcoma)

- III. TUMOURS MENINGEAL AND RELATED TISSUE
  - A. Meningioma
    1. Meningotheliomatous (endotheliomatous, syncytial, arachnotheliomatous)
    2. Fibrous (fibroblastic)
    3. Transitional (mixed)
    4. Psammomatous
    5. Angiomatous
    6. Haemangioblastic
    7. Haemangiopericytic
    8. Papillary
    9. Anaplastic (malignant) meningioma
  - B. Meningeal sarcomas
    1. Fibrosarcoma
    2. Polymorphic cell sarcoma
    3. Primary meningeal sarcomatosis
  - C. Xanthomatous tumours
    1. Fibroxanthoma
    2. Xanthosarcoma (malignant fibroxanthoma)
  - D. Primary melanotic tumours
    1. Melanoma
    2. Meningeal melanomatosis
  - E. Others

Table 1.2: An outline of the World Health Organization scheme for classification of tumours of nerve sheath cells and meningeal and related tissue.

based solely on cell morphology and additions were later made to emphasize anaplasia. As understanding increases regarding tumour cells, classification schemes must be updated. Classification of tumours is a slowly evolving system, and presently the most widely used scheme for primary brain tumours is shown in Table 1.1 and 1.2.

In this thesis the most common tumours of the brain are represented: gliomas, meningiomas and metastases. Gliomas comprise 40% of all brain tumours, meningiomas, 17% and metastases, 23%. The most common metastases to the brain are from lung in men and breast in women (16).

1.2. Gliomas

Gliomas are the neoplastic form of glial cells. Of the tumours arising from the glial cells, astrocytomas and glioblastomas are the most prevalent. Astrocytes give rise to 40% to 60% glial tumours. In this thesis three types of gliomas are included, astrocytomas, glioblastomas and mixed oligodendrogliomas/astrocytomas.

Kernohan was the first to employ a grading system for gliomas which gave a numerical grading from I to IV (15). These grades can be thought of as finer divisions which apply to each type of glioma in Table 1.1. In the Kernohan system, grade I is the best differentiated and the most malignant grade is IV. As well as cellular differentiation and anaplasia, the presence of necrosis, mitotic figures and vascular proliferation are important variables and influence the grading of the tumour. This grading system quickly became popular with neurosurgeons because it was related to prognosis and was simple to use. The system works best for astrocytomas which show the best correlation between microscopic appearance and clinical behaviour. However, prognosis will also depend on age, location of the tumour and length of symptoms. There is much controversy over the Kernohan classification. Some groups define the glioblastoma multiforme as synonymous with a grade IV astrocytoma, but others classify grades III and IV astrocytomas as glioblastomas (17, 18). Mixed grades such as II-III are often reported.

To solve this problem the World Health Organization (WHO) published a new comprehensive scheme for classification. Note that only the broad outlines of the WHO classification scheme are shown in Tables 1.1 and 1.2. Grades I to IV are still used and are denoted benign, semi-benign, anaplastic and malignant with patient survival times of greater than 5 years, 3 to 5 years, 1 to 3 years, and less than 1 year, respectively. Grade IV is synonymous with the glioblastoma. Brucher (19) states that the anaplastic astrocytoma (grade III) and the glioblastoma (grade IV) can be distinguished using the WHO system and gives survival rates of 416 days versus 305 days, respectively. Death resulting from recurrence of glioblastoma is 80% within one year (16). It is important to add that while prognosis for grade I and II, "benign", astrocytomas is significantly improved, these tumours are also highly lethal and the 5 year survival rate is approximately 30% with excision and radiotherapy. In this thesis astrocytomas of grades I to III and mixed oligoastrocytomas are classified as astrocytomas, while glioblastomas are left in a separate category.

1.3. Meningiomas

Meningiomas are tumours derived from the lining of the brain or meninges. They are named according to anatomical structure not by tissue or cell group. Meningiomas are generally a very diverse group and this is probably due to the nature of their classification which is by structure and not cell type. Meningiomas are slow growing, well encapsulated and generally more benign than the glial tumours. The WHO classification, Table 1.2, divides the meningiomas into nine groups with the first six generally considered benign tumours. Group seven, haemangiopericytic, and group eight, papillary, tend to be more malignant, and group nine, anaplastic, is clearly a malignant tumour.

Recurrence rates for meningiomas in general are 7% at 5 years, 20% at 10 years and 32% at 15 years (15). One difficulty with these tumours is that often biological behaviour is not predictable from histological appearance. Hypercellularity, cellular pleomorphism, diffuse growth, high mitotic rate, tumour necrosis, and bone invasion (20) are all histological parameters which have been correlated with biological parameters such as aggressive behaviour, faster growth rate and more frequent recurrence.

1.4. Metastases from the Lung

Metastasis from the lung to the brain is very common. The cumulative probability of metastasis to brain from the lung for patients with adenocarcinoma of the lung is 50%, with metastases occuring as late as in the fifth year after diagnosis (21). There are six main types of malignant lung tumours: squamous cell carcinoma, small cell carcinoma, adenocarcinoma, large cell carcinoma, carcinoids and mesothelioma. They are classified by standard light microscope techniques. The grade of differentiation of the tumour (well, moderately or poorly differentiated) is also determined, based on the most highly differentiated tissues. Adenocarcinoma and large cell carcinoma have the highest rates of metastasis to brain. Most lung metastases presented in this thesis are adenocarcinoma. Adenocarcinoma is identified as a primary malignant tumour with tubular acinar or papillary growth pattern and/or mucous production. They arise from the epithilium of the bronchi and are peripherally located.

The median survival for a patient with brain metastases from the lung is three to four months. In an attempt to control this metastasis, cranial radiation has been proposed (21).

1.5. NMR Theory

The tumours described above are frighteningly lethal, despite the many therapies a clinician can now employ. More research is required to aid in early diagnosis, to improve and to discover new, more effective treatments, to monitor treatments and to understand tumour progression. The research described in this thesis uses nuclear magnetic resonance (NMR) techniques. In order to describe what NMR can potentially contribute to brain tumour diagnosis and therapy, the basics of how and what NMR detects are described in this chapter.

Nuclei have spin and an associated magnetic moment (22, 23). In a magnetic field the spins are limited by quantum mechanics to (2I + 1) orientations, where I is the spin quantum number. The energy level diagram for a spin 1/2 system is shown in Figure 1.3. There are two allowed states; parallel (↑) and anti-parallel (↓) to the magnetic field, and the separation between these states is dependent on the strength of the magnetic field. To excite a transition from one energy level to the other it is necessary to supply the energy

$$\Delta E = \hbar\omega = \gamma\hbar B_o.$$

B_o is the applied magnetic field, ω is the frequency of the irradiation and γ is the magnetogyric ratio. The magnetogyric ratio is characteristic of the nucleus and thus the frequency, ω, will depend on which nucleus is being observed. If the spin system is in thermal equilibrium the distribution of the spins between the two levels will be determined by the Boltzmann distribution:

$$n(\uparrow)/n(\downarrow) = \exp\ (-\Delta E/kT).$$

At body temperature (310°K), the excess of protons as a fraction of the total spins in the low energy or parallel state is only 3.3×10^{-6}. This results in NMR being an insensitive technique relative to techniques such as ultraviolet and infrared spectroscopy. While many aspects of

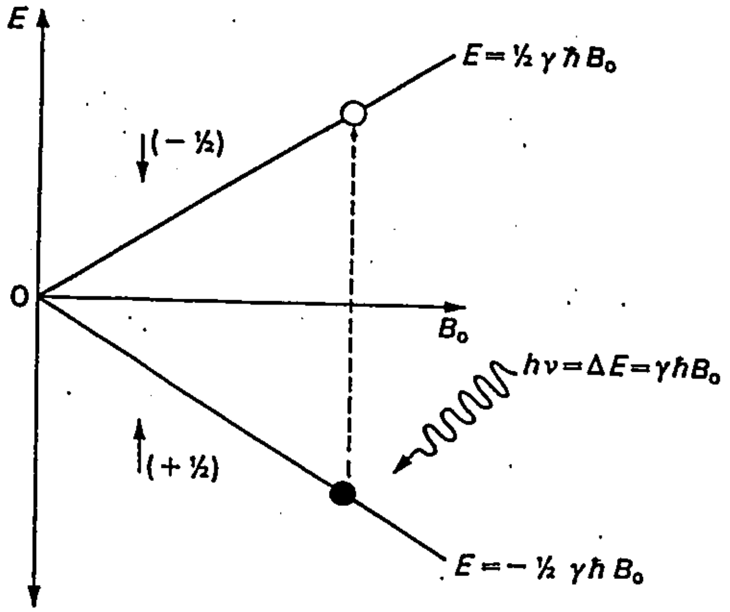

Figure 1.3: The energy levels of a one spin system (taken from reference 23)

NMR can only be explained using a quantum mechanical description, what happens as the spins interact with the magnetic field can be visualized in classical terms.

In physical terms the interaction is explained by precession of the magnetic moments of the nuclei about the magnetic field. The phenomena of precession is best explained by referring to the more familiar case of a child's top or a gyroscope (24). Why does a rotating gyroscope or top not fall over, but instead begins a different motion called precession. Figure 1.4 schematically shows a gyroscope and the forces which are present. If the string is pulled and the flywheel is set in motion the gyroscope will begin to circle about the axis, P, in a horizontal plane as shown. This motion, while not intuitively obvious, can be explained by the addition of angular momentum vectors. The forces acting on the gyroscope are gravity due to its weight, w, and the force P at the pivot point. If the gyroscope were at rest the torque of these two forces would cause a rotation and, as is intuitively obvious, the gyroscope would fall. Because the flywheel is spinning, the gyroscope is not at rest, and thus the torque from w and P changes the rotational motion already in progress. The vector L shows angular momentum due to the spinning and ΔL is the angular momentum caused by the force w in a short time interval Δt. Vector addition of these angular momenta, as shown in Figure 1.4,

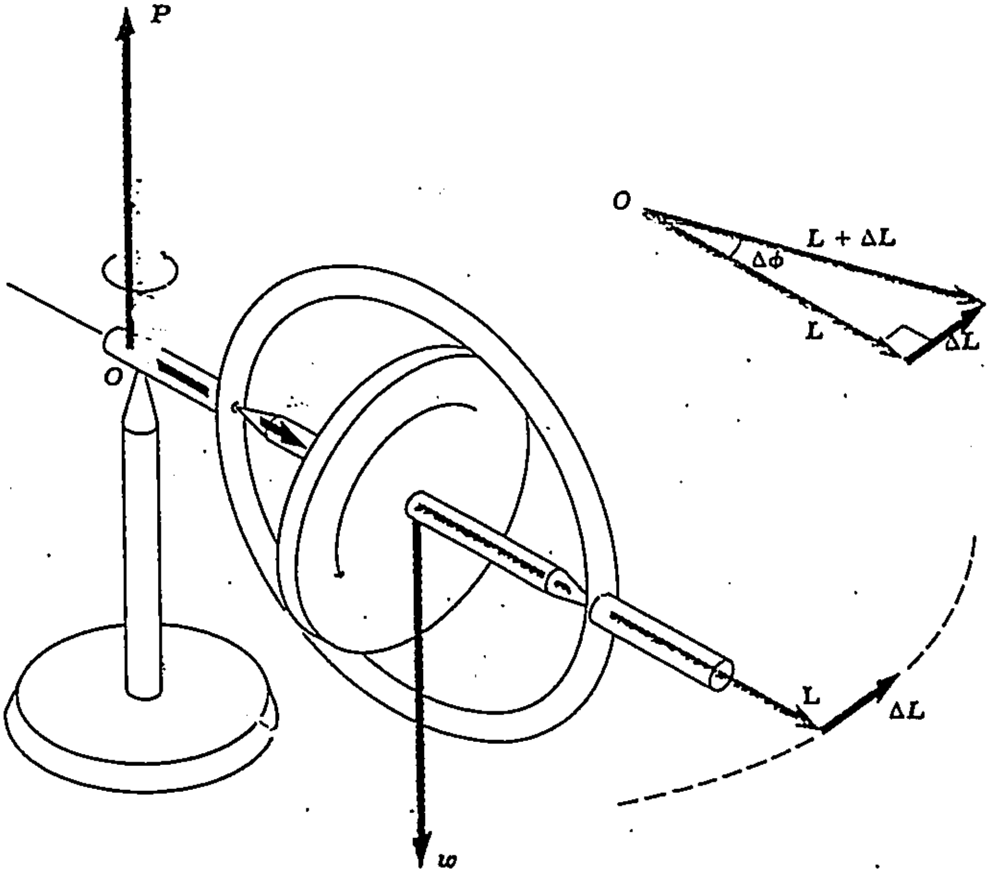

Figure 1.4: Diagram of a gyroscope and the forces involved (adapted from reference 24).

explains the motion in the horizontal plane. The motion is called precession.

The interaction between the magnetic moments of the nuclei and the magnetic field, B_o, generates a torque similar to that in the gyroscope. The nuclear magnetic moment in the magnetic field experiences a coupling tending to align it with the field. Because the nuclei possess spin angular momentum, precession results. The sum of the magnetizations of all the spins can be represented by a vector, and the precession of this vector, shown in Figure 1.5, has a frequency of

$$\omega_o = \gamma B_o$$

called the Larmor frequency. The field each nucleus actually experiences is B and σ is the shielding parameter

$$B = (1-\sigma)B_o$$

which depends on the chemical environment. Nuclei in different chemical environments will therefore have different Larmor frequencies. The difference in frequencies with respect to a reference is called chemical shift and is usually converted to ppm units by dividing by the spectrometer frequency.

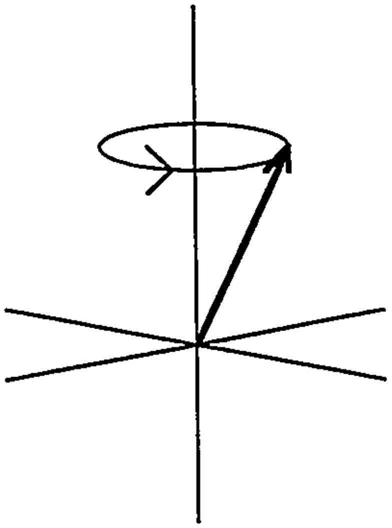

Figure 1.5: Precession of the bulk magnetization about the magnetic field.

To detect this information a magnetic field perpendicular to B_0, B_1, is applied at the Larmor frequency for a brief duration of time. This field results in precession of the magnetization around B_1. A so-called 90° pulse rotates the magnetization from the z axis (B_0 axis) to the y axis. Figure 1.6 shows the effect of a pulse which rotates the magnetization β degrees. Once in the x-y plane, the magnetization continues to precess at the Larmor frequency.

To make manipulations of the magnetization easier to visualize, a rotating reference frame may be used. In the rotating reference frame, the z axis remains the field direction, but the x and y axes rotate about the z axis at a frequency of ω_0. After a 90° pulse, although the magnetization is precessing about B_0 at the Larmor frequency in the x-y plane, this will be represented by a vector stationary on the y axis in the rotating frame. If a receiver coil is placed on the x axis in the laboratory frame, the precession will induce current in the coil and a nuclear magnetic resonance signal can be detected. If nuclei with differing chemical environments are present, more than one frequency will be received. The signal received is called the free induction decay, or FID.

Once B_1 is shut off the decay of the signal is a result

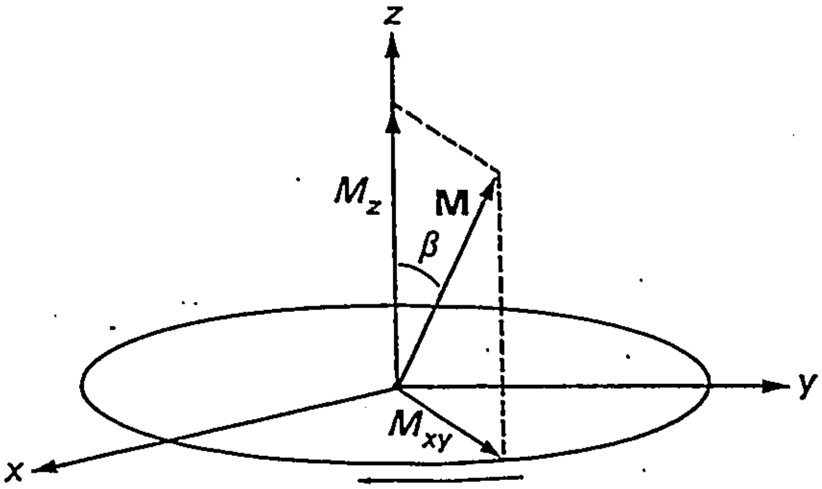

Figure 1.6: The precession of the bulk magnetization in the laboratory frame following the application of a radiofrequency pulse (taken from reference 23).

of transverse relaxation. The return to equilibrium is the result of a second type of relaxation, longitudinal relaxation. Longitudinal relaxation describes the transfer of energy from the spins to the lattice and results in the spins realigning themselves with B_0. The transverse relaxation determines the decay of the x-y components of the magnetization, and involves the gradual dephasing of the spins in the x-y plane. Transverse relaxation can occur at a rate faster than, but not slower than the rate of longitudinal relaxation. Both types of relaxation depend on magnetic interactions and their rate of modulation. The signal decay will also depend on experimental factors such as poor homogeneity of the magnetic field. The actual transverse time constant seen in the FID is called T_2^*. A short T_2^* will result in a spectrum with broad lines. If the longitudinal time constant, T_1, is long, time constraints may make it impossible to delay the next acquisition until the magnetization is fully restored to the z axis. If this is the case, a species with long T_1 will have a lower intensity in the final spectrum, due to implete relaxation between pulses.

The final step, before interpretation of the NMR signal, is a Fourier transform of the FID to convert the frequencies received from the time domain to the frequency domain where they can be analyzed.

1.6. NMR and Brain Cancer

The following nuclei are most commonly used in NMR studies of humans; ^{19}F, ^{31}P, ^{1}H and ^{13}C. While there are many other NMR visible nuclei, i.e. with non-zero nuclear spin, there can be complicating factors when dealing with biological systems. Sensitivity is adversely affected by a low magnetogyric ratio or by low natural abundance. Some nuclei must be eliminated because of low physiological concentrations.

To date, the most common use of NMR in human studies is magnetic resonance imaging. This technique is now a common clinical tool used for diagnosis and treatment planning. Spectroscopy is not nearly so widespread as a medical tool. However, many research hospitals are now equipped with magnetic resonance imagers, which can perform in vivo spectroscopy. Fluorine spectroscopy is used to study the distribution and metabolism of chemotherapeutics in the brain. It is an isotope which has enhanced utility because it has a low physiological concentration. Carbon-13 studies generally involve the ingestion of labelled compounds.

^{31}P and ^{1}H NMR studies of human brain tumours predominate. The research outlined in this thesis is in two parts: *in vivo* phosphorus studies, and *ex vivo* proton studies. The next two chapters will describe the information available from these two nuclei and any special techniques required to obtain the NMR spectra.

CHAPTER 2

Phosphorus NMR of Human Brain Tumours

Background and Localization Theory

Phosphorus NMR spectroscopy of human brain tumours, *in vivo*, has been possible technically for approximately five years. Much more research has been done, for obvious reasons, on animal models. The amount of information available from a phosphorus spectra *in vivo* is surprising, given that a typical spectrum has only seven peaks, with three of those peaks largely representing the same compound. Much can be determined from the phosphorus spectra including, possibly, diagnosis and the biochemical status of the tumour.

It is important, when possible, to obtain spectra of tumour uncontaminated with normal tissue. This has led to the development of spectroscopic localization techniques which allow acquisition from only certain volumes within a sample. There have been two approaches towards this goal; the first is to eliminate signal from all areas except the volume of interest. The second approach is to divide the entire sample into sections, or voxels, and to obtain a spectrum for each voxel. In the second approach, the spectra can be assembled to create a spectral map of the sample. To obtain spectra from a tumour in the human brain, one of these approaches must be used. In this thesis, the localization technique used was chemical shift imaging (CSI), or spectroscopic imaging (SI). This technique obtains spectra from a number of voxels simultaneously.

2.1. Phosphorus 31 Spectra of the Human Brain

A typical phosphorus spectrum of a human brain, obtained using a surface coil and no other localization technique, is shown in Figure 2.1. A spectrum which was acquired using the chemical shift imaging technique is shown in Figure 2.2. The spectrum in Figure 2.2 has been baseline-corrected and the underlying large hump characteristic of brain spectra, as seen in Figure 2.1, has been eliminated. The peaks in the spectrum have been assigned to the following compounds: phosphomonoesters (PME), inorganic phosphate (Pi), phosphodiesters (PDE), phosphocreatine (PCr), and nucleotide triphosphates and diphosphates, labelled for convenience as the most abundunt species, adenosine triphosphate (ATP).

Relative intensities of three of these compounds, ATP, Pi and PCr, reflect the cellular energy state. ATP and PCr

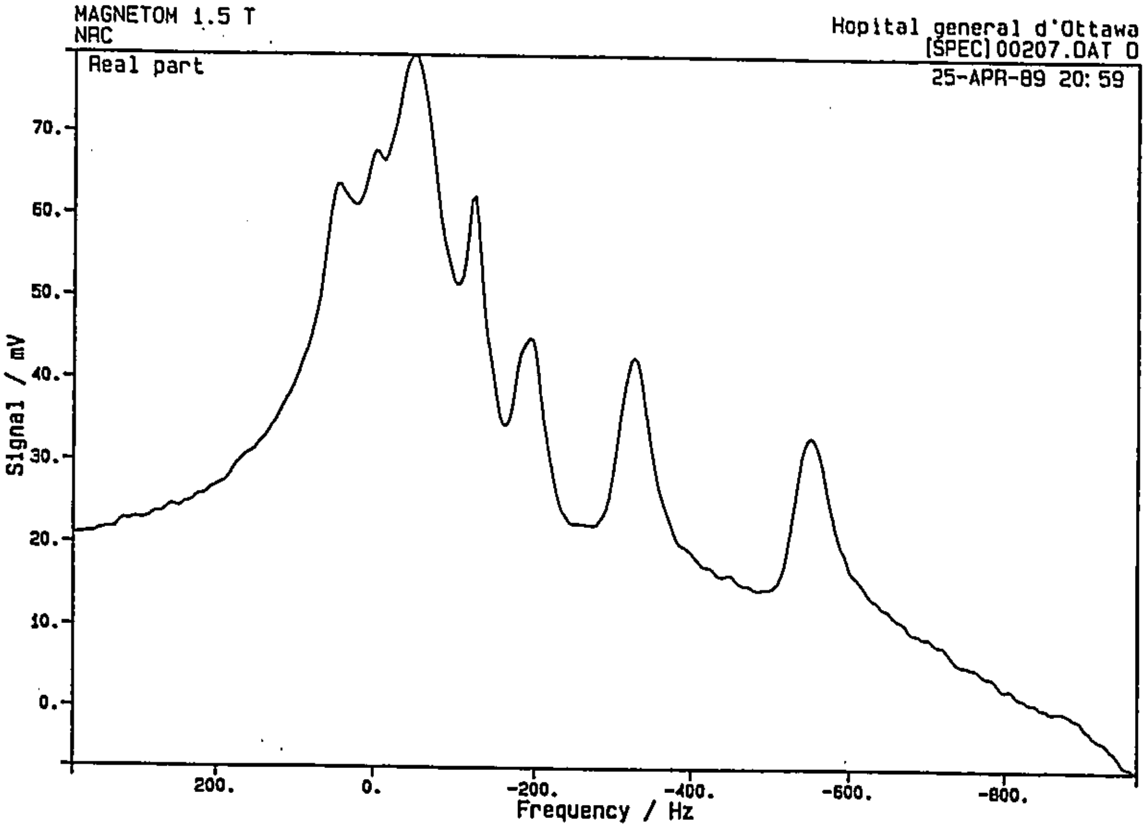

Figure 2.1: Typical phosphorus spectrum of a human brain localized only by a surface coil.

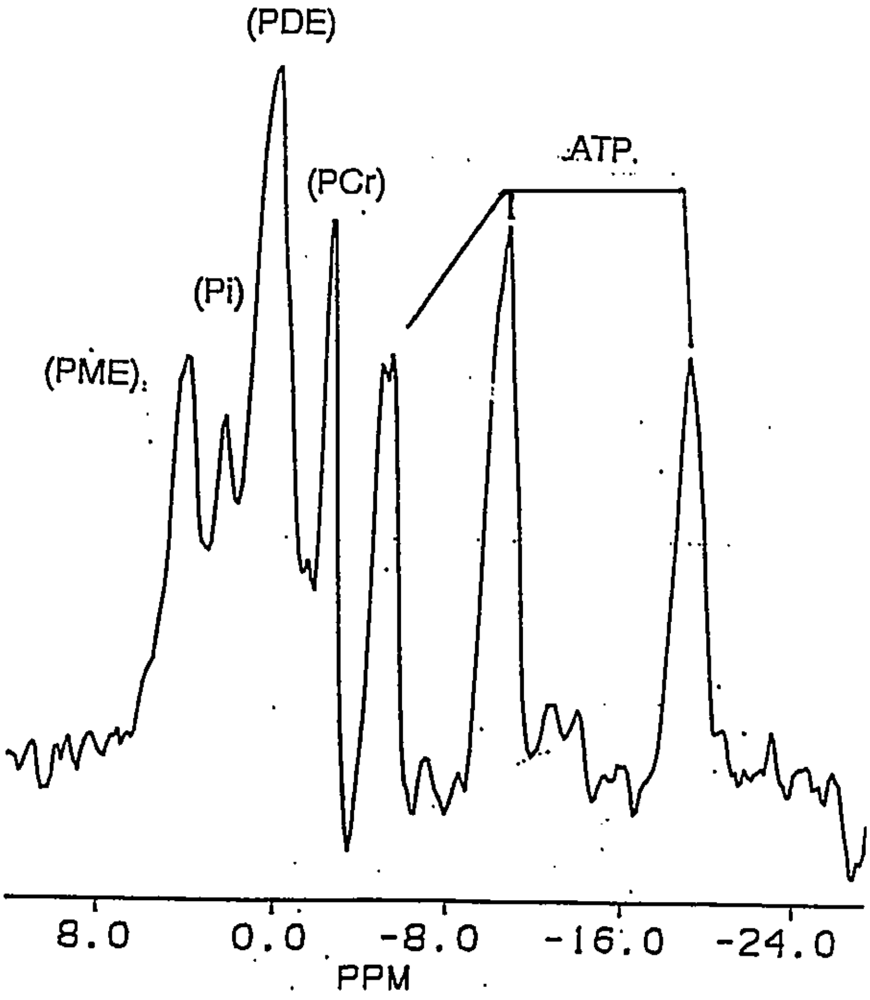

Figure 2.2: CSI1D phosphorus spectrum of human brain processed with convolution difference, line broadening and baseline fitting.

are high energy phosphate compounds, whereas Pi is released when the energy stores are used, Figure 2.3. The ratio of PCr to ATP varies markedly from tissue to tissue; in brain it is approximately 2:1, but in muscle tissue it is much higher. Relative to healthy tissue, bioenergetically unhealthy brain tissue will have low PCr and ATP levels and high Pi levels. Pi in healthy tissue will be reused for the synthesis of ATP in glycolysis and respiration. Unhealthy or dead tissue should have low PCr and ATP levels, with high Pi levels, because catabolic but not anabolic processes can continue in dead tissue. PCr acts as an energy store, and will decrease first if a tissue is under stress, thus maintaining the cell's primary energy source, ATP. Animal models (2) have shown that as a tumour grows larger and progresses towards a dead or necrotic tissue with few blood vessels, PCr levels decrease and Pi levels increase. Ultimately the ATP concentration also declines, and the Pi resonance dominates the spectrum of the tumour.

The inorganic phosphate peak is an exceedingly useful peak in the ^{31}P spectra; not only does it yield information regarding the energy status of the tissue, it also can be used to determine pH (25). The inorganic phosphate peak is an average of two resonances, $H_2PO_4^-$ and HPO_4^{-2}, at physiological pH's. These compounds are in equilibrium,

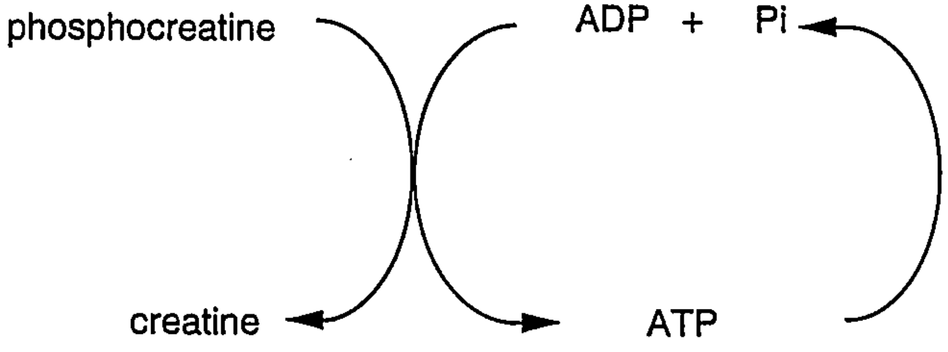

Figure 2.3: Pathways showing the link between ATP, Pi and PCr.

$$H_2PO_4^- \rightleftharpoons HPO_4^{2-} + H^+.$$

The exchange is rapid and therefore the Pi NMR peak represents the average chemical shift of the two compounds, with the measured value being a concentration weighted average of the shifts of the two species. The chemical shift therefore is a measure of pH, and, as can be seen in Figure 2.4, it conveniently changes most rapidly with pH in the range of physiological pH.

The pH of tumours has long been assumed to be in the acidic range because tumours cells are generally believed to derive a higher percentage of their ATP from glycolysis and thus produce larger amounts of lactic acid (26). Compared to normal cells, the tumour cells therefore derive a lower percentage of their energy from full oxidation (i.e. using the tricarboxylic acid cycle). When animal tumours become necrotic, the pH measured by the chemical shift of the Pi peak, does show an acidic pH (26). Some animal tumours, however, have a neutral or alkaline pH (27). Ng et al (28) demonstrated by NMR that most human tumours have a pH ranging from neutral to alkaline. In light of microelectrode measurements of pH indicating interstitial acidosis in tumours, it has been hypothesized (26) that cancer cells are chronically adapted to the increased acid production and are capable of pumping the H^+ ions into the

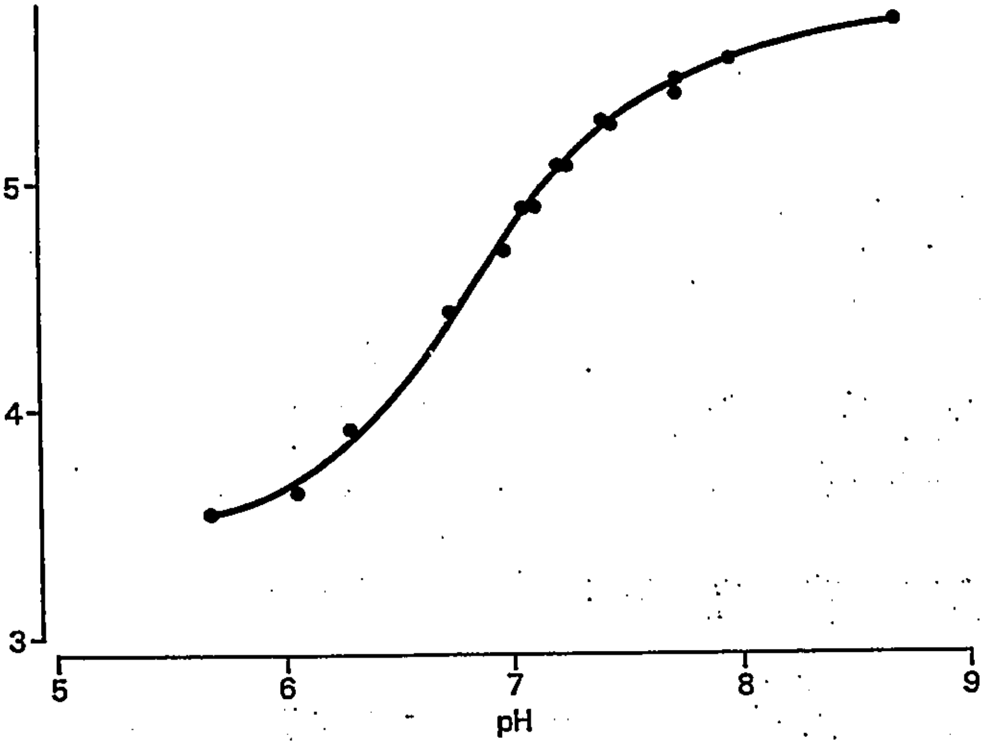

Figure 2.4: Titration curve for inorganic phosphate at physiological pH (taken from reference 23).

interstitial space at the same rate as they are formed. Another hypothesis (28) is that the hypoxic cell fraction (hypoxia may be the cause of the glycolytic metabolism in tumours) has been over-estimated. It is generally agreed, however, that the concept of neutral to alkaline pH of tumours has important implications in the design of radio sensitizers and certain chemotherapeutic drugs.

The two peaks in the ^{31}P spectrum not yet discussed are those due to PME and PDE. The phosphomonoester peak is predominantly comprised of phosphoethanolamine and phosphocholine (29). The phosphodiester peak is mainly composed of glycero-phosphoethanolamine and glycerophosphocholine (30). There is a broad component to the PDE peak which has been eliminated by to baseline correction in Figure 2.2. The broad component of PDE has been shown to be due to bilayer phospholipids and mobile phospholipids (31, 32). The PME peak and the PDE peak predominantly represent intermediates in phospholipid metabolism. Since a rapidly growing tumour must have increased membrane production, it has been suggested that this would be reflected in alterations in the PME and PDE contributions to the phosphorus spectra (33).

Studies of developing rat brain have shown that PME is high at birth, peaks around day 10 after birth and then declines (34). Studies of developing brain are important because they are a means to study not only the rapid growth which is present in tumours, but also differentiation. Tumours are dedifferentiated and neonatal tissue reflects the opposite trend, differentiating as they grow. Early neonatal tissue has rapid growth, is undifferentiated, and thus might serve as a model for tumour tissue. The NMR of the brain of aged rats showed increased levels of PDE relative to adult rats, but PME levels were consistent with adult rats (35).

Early NMR studies of human brain tumours indicate that PME levels are higher in tumours when compared to normal brain tissue (36, 37). The alterations in PME and PDE levels can be interpreted as an alteration in membrane metabolism (29). It has been more specifically hypothesized that increased PME concentration with decreased PDE levels could indicate membrane synthesis and thus tumour growth (6). The biochemistry of these compounds in tumour and normal tissue is not fully understood. Treatment response studies have shown that the monitoring of PDE and PME levels may ultimately be useful in treatment management. PME and PDE signal intensities in the spectrum of a tumour are often dramatically affected by radiotherapy or chemotherapy and the nature of the response in the phosphorus spectra may reflect the patient's overall response to the therapy (38, 39, 40).

2.2 ^{31}P Chemical Shift Imaging

Information regarding metabolic status of the tissue, membrane metabolism and possibly the response to treatment may be present in the phosphorus NMR spectra. Once large bore magnets were available and spectra could be obtained from larger animals and humans, the problem arose as to how to obtain spectra from particular areas or volumes of interest. The initial solution to the problem was the introduction of surface coils by Ackerman (41). Conventional solenoid and saddle-shaped radiofrequency coils used in narrow bore high resolution spectrometers are designed to produce a homogeneous field distribution (B_1) which will ensure uniform signal from all portions of the sample. The surface coil was designed to observe signal only from regions adjacent to the surface of the sample. The circular surface coil has been widely used. For this coil, the radiofrequency magnetic field, B_1, is localized in a volume defined approximately by the diameter of the coil and penetrates to a depth of the radius of the coil. A diagram of a surface coil and its B_1 field profile is shown in Figure 2.5. Note that the intensity of the B_1 field decreases as distance from the coil increases. A pulse length which is equivalent to a 90° pulse at depth of 2 cm from the coil will rotate the magnetization through a much smaller angle at 3 cm and a much larger angle

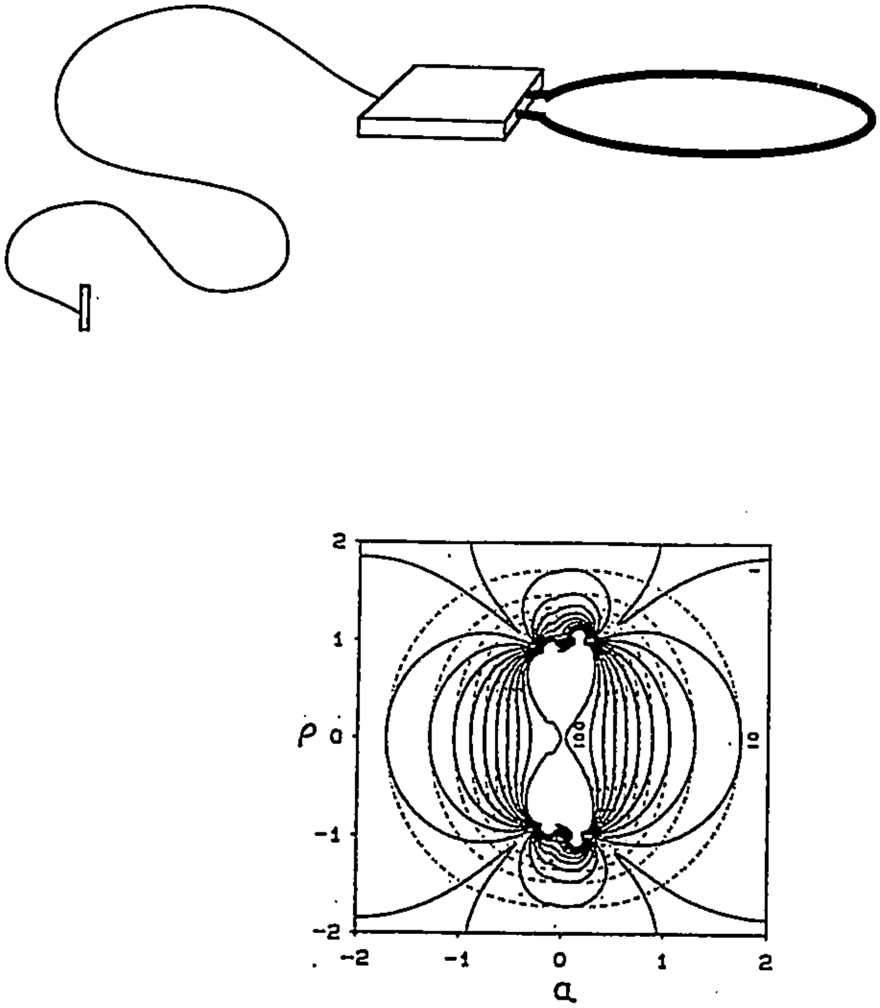

Figure 2.5: Diagram of a surface coil and its profile (α is the distance from the coil in units of coil radii and ρ is the diameter of the coil).

at 1 cm. Thus, signal intensity depends strongly on the location relative to the coil and most of the signal received will come from the surface of the sample.

The surface coil is still widely used to obtain *in vivo* NMR spectra. Experiments with surgically implanted coils have widened the range of applications, but this seriously compromises the noninvasive nature of NMR and is inapplicable to human subjects. The desire to define more clearly the area from which the NMR signal was coming and the desire to non-invasively take spectra from areas not adjacent to the surface of the subject caused the development of a number of multidimensional techniques for this purpose. Progress in coil design has yielded head coils which surround the human head and are capable of producing uniform B_1 field throughout the head. A surface coil will, however, have better signal to noise for its volume.

One of the simplest spatial localization techniques requires the use of a surface coil and an application of a pulsed magnetic field gradient. This technique, chemical shift imaging, uses a surface coil to select a volume and obtains a series of spectra as the amplitude of the gradient is increased. The technique has been called spectroscopic imaging and chemical shift imaging. These terms will be used interchangeably in this thesis.

A uniform field gradient, G, is the varying of the static magnetic field, B_0, linearly with space, d. If the field varies linearly in the z direction then the field in that direction can be defined as:

$$B_z = B_0 + Gd.$$

The precessional (Larmor) frequency of any spins in the gradient will have the same spatial dependence. Thus, by applying a gradient the precessional frequency will depend on location. If a free induction decay is acquired while the gradient is applied, the spatial information will have been encoded into frequency. Figure 2.6 demonstrates this effect. This type of gradient is called a read gradient and is commonly used in imaging sequences.

The type of gradients implemented in CSI sequences use phase to encode information. Phase can be characterized as position in the x-y plane of the rotating frame. After a 90° pulse all spins will be on the y-axis in the rotating frame. Any spins which are not at the reference frequency, will rotate in the x-y plane of the rotating frame. The amount a spin will rotate depends on the difference between its frequency and the reference frequency. The effect of this change in phase on the Fourier-transformed signal is shown in Figure 2.7. The further off-resonance a signal is,

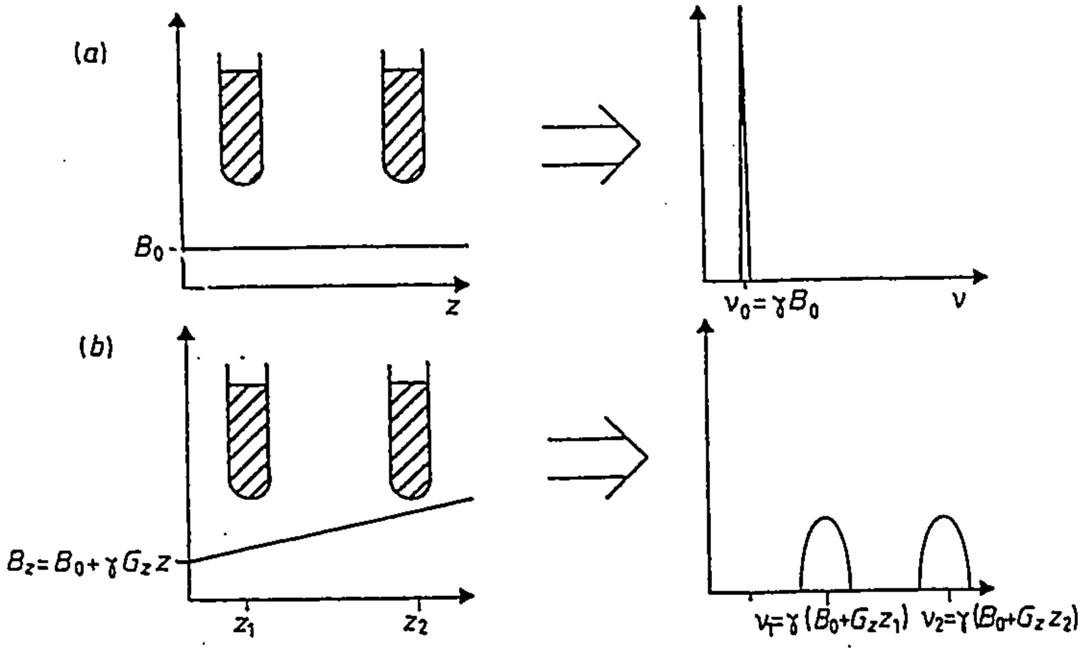

Figure 2.6: Demonstration of the effect of a linear gradient on spectra acquired on two tubes containing the same substance. (a) With a constant B_o only one frequency is seen in the resulting spectra. (b) If a linear gradient is applied the spectrum shows two frequencies, with a separation proportional to the spatial separation (taken from reference 34).

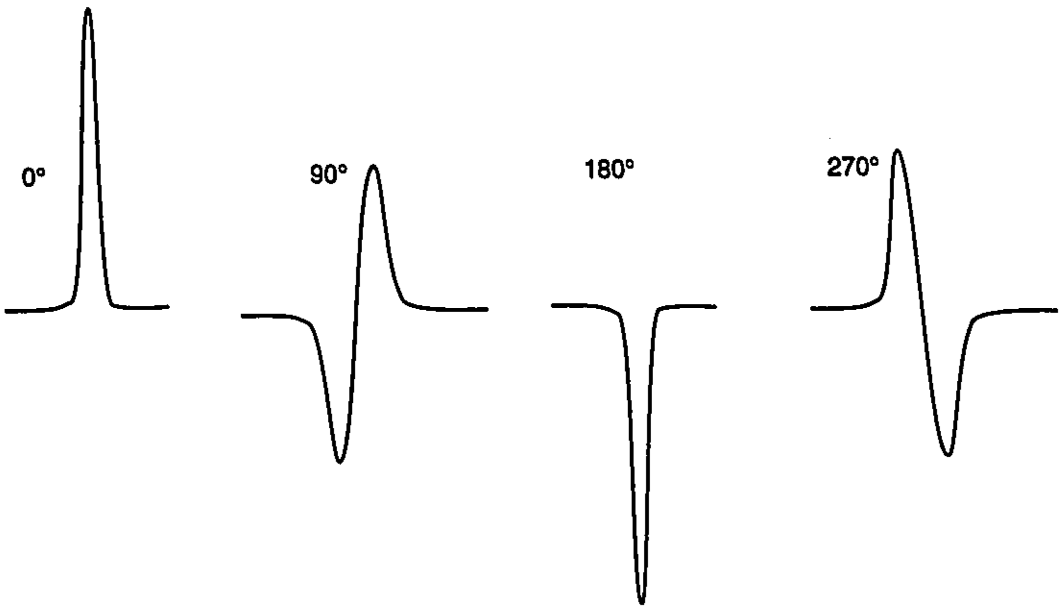

Figure 2.7: The effect of phase on a signal.

the larger the phase difference will be. These phase changes are called first order because they vary linearly with frequency. If acquisition is commenced quickly after the 90° pulse, the first order phase corrections needed are small.

The phase encoding gradient used in spectroscopic imaging works by inducing a phase shift. As already stated above, after a 90° pulse a spin that is on resonance will sit on the y axis of the rotating frame (see section 1.3 above), assuming no relaxation. If, however, a gradient is applied for a time, t, the precession frequency will change for the spin and the spin will begin to move in the rotating frame. Once the gradient is turned off, the frequency of the spin will return to its previous value, but its phase will have been altered. During t, the amount that the phase of the spin has changed, or stated differently, the amount that the spin has rotated with respect to the rotating frame, will depend on where the spin was located in the gradient. Figure 2.8 shows what happens to a spin if this experiment is repeated three times; with no gradient and with a gradient on for t and 2t. The phase changes at a frequency:

$$\omega = \gamma G_y y_o.$$

When the intensity of the Fourier-transformed spectrum is

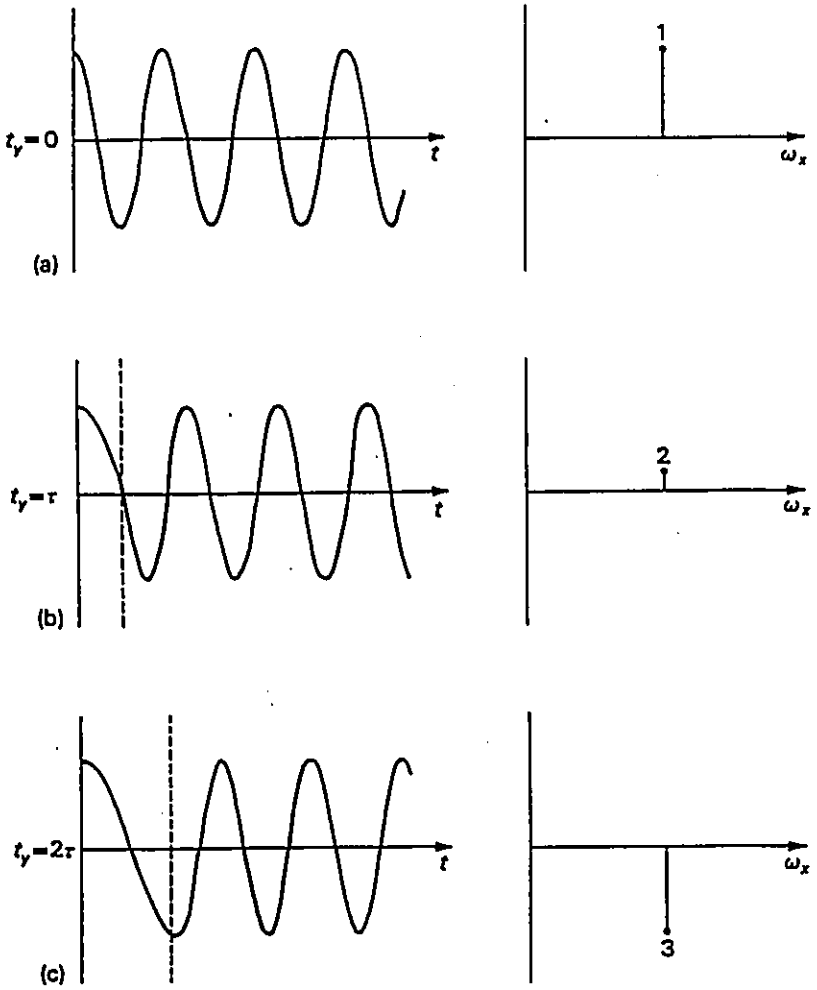

Figure 2.8: FID's and the Fourier transformed spectra for a single spin located at y_0 with the gradient G_y left on for three different intervals (taken from reference 23). The dashed line indicates the time at which the gradient is switched off and acquisition is started.

plotted, a cosine function of the above frequency is described. By performing a second Fourier transform the spatial information is retrieved. Figure 2.9 demonstrates the full spectroscopic imaging experiment for two spins in different positions in a gradient. The spectra for ten different values of t are shown along with the plotted intensity. The amplitude varies systematically with a frequency which is dependent on location. The phase of sample A changes more quickly than that of B because the gradient strength is higher at A's position. The intensities are shown plotted and the final result is shown as a two dimensional plot with chemical shift information in one dimension and spatial information in the second. These two spins, A and B, have different chemical shifts in the absence of a gradient and it is important to note that the chemical shift information is preserved in this experiment. If the amplitude of the gradient is increased in sucessive FID's, instead of the time that the gradient is applied, the same result is obtained. The pulse sequence is shown in Figure 2.10. After a 90° pulse a gradient is applied for a short time. A number of experiments, in which the amplitude of the gradient is systematically increased, are run. Because of the fast Fourier transform algorithm, the number of experiments, or phase encoding steps is usually chosen to be 8, 16, or 32. Larger numbers of steps are possible but are generally too time consuming.

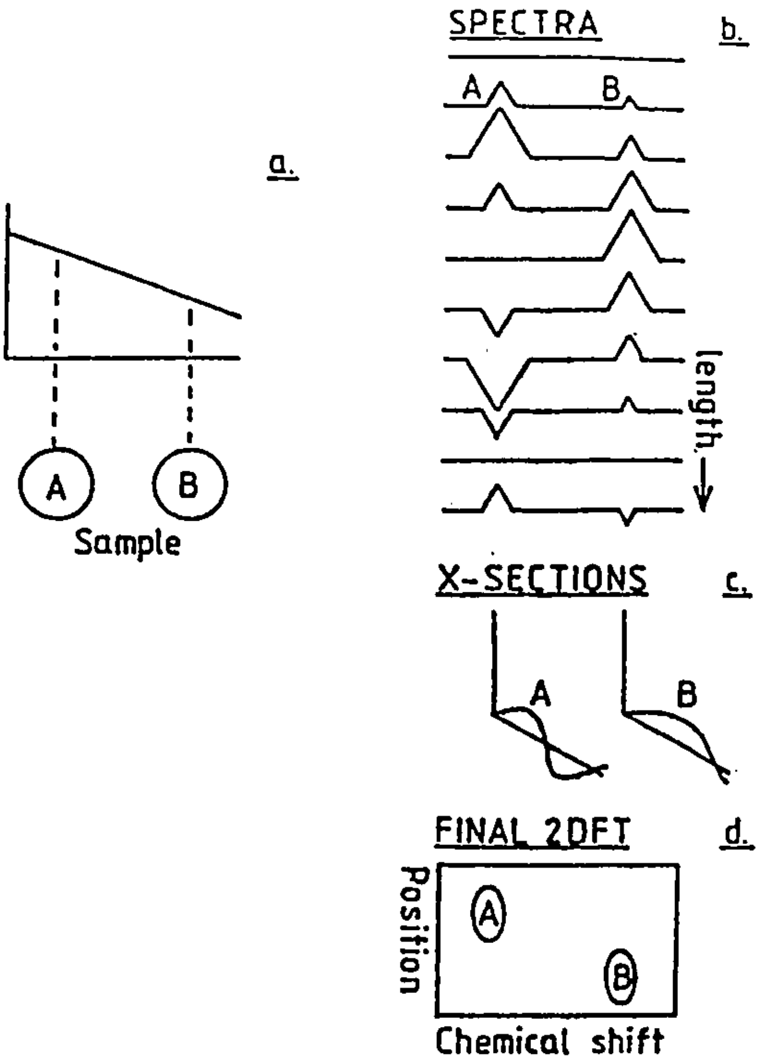

Figure 2.9: A spectoscopic imaging experiment for two spins in different positions in a gradient. See text for detailed explanation.

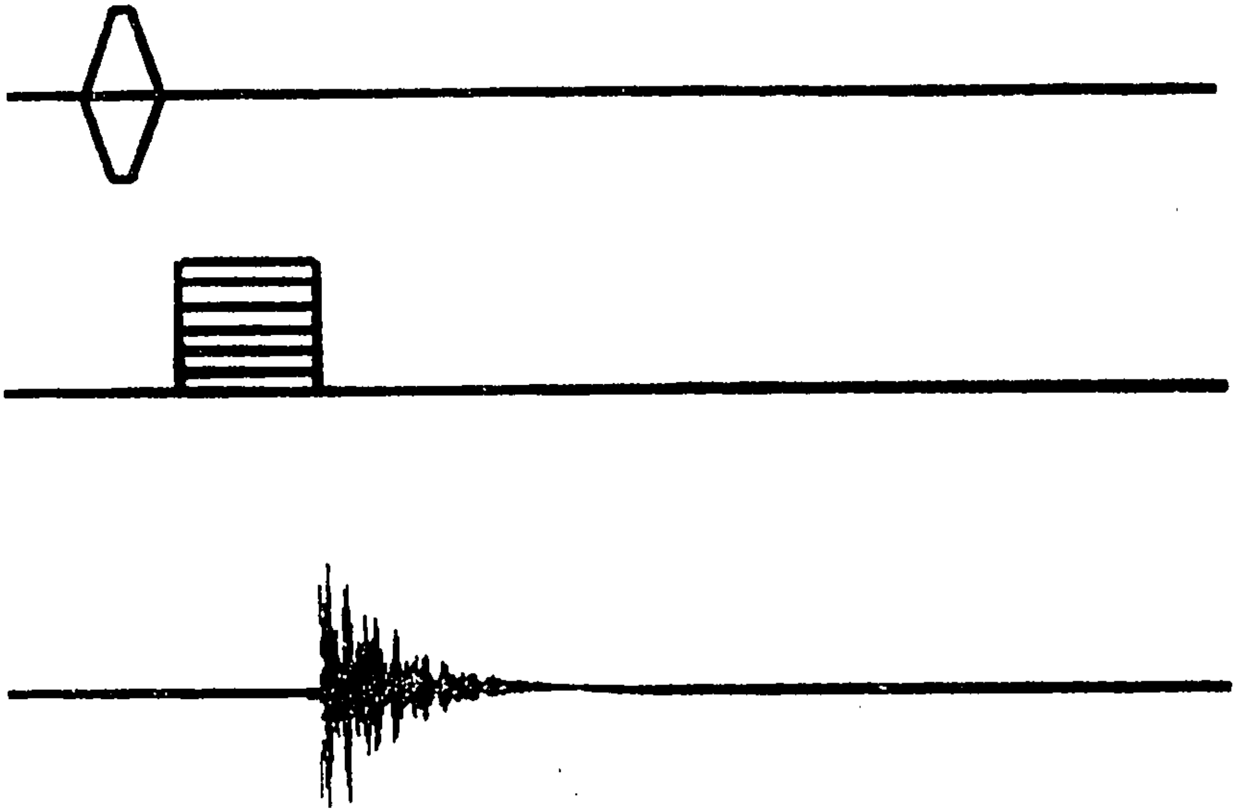

Figure 2.10: One dimensional chemical shift imaging sequence.

When the sequence in Figure 2.10 is used, large first order phasing errors occur. These are caused by the long delay between the 90° pulse and acquisition. The delay is caused not only by the duration of the phase encoding gradient, but also by the further delay which must follow the gradient. This delay is necessary because gradients cause eddy currents. Eddy currents are currents in any surrounding metal which are induced by currents in the gradient coils. These currents will cause inhomogeneities in the magnetic field B_0 and thus can cause distortions in the baseline and broadening of spectral lines. This problem can be reduced by using actively or passively shielded gradients. In simple terms, an active shield creates currents of opposite polarity which cancel the eddy currents. Passive shielding is performed by adding a shield of material around the gradients which absorbs the eddy currents.

Another important problem with all localization techniques is that the voxels can have some contamination of signal from adjacent voxels. If a signal is very large, the bleeding of this signal into neighbouring voxels can be a significant problem. For CSI, the problem is a consequence of using a Fourier transform algorithm with a small number of phase encoding steps. Weighting certain phase encoding steps according to a Hanning window function (43) or the use of a Gaussian function can reduce this bleeding.

An early application of this technique allowed simultaneous acquisition of control data. Haselgrove et al (44) applied one dimensional chemical shift imaging to attempt to identify ischemia in rat muscle. The technique was slightly different than that described above because a 180° pulse was used to eliminate first order phasing problems. This pulse eliminates the first order phasing problems which occur because of the delayed acquisition discussed above. The echo, however, can increase the time beween acquisition and excitation and therefore loss of intensity due to T_2 relaxation is increased. The rat's leg's were placed together in the probe, with a torniquet applied to one hind limb. Localization was used to obtain spectra from each leg. The control leg showed a strong phosphocreatine peak. The ischemic leg showed a broad inorganic phosphate peak. In the spectra of the rat limbs no ATP was observed due to the short T_2 value.

CSI can be expanded to require a four dimensional fourier transform (45, 46). Three gradients are used with each being incremented one after the other. The resulting data set, once Fourier transformed in four dimensions, will yield a spectrum from every cube within the sensitive area of a coil. Time constraints are an obvious limitation of this experiment. Each gradient must be incremented sequentially making the number of experiments very large. If limited spatial resolution is required, then the number of phase encoding steps and thus the time required can be reduced, making the experiment more practical.

A common solution to this problem is the use of frequency selective pulses in combination with a gradient to select a slice (47, 48). This experiment is a limited version of the full chemical shift imaging experiment. To accomodate time constraints, information is not obtained from all surrounding areas. The experiment in terms of chemical shift imaging is now two dimensional, with a Fourier transform yielding a spectrum from every square in the slice defined by the frequency selective pulse, as opposed to yielding information from every cube in the sensitive volume. The strength of the gradient can be varied to allow selection of varying thickness. This sequence is shown in Figure 2.11.

An error introduced by application of this method is a problem common to all methods using B_0 gradients to slice-select a volume. The selection of a volume in this manner is hampered by the frequency shift caused by chemical shift. If a frequency selective pulse of bandwidth 500 Hz is used, then signal from, for example, PME and ß-ATP signals which are approximately 600 Hz apart at 26 MHz, will be selected from

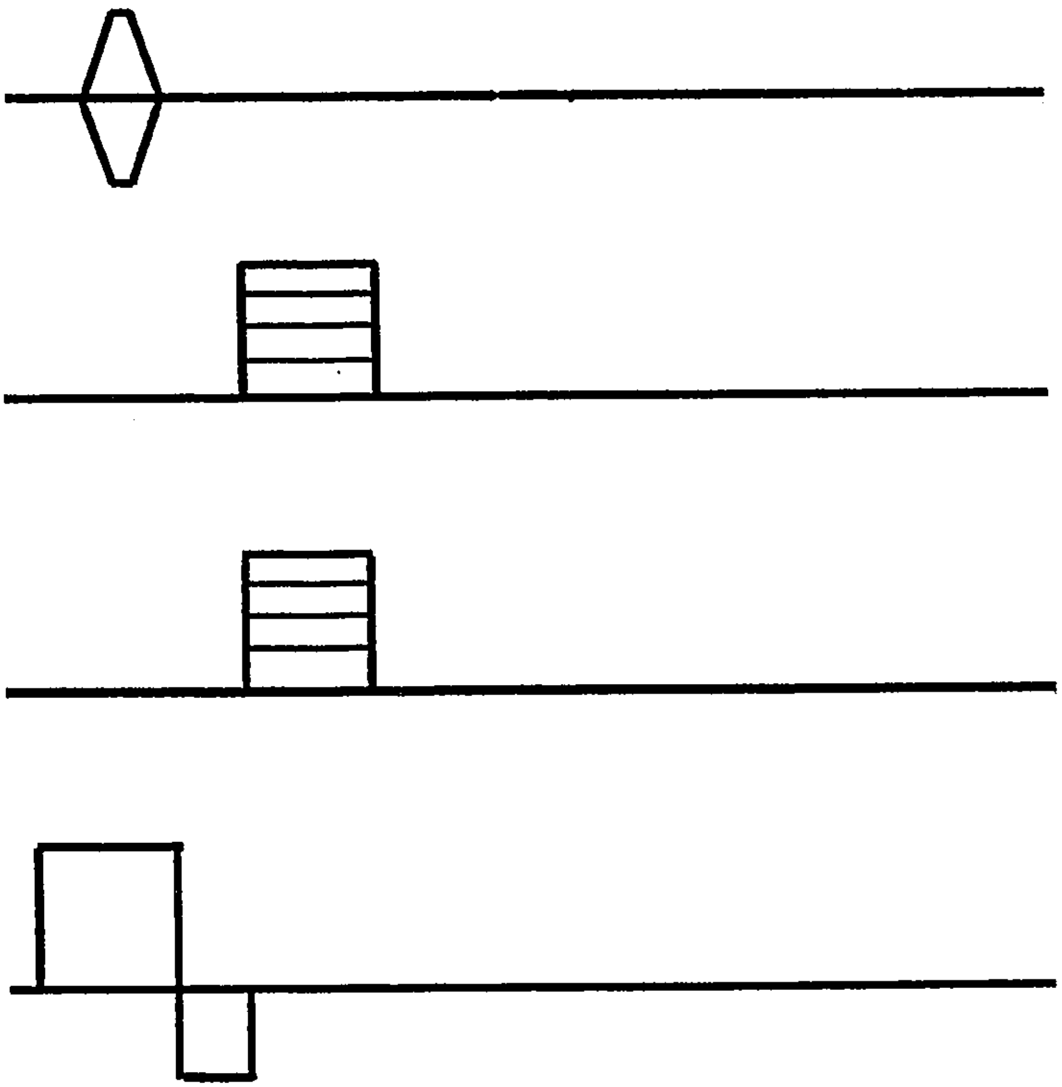

Figure 2.11: Two dimensional chemical shift imaging sequence with slice selection in the third spatial dimension.

different volumes. The problem is greatest for nuclei with a large chemical shift dispersion and when fine spatial resolution is required with low gradient strength. A further difficulty is the loss of signal intensity caused by T_2 relaxation during the slice-select pulse.

One of the earliest papers to have been published using ^{31}P spectroscopic imaging in a clinical setting was by Lenkinski _et al_ (49). A plane was selected with a frequency selective pulse in combination with a gradient and pulsed gradients were used in the two other dimensions. The three dimensional fourier transform yielded spectra related to specific voxels. One modification to the technique used by Haselgrove _et al_ (44) was that Lenkinski _et al_ (49) did not use a spin echo. The necessary delay between the 90° pulse and acquisition, due to the gradients, caused large first order phase errors and loss of signal due to ATP as a consequence of its short T_2 value. Despite these limitations the spectral data were shown to be quite useful in two preliminary cases. The spectroscopic imaging of a patient with a meningioma distinguished between tumour and normal brain on the basis of levels of phosphocreatine and inorganic phosphate.

2.3. Other Localization Methods

There are many other approaches to the problem of generating localized phosphorus NMR spectra and those most commonly used for phosphorus will be mentioned briefly here.

One early method (50) exploits the relationship between B_1 and the distance from the surface coil. If a sample is in a B_1 field whose strength varies linearly with distance a transmitter pulse will cause the nuclear spin to rotate through an angle dependent on the strength of, among other things, B_1. The angle will define where a particular spin is located with spins at positions of higher B_1 precessing through larger flip angles. If a set of spectra is acquired with the pulse length systematically incremented, the amplitude of any spectral line will vary at a frequency determined by the strength of B_1 and hence its distance from the surface coil. One significant drawback of this method is that the shape of the slices are irregular because, while the coil produces a linear gradient along a line drawn from the centre of the coil, the field lines are best described as spherical. Another important problem with this method is the large radio-frequency power deposition required. The application of this technique to a human subject was done by Styles <u>et al</u> (51) in 1985.

CSI and the B_1 technique discussed above can be used to generate a map of the tissue. The other commonly used technique is based on the manipulation of the magnetization such that at the end of the pulse sequence only the signal from the volume of interest is sampled. ISIS (image selected in vivo spectroscopy) which has shown great promise, especially applied to the problem of evaluating brain tumours, was developed by Ordridge (52). ISIS is a single voxel technique which results in the acquisition of one spectrum from the defined volume of interest. This is a different approach to localization than that used in mapping techniques such as CSI. Mapping techniques obtain data from many voxels and this data can be reconstructed to provide a "map" of the area covered by these voxels. If comparison to surrounding tissue is desired, a mapping technique will be the method of choice. ISIS is based on the principle of slice selection using gradients as discussed above. Using a 180° pulse and a slice select gradient, the magnetization of a portion of the sample is inverted and then subjected to a 90° pulse. If this is subtracted from the magnetization from the whole sample (after a 90° pulse) then the remaining magnetization should be only from the slice. A vector diagram explaining the one dimensional experiment is shown in Figure 2.12. If this is repeated in three dimensions with the appropriate subtractions and additions of signals, signal from the desired cubic voxel should be obtained. ISIS

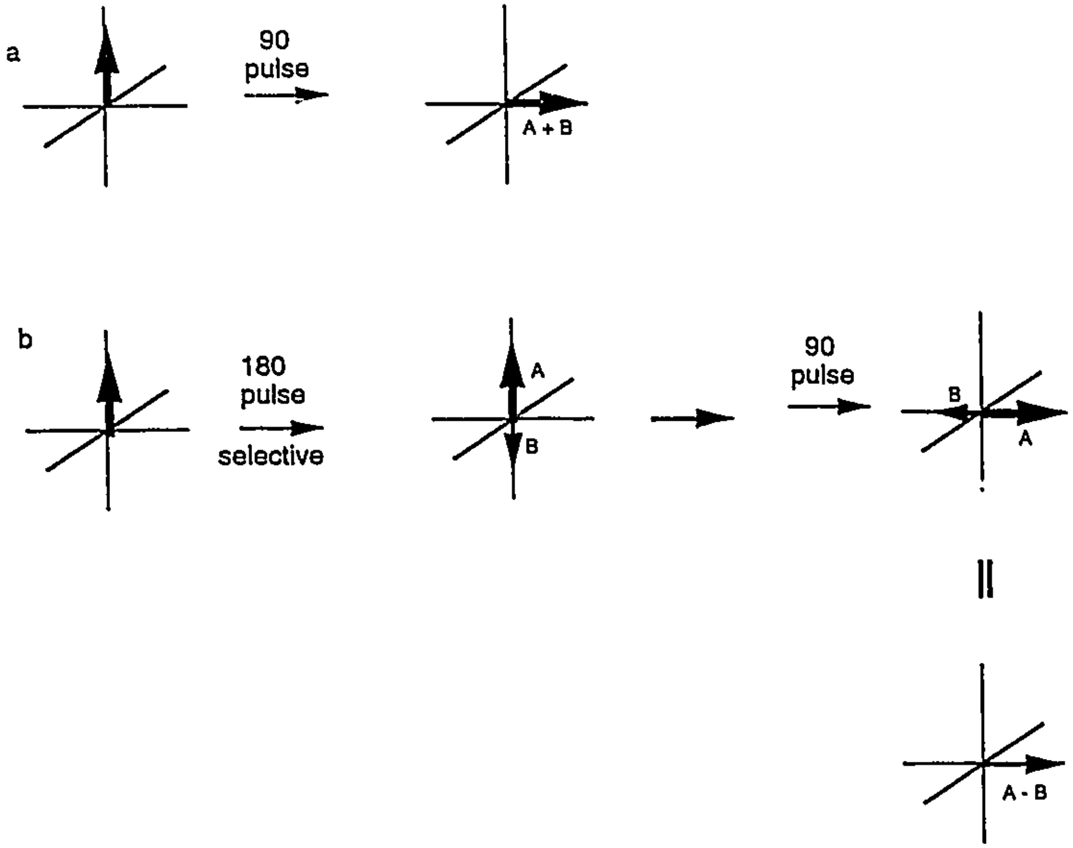

Figure 2.12: Vector diagram explaining a one dimensional ISIS sequence. The results of a and b are subtracted to yield 2B (which is signal from the area selected by the 180° selective pulse).

suffers from the frequency shift due to chemical shift and also from contamination problems due to imperfect additions and subtractions.

An interesting combination of the two methods discussed in this section is the FLAX-ISIS technique (53) which was used to investigate the heart wall in dogs. FLAX-ISIS uses two dimensional ISIS to define a column and than uses the B_1 technique to obtain voxels along the column.

CHAPTER 3

Proton NMR of Human Tumours: Background

Proton NMR of human tumours *in vivo* is more difficult technically than phosphorus NMR because the large signal from water must be suppressed in the proton spectra before any other compounds can be observed. In terms of signal to noise, however, proton spectroscopy has a large advantage over phosphorus. NMR studies of human brain tumours have been performed on extracts and *in vivo*. The *in vivo* studies have been useful in characterizing brain tumours and increasing our understanding of their metabolism. In humans *in vivo* ^1H NMR spectroscopy is still limited to techniques which yield one dimensional proton spectra. For this thesis, high resolution NMR was performed *ex vivo* on biopsy samples of human brain tumours. Because the spectroscopy was not *in vivo*, techniques such as the two dimensional COSY and T_2 determination were technically possible. These techniques, applied to other forms of cancer, have yielded information regarding the malignancy of the tissue observed (3).

3.1. 1D Proton Spectroscopy of Human Brain Tumours

An *ex vivo* proton spectrum from a tumour is shown in Figure 3.1. The number of peaks in this spectrum makes it difficult, if not impossible, to identify each peak. With the improved resolution of extracts (c.f. Chapter 8) even more peaks can be distinguished. The number of compounds can be overwhelming; therefore, only those which appear to discriminate between normal and cancerous brain tissue will be discussed.

In an early paper Nadler and Cooper (54) used spectrophometric techniques to demonstrate low N-acetylaspartate anion (NAA) in astrocytomas and meningiomas. They postulated that low NAA levels were caused by the lack of neurons in the pathological tissues and that NAA might be a neuronal marker. Lowry *et al* (55) showed low total creatine (creatine plus phosphocreatine) levels in gliomas and meningiomas.

The advent of *in vivo* proton NMR spectroscopy of the human brain stimulated proton NMR studies of extracts to explain the *in vivo* data. In a study by Gill *et al* (56) in 1990, perchloric acid extracts were made from biopsy samples of human tumours and normal tissue. Consistent with the

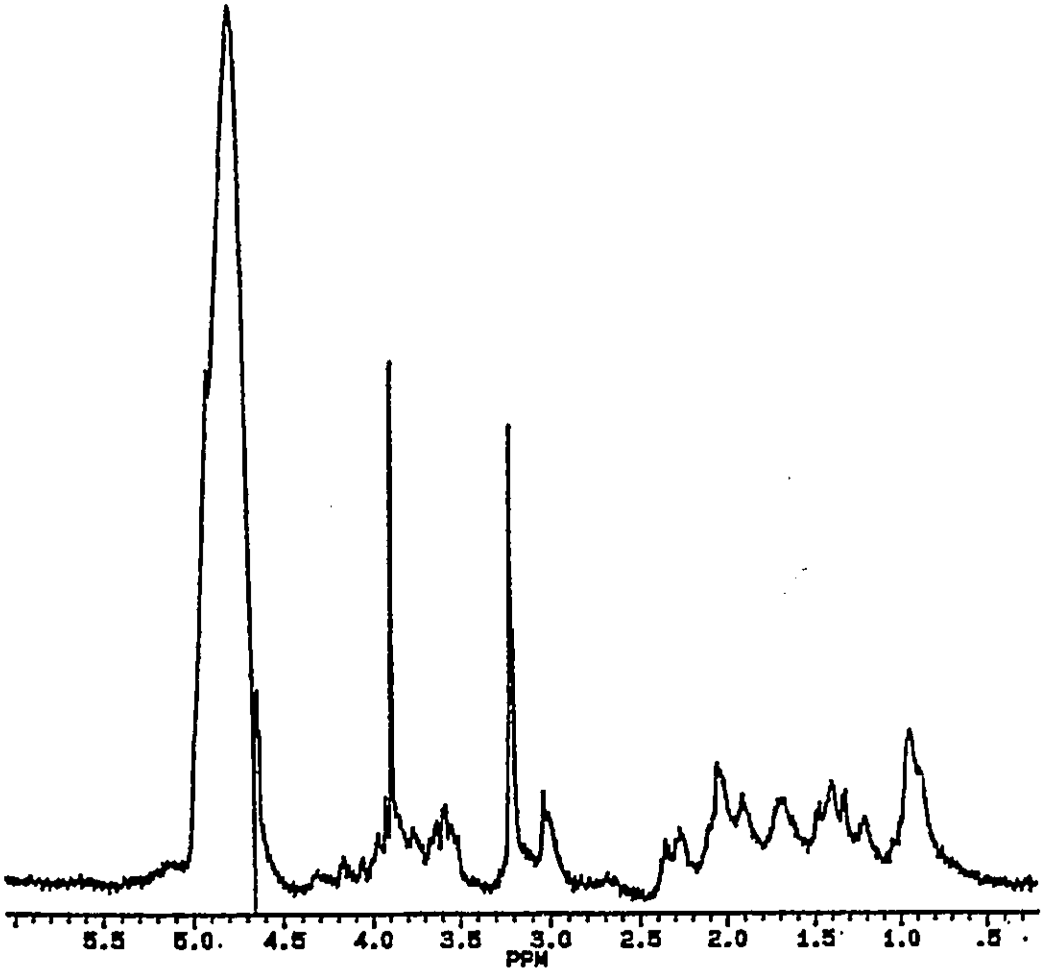

Figure 3.1: Proton NMR spectrum of a human brain tumour *ex vivo*.

non-NMR papers discussed above, total creatine and NAA levels were reduced in astrocytomas of all grades, as compared to normal brain tissue. The ratio of alanine to creatine was increased in meningiomas. The choline to creatine ratio was found to be useful in defining the degree of malignancy in astrocytomas. This ratio increased with increasing malignancy, and grade IV astrocytomas had values significantly higher than normal tissue and the lower grades of astrocytoma. It may be hypothesized that the increase in choline concentration is related to a different turnover in tumour tissue as compared to normal tissue of the phospholipids. The choline peak may include some of the same compounds represented by the PME peak in the phosphorus spectra (c.f. section 2.1.), such as phosphocholine. A proton NMR study of extracts of infant brain (57) indicated that the ratio of choline to creatine decreases with age. This suggests an increase in this ratio may be somehow indicative of the dedifferentiation characteristic of malignant tumours. Ratios of NAA to both creatine and choline increased with age. Studies with developing rats have shown that the increase in NAA concentration coincides with myelination (34).

In a recent proton NMR study of extracts of human brain tumours low creatine and inositol levels were found in meningiomas. Peeling and Sutherland (58) also found evidence of abnormal glucose metabolism reflected in low levels of succinate, glutamate, aspartate, glutamine and creatine and generally elevated levels of glycine and alanine in all tumours. Multiple samples were taken from some tumours and malignant astrocytomas and metastatic tumours were found to be more hetereogeneous than meningiomas or benign astrocytomas.

The in vivo proton spectroscopy of human tumours is generally in agreement with the findings from extract studies. Decreased levels of NAA and creatine and increased levels of choline (59, 60) have been found in brain tumours. The lactate anion has generated significant interest in in vivo studies. Its production during freezing makes any data on lactate anion concentration in extracts unreliable. The levels of lactate anions in vivo, however, may yield useful information regarding necrotic and hypoxic areas in a tumour. Arnold et al (61) found that higher lactate anion signals were present in the spectra of the more malignant histological tumour grades as compared to benign astrocytomas. Unfortunately, high lactate anion concentration was found in all grades in other studies (62).

A more detailed study into the significance of the presence of lactate anions was done by Alger et al (63). Using both ^{18}F fluorodeoxyglucose positron emission tomography

(PET) and ^{1}H in vivo spectroscopy the study unsuccessfully attempted to correlate elevated metabolism of glucose with high lactate anion concentration. Brain tumours have increased glucose consumption, as shown by PET, which is postulated to be caused by an increased dependence on glycolysis rather than full oxidation of glucose for ATP generation. Brain tumours which PET indicates have increased glucose utilization, should therefore have increased lactate anion concentration, a product of glycolysis. The study was unable to show this correlation, possibly because of the complexities of the system studied. The level of lactate anions depends not only on its production, but also on its elimination.

Thus far the reproducible peaks obtained in vivo are creatine, choline, NAA and lactate. Other peaks, which may be useful in discriminating tumour from normal tissue, are now being reported. Because it is difficult to identify all the peaks in ex vivo or in vitro 1D ^{1}H spectra, other techniques are used to discrimate between the peaks, and to obtain more information. These are described in the next two sections.

3.2. Two Dimensional COSY Spectra

A 2D COSY spectrum of a human brain tumour biopsy sample ex vivo is shown in Figure 3.2. The COSY experiment spreads out the information from a 1D experiment into two dimensions with each cross peak indicating scalar coupling. The COSY experiment will be briefly described using vector diagrams and some population arguments. A thorough description, which will not be attempted here, requires density matrix theory. It should be noted that there are similarities between spectroscopic imaging (described in section 2.2) and this technique. Both are two dimensional techniques; spectroscopic imaging uses a gradient pulse to encode the spatial information as frequency for the second dimension, while a COSY encodes coupling information in the second dimension with a mixing pulse of 90° degrees.

The basic COSY sequence is composed of two 90° pulses with a variable delay, t, between the two pulses. After the first 90° pulse, the proton vector, in the rotating frame, will precess according to frequency differences from the reference frequency due to chemical shift and also according to couplings to other protons. During the variable delay period, t, in, for example a simple AX system, the A proton will be split into two vectors rotating in the rotating frame at a frequency of $\upsilon \pm J_{AX}/2$, where υ depends on its chemical shift and J is the coupling constant. The period of evolution is t and is followed by the 90° mixing pulse.

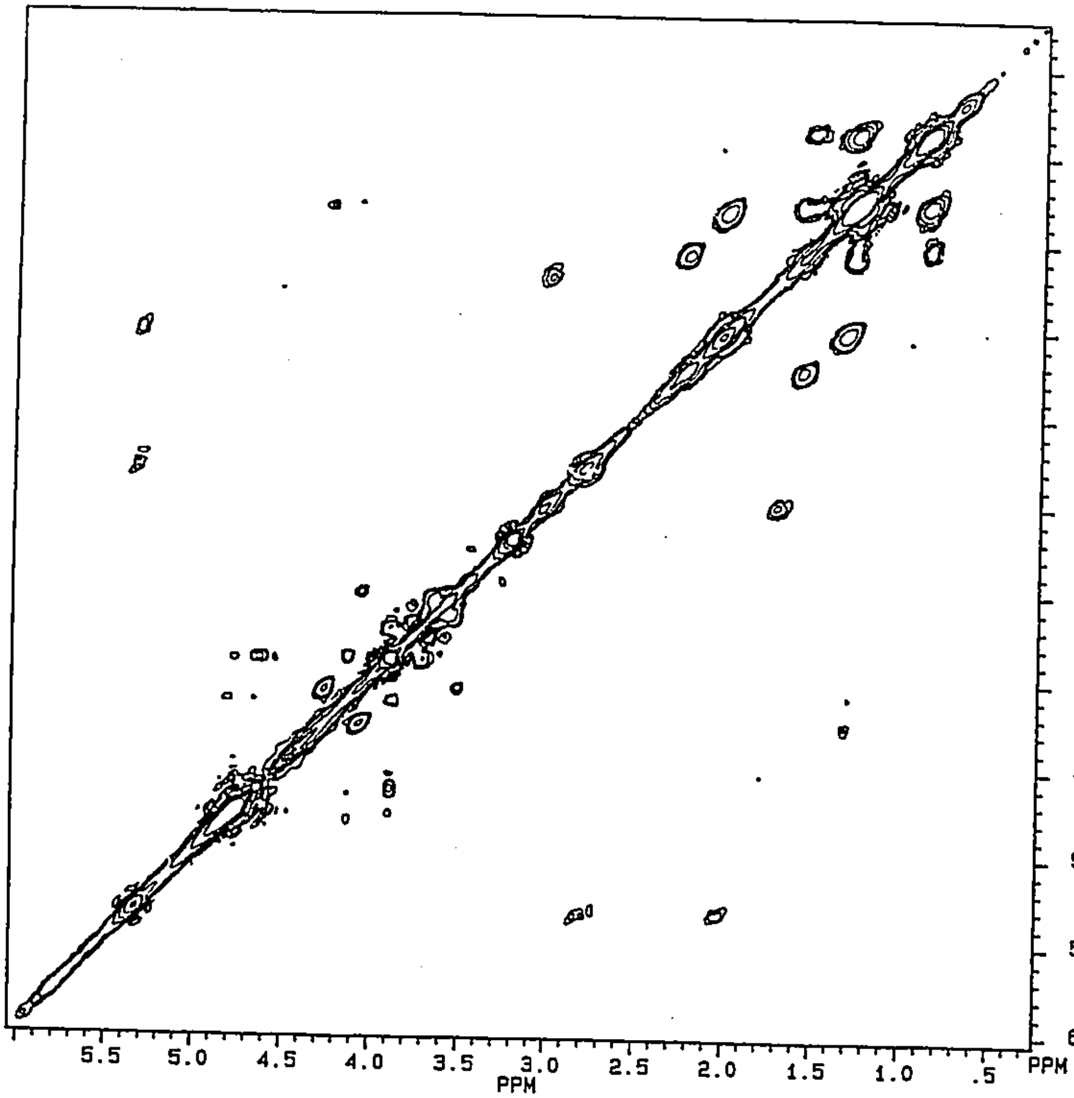

Figure 3.2: Two dimensional COSY spectrum of a human brain tumour <u>ex vivo</u>.

The description of a COSY experiment requires recourse to the populations of the spin systems. If there is no delay between the two 90° pulses, the second pulse will tip the magnetization down to the -z axis, as shown in Figure 3.3. If the vector has precessed to the -y axis then after the 90° pulse the populations are in an unperturbed state. If the delay, t, is long enough to allow a single proton vector to precess back to the y axis, then the z magnetization is inverted by the second 90° pulse; in terms of populations of energy levels, this means the populations of the spin system have been inverted. During the delay, t, the populations of all the connected transitions will be changing with a frequency of υ, the frequency of the A proton. By carrying out a number of experiments in which t is incremented, the intensity of the X proton, in the simple AX system, will oscillate at the frequency of the A proton. Thus the frequency of any coupled protons has been encoded into the amplitude by the mixing pulse. The second Fourier transform, will therefore yield the frequency of any protons coupled to the proton.

Each cross peak in a COSY spectrum indicates a coupling. The information regarding which protons are coupled can aid in the identification of molecules. The power of this experiment as an aid to identifying peaks in biological systems is shown in two papers by Sze and

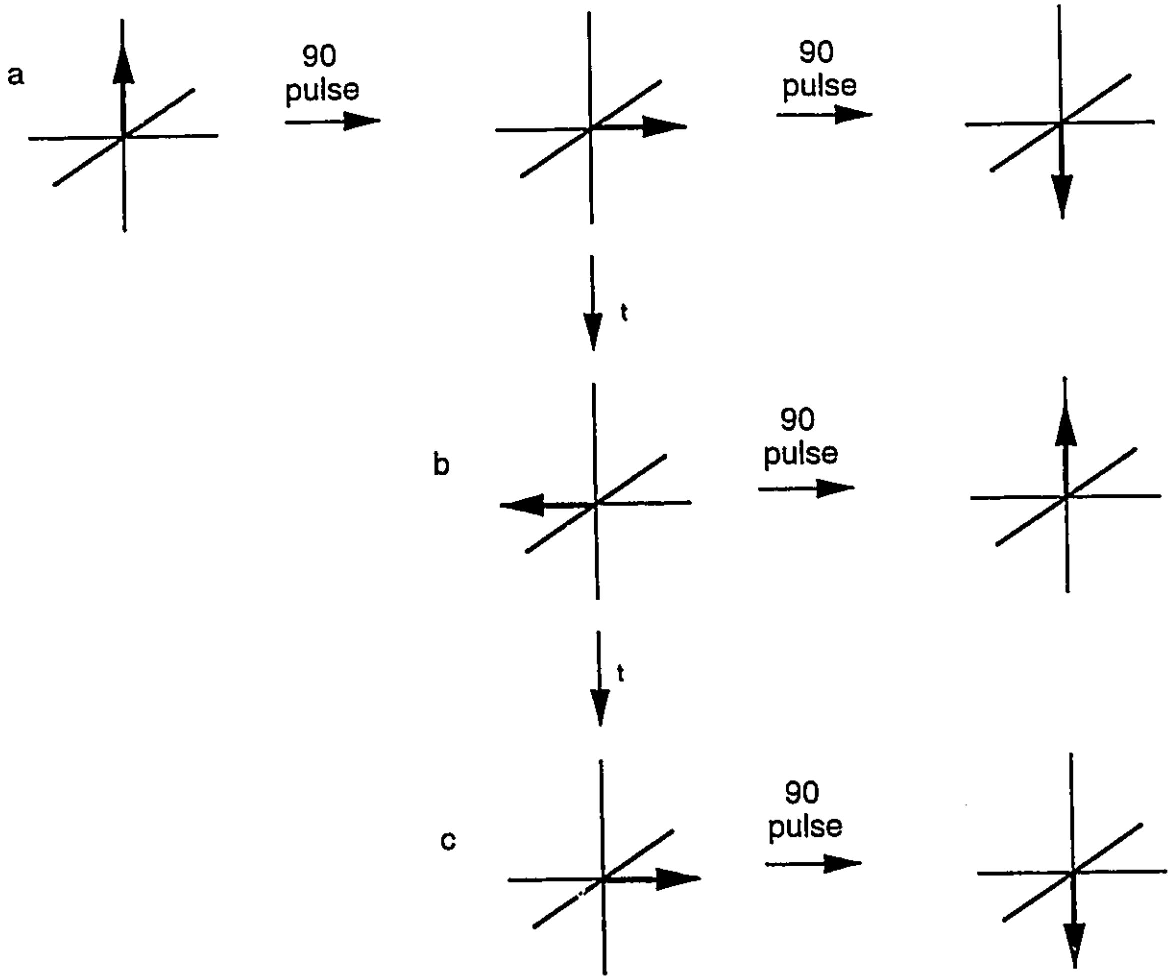

Figure 3.3: Behaviour of a proton vector of frequency, υ, in a 90° - t - 90° COSY sequence where a) the second pulse is applied immediately after the first, b) the vector has precessed to the -y axis before the second pulse is applied and c) the vector has precessed back to the y axis, during the delay t.

Jardetzky (64, 65). Metabolites, nucleotides and lipids were all identified in extracts of human lymphocytes and changes during proliferation were monitored. COSY experiments can also be useful for *ex vivo* samples. Mountford *et al* (66) used COSY experiments to distinguish normal and malignant tissue. In a study of uterine cervical punch biopsy samples (3), significant differences in COSY spectra of malignant tissues versus normal were found. Certain cross peaks, possibly fucose and/or threonine, which are in malignant tissues, were also seen in the precursor stages of cervical cancer, but not in normal cervix samples.

The first *in vivo* COSY of brain was published by Barrere (67) in 1990. A number of cerebral metabolites in the rat brain, such as aspartate, inositol and taurine, some which could not be resolved using conventional 1D ^{1}H NMR were assigned. Another COSY spectrum was taken after ischemia of the brain, and changes in the metabolites were noted. The 2D COSY experiment has been demonstrated to be a powerful tool for sorting through some of the complexities of brain metabolism.

3.3. T2 Measurements in Cancerous Tissues

Relaxation of the magnetization, as mentioned in section 1.3, is by two processes. Longitudinal relaxation is the restoration of the magnetization to the z axis and is caused by the transfer of spin energy to the lattice. Transverse relaxation describes the dephasing in the x-y plane caused by the transfer of energy between the spins and by field inhomogeneity. The major mechanism for relaxation in proton systems is generally dipole-dipole relaxation, caused by fluctuations of the magnetic dipoles with the motion of molecules. The size of the magnetic moment, the distance between the two dipoles and the effective correlation time all affect this relaxation mechanism.

The longitudinal time constant is shortest when the motion is at the Larmor frequency and increases for shorter or longer correlation times. The transverse time constant, T_2, coincides with T_1 for faster molecular motion, but for molecules tumbling with slower rates of motion than the Larmor frequency, it decreases. The transverse time constant determines linewidth. This thesis is concerned with T_2, and only its measurement will be described.

The transverse relaxation is sensitive to inhomogeneities in the magnetic field and, therefore, to obtain the natural T_2, as opposed to T_2^*, the Carr-Purcell spin echo can be used. To eliminate the further problem of inaccurate 180° pulses, the Carr-Purcell-Meiboom-Gill pulse sequence is used to measure T_2. The sequence begins with a

90° pulse, which is followed by

$$(t - 180_{\pm y} - t)_n.$$

The spins begin to dephase in the first time interval and then in the second interval after the 180° pulse are refocussed. By repeating the sequence for many different value of n, the loss of intensity of the spins caused by T_2 can be monitored at various times. If the data are plotted, a value for the time constant can be obtained. Given the complex nature of the environment the molecules are in, it is commonly found that two or more time constants are required to describe the decay in *in vivo* and *ex vivo* samples.

The first hint that relaxation time measurements might be useful in the discrimination of cancerous tissue from normal tissue came with Damadian's paper in 1971 (68). T_1 and T_2 values for water in excised cancerous rat tissue were found to be twice those found in normal tissue or benign tumour tissue. Two explanations for these long relaxation times have been: 1) the different water content of pathological tissue; and 2) paramagnetic ions bound in normal but unbound in tumours (67). Although, the long relaxation times were not verified by subsequent reports, a fruitful avenue of research had been opened.

In 1984, Mountford et al (70) reported data on two rat mammary carcinoma cell lines; one metastatic, the other malignant but non-metastatic. The proton spectrum of the metastatic line had a component with a very long T_2 component, at 1.3 ppm, which was not found in the spectrum of the non-metastatic line. The signal at 1.3 ppm was a fairly narrow resonance in the proton NMR spectra of cancer cells and was assigned to the fatty acyl chain of membrane lipids (71). These lipids are in or attached to the plasma membrane and tumble isotropically. When human tumours were studied, long T_2's of the resonances at 1.3 ppm, were found in biopsy samples of human ovarian and colonic tumours (72). Another research group found that malignant breast tumours could be characterized by a very long $T_{2,}$ also in the lipid region of the spectrum (73). Thus, a long transverse relaxation time appears to be characteristic of cancer in a number of tissues in both humans and animal models.

CHAPTER 4:

Application of 1D CSI to the Magnetom

Installation of the one dimensional chemical shift imaging sequence on the Siemens Magnetom was necessary before any work with brain tumour patients could be done. A basic 1D CSI sequence was obtained from Dr. W. Negandank in Detroit (74), but this sequence was not suited for the Magnetom at the Ottawa General Hospital or for the application desired, analysis of human brain tumours. This chapter will describe the development of the technique and the final sequence used.

4.1 Materials and Methods

The imager at the Ottawa General Hospital is a Siemens Magnetom version GBS2 with a 1.5 T magnet. The maximum gradient strength is 10 mT/m and the gradients can be ramped at approximately 10 mT/m in 1 ms. The computer is a VAX 11/750 manufactored by Digital Equipment Corporation and the imaging operating software is NUMARIS D1.3. The sequence generator used on the Magnetom is version D1 of PARGEN. The imager was equipped with the spectroscopy option in 1988. All data manipulation was performed using the FTNMR software package, modified for NUMARIS files, which accompanies the spectroscopy package. The surface coil used was a 9 cm diameter coil with 2 turns. The coil was designed and built by Paul Morris Instruments Ltd, Ottawa.

The surface coil was manually tuned but the body coils of the Magnetom tuned automatically. The sample, whether phantom or patient, was positioned on the table, or bed of the imager. An alignment light indicated the position on the bed which would be placed in the isocentre of the magnet in the x and z direction. For this magnet, the z direction is designated as being along the bore of the magnet, the x is horizontal and y is the vertical direction. Tuning of the surface coil was performed before the sample or subject was moved into final position, but the body coil was tuned automatically once final positioning was complete. After tuning, shimming was performed by using the body coils to transmit. Although the surface coil was tuned to phosphorus during shimming enough proton signal was obtained to shim on the FID of water. Adjustments of frequency and transmitter power for the CSI experiment were generally determined by obtaining an spectrum, localized only by the surface coil, once shimming was completed. If images were obtained, the sequence SESMS, a simple T_2 weighted imaging sequence was used. The sequence is reproduced in Appendix 1.

Once the CSI sequence was completed the raw data were transferred to the FTNMR program. A program was written in FTNMR which converted the raw data from a serial file into a matrix file and then line broadened and Fourier transformed the data in one dimension. The program, named AR2, is reproduced in Appendix 2. A second program which performed the second Fourier transform was used after AR2. This program, AR11, is also in Appendix 2. The final matrix was usually 32 by 1024. The program FTNMR was incapable of performing a Fourier transform on less than 32 points, thus, the spatial dimension was zero filled to 32 before the 2D Fourier transform. For a 16 step CSI experiment only every second spectrum was used and for an eight step, only every fourth spectrum was used. Routines were written to display the appropriate number of spectra. After the spectra were displayed, those spectra which contained signal were manually phased. The first order phase correction was in the range of -1600°. Once the first order correction was done, the zeroth order value could usually be determined visually.

The following compounds were used in making phantoms: orthophosphoric acid (H_3PO_4) 85% obtained from BDH Chemicals, dimethylmethylphosphonate (DMMP) from Aldrich Chemical Company, Inc., phenylphosphonic acid (PPA) from Aldrich

Chemical Company, Inc., and sodium phosphate $(Na_3PO_4)\cdot 12H_2O$ from Anachemia. Solutions were prepared in concentrations ranging from 0.05 to 1.0 M depending on requirements. Phantoms were made by adding these solutions to sealed petri dishes, vials and bottles of various shapes.

4.2 Results and Discussion

The one dimensional chemical shift imaging sequence used is shown in Figure 4.1 and was based on sequence published by Brown et al (75). The radiofrequency pulse was adjusted to 250 μs. This yielded maximum signal at depth of approximately 3 cm in the human brain when a transmitter voltage of 40 V was used. The rise and fall times of the gradients were 540 μs.

Once the gradient, or more specifically the area under the gradient pulse, which would be consistently used was determined, (see below) square pulses and various triangular pulses were experimented with. As discussed in section 2.2., perfectly shielded gradient coils would produce gradient pulses which have no eddy currents which could affect the acquisition of spectra. The Magnetom was not actively shielded, and furthermore, perfect shielding is impossible to obtain. Thus, gradient pulse must be used carefully in sequences to ensure they do not affect spectral quality

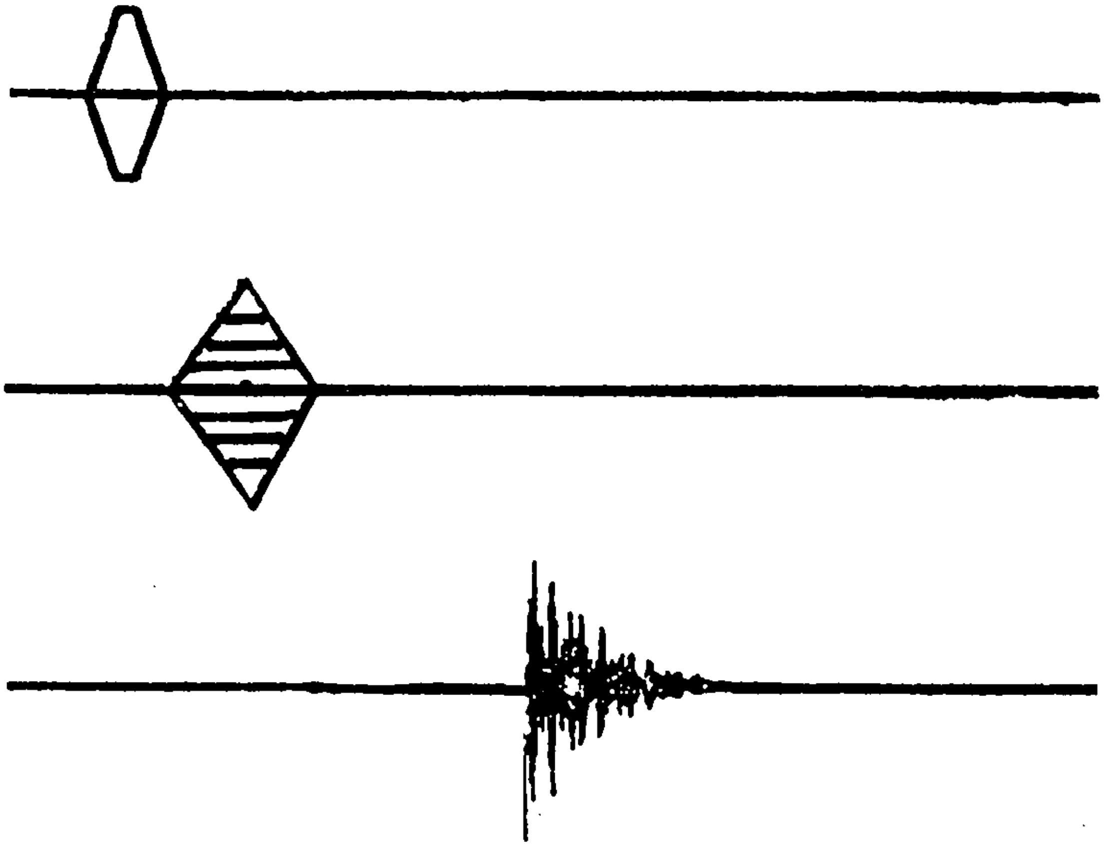

Figure 4.1: One dimensional chemical shift imaging sequence.

beyond what can be tolerated. The gradient system could accomodate slightly faster rise times than the 540 μs used, but it was found that gradient settling was affected by not only the maximum value of the gradients, but also, the speed at which they were ramped. Furthermore, at the maximum ramp time, errors in the final shape of the pulse are more likely to occur. The triangular-shaped pulse with rise and fall times of 540 μs was found to be the most reproducible, and was used consistently in the _in vivo_ experiments.

A compromise between minimum gradient artifacts in the spectra and minimal signal loss during the delay resulted in a final delay before acquisition of 835 μs. A number of experiments were run in which the delay was reduced until artifacts were too large. The delay was readjusted when _in vivo_ studies were started. The number of phase encoding steps and the gradient strength depended on the sample size and resolution required.

Before more specific concepts in the application of CSI are discussed the results of a basic experiment will be shown. Figure 4.2 shows a spectrum taken from the phantom illustrated. Because this is a standard NMR experiment, only chemical shift information is available. The peaks represent, starting downfield PPA, Na_3PO_4, and H_3PO_4. A chemical shift experiment, in the y direction, was run on

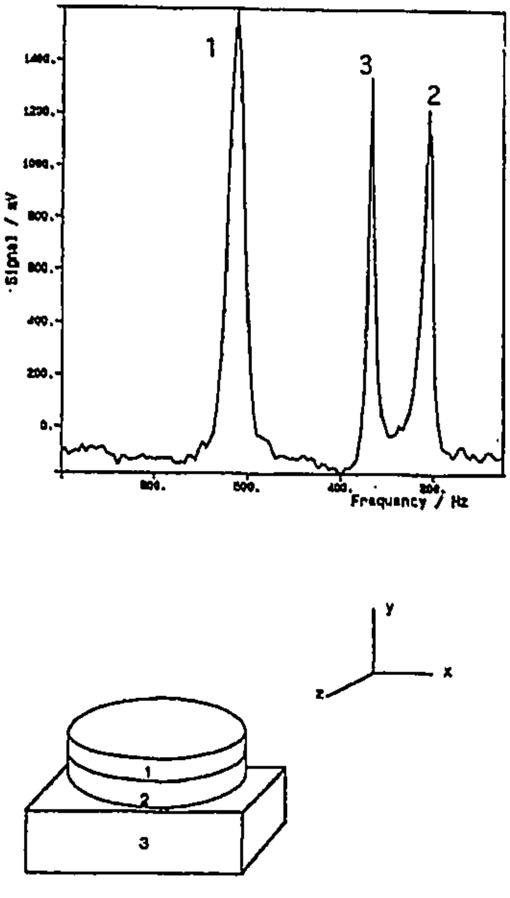

Figure 4.2: An unlocalized spectrum of the phantom using the 9 cm surface coil and a diagram of the phantom. The peaks are numbered according to which part of the phantom they originate from, but note that no spatial information is present in the spectrum.

these same phantoms, and, as shown in Figure 4.3, chemical shift and spatial information was obtained. A number of experiments were run to determine the appropriate adjustments for the most significant parameters and to verify the sequence was performing properly. These will be discussed below.

The general theory of spectroscopic imaging was discussed earlier in this thesis but additional practical details are required for the application of the theory. The Nyquist theorum governs the relationship between sweep width and dwell time (time between sampling) in high resolution spectroscopy. The theorum states that the highest frequency must be sampled at least twice per cycle to be reproduced faithfully. In the CSI experiment (44, 76), this means that the gradient increment between steps must be small enough such that one half a cycle or less occurs for the maximum frequency. The maximum frequency is at maximum gradient strength, G_y, and, at the maximum sample size, y_o.

$$\int y_o \; \gamma \; G_y/\text{steps} \; (t) \; dt = \pi$$

If the gradient pulse is square, the equation relating gradient strength, sample size, gradient time on and number of steps is:

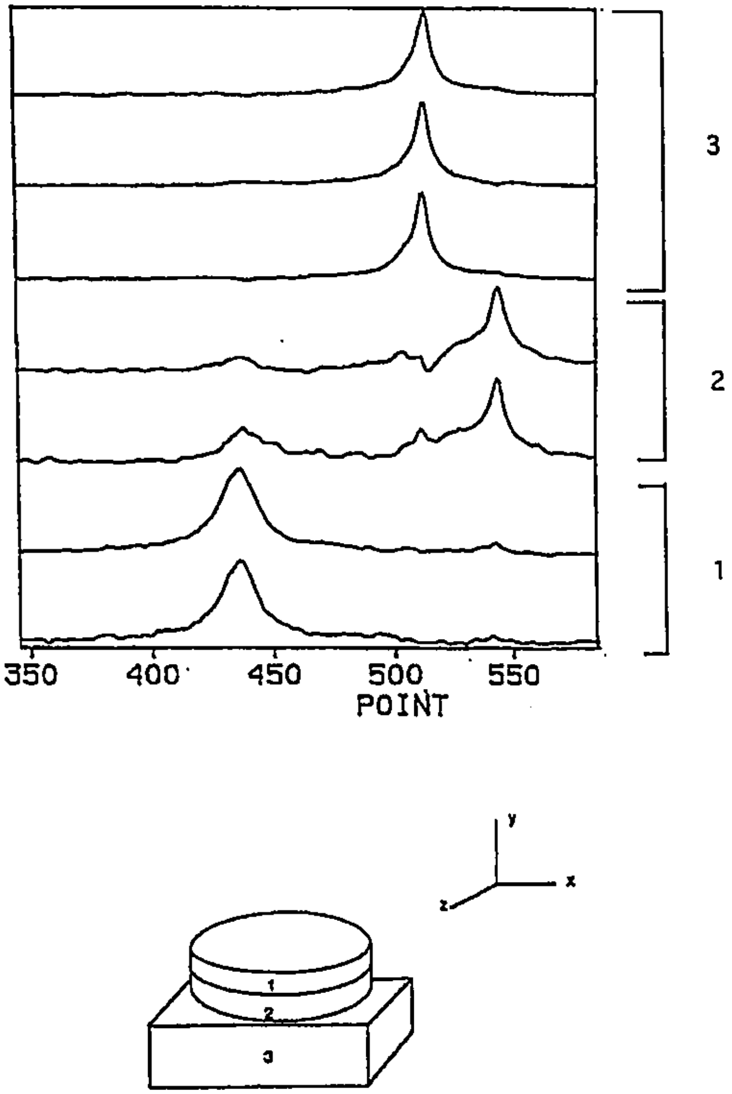

Figure 4.3: The one dimensional chemical shift imaging spectra and a diagram of the phantom used. Note that spatial information is present in the spectra as indicated by the numbering of the phantoms and spectra.

$$G_y y_o t/\text{steps} = 1/2.$$

The calculation is also simple for the phase encoding gradient of Figure 4.1, where the area is a triangle. Because the encoding is in phase information, the detection is analogous to quadrature detection and the equation for sample size or field of view becomes, for a square gradient pulse:

$$y_o = \text{steps}/G_y t.$$

If any signal is detected by the surface coil outside the field of view, it will be folded into the set of spectra in the wrong place. The resolution, for these experiments, is the maximum sample size divided by the number of steps.

The effect on the final data set of repeating the same experiment, but changing the number of steps, is illustrated in Figure 4.4. The spectra represent the results of two CSI experiments. Three phantoms, each containing a different phosphorus compound, were stacked on top of one another in the y direction. The surface coil was placed on top of the phantoms, and a CSI experiment was set up with the phase encoding gradient in the y direction. The gradient strength

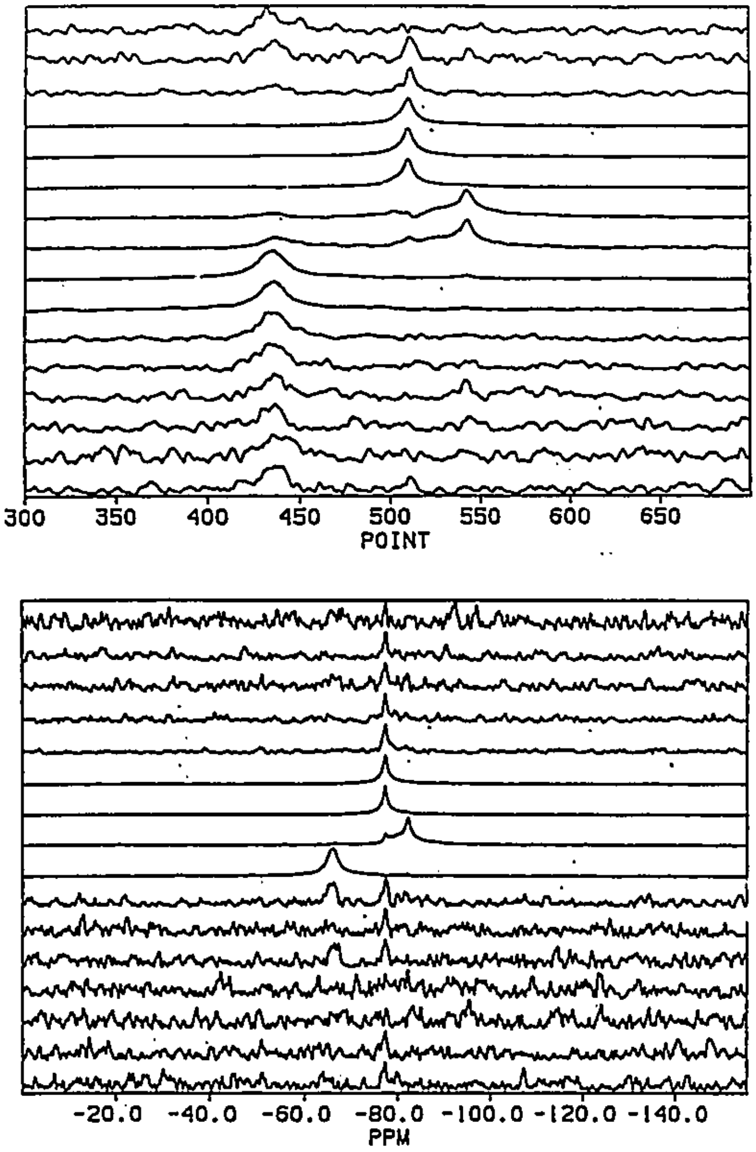

Figure 4.4: Data from two CSI experiments taken of the same phantom consisting of three phantoms each containing a different phosphorus compound, stacked on top of each other. The effect of changing the number of steps of a CSI experiment is demonstrated. The top data were taken with eight steps and the bottom with sixteen steps. Note that the field of view is increased two fold for the sixteen step experiment.

was set such that the sample size was larger than the length of the stacked phantoms in the y direction for eight phase encoding steps. The CSI experiment was repeated with sixteen phase encoding steps. In the eight step experiment the field of view was smaller and about half of the spectra show signal and half are only noise. In the second experiment the effect of doubling the number of phase encoding steps doubles the field of view and therefore signals from the stack of phantoms are in only approximately one quarter of the spectra, with the rest of the spectra being noise only. Each spectrum in the second experiment represents twice the length in the y direction when compared to the first experiment. Halving the maximum gradient strength would have the same effect as doubling the number of steps in terms of sample size, but this would cut the resolution in half. Note that the experiment will take twice as long if the number of steps is doubled and no other changes are made to the sequence.

In order to perform a CSI experiment, it is not enough to know the field of view and the resolution: the placement of the field of view must also be known. The centre of the set of spectra will be the position at which the gradients always have a value of zero. Gradient coils are designed to place this position at the centre, or so called isocentre of the magnet. Thus, the experiment must be set up such that the sample is approximately centred at the isocentre. The further away the sample is positioned from the isocentre, the larger the field of view must be set to eliminate folding. The effect of physically moving the sample in the magnet is shown in Figure 4.5.

The first set of spectra in Figure 4.5 is the same experiment discussed above, with sixteen phase encoding steps. Before the experiment was repeated the set of phantoms was physically moved in the magnet in the y direction. The surface coil was moved at the same time to ensure no loss of signal ensued. The signal received is limited not only by the CSI experiment, but also by the ability of the coil to receive the signals. The B_1 field of the surface coil extends to approximately 6 cm in depth. The spectroscopic imaging experiment was repeated in the y direction and the results are shown in the second part of Figure 4.5. As would be expected, the placement of the signals from the phantoms has been changed in the series of spectra. In the example shown, the phantoms were still within the field of view and their location was faithfully reproduced. If the experiment had been repeated with eight phase encoding steps, a portion of the sample would have been outside of the field of view and consequently the peaks would have been folded into the series of spectra into the wrong position.

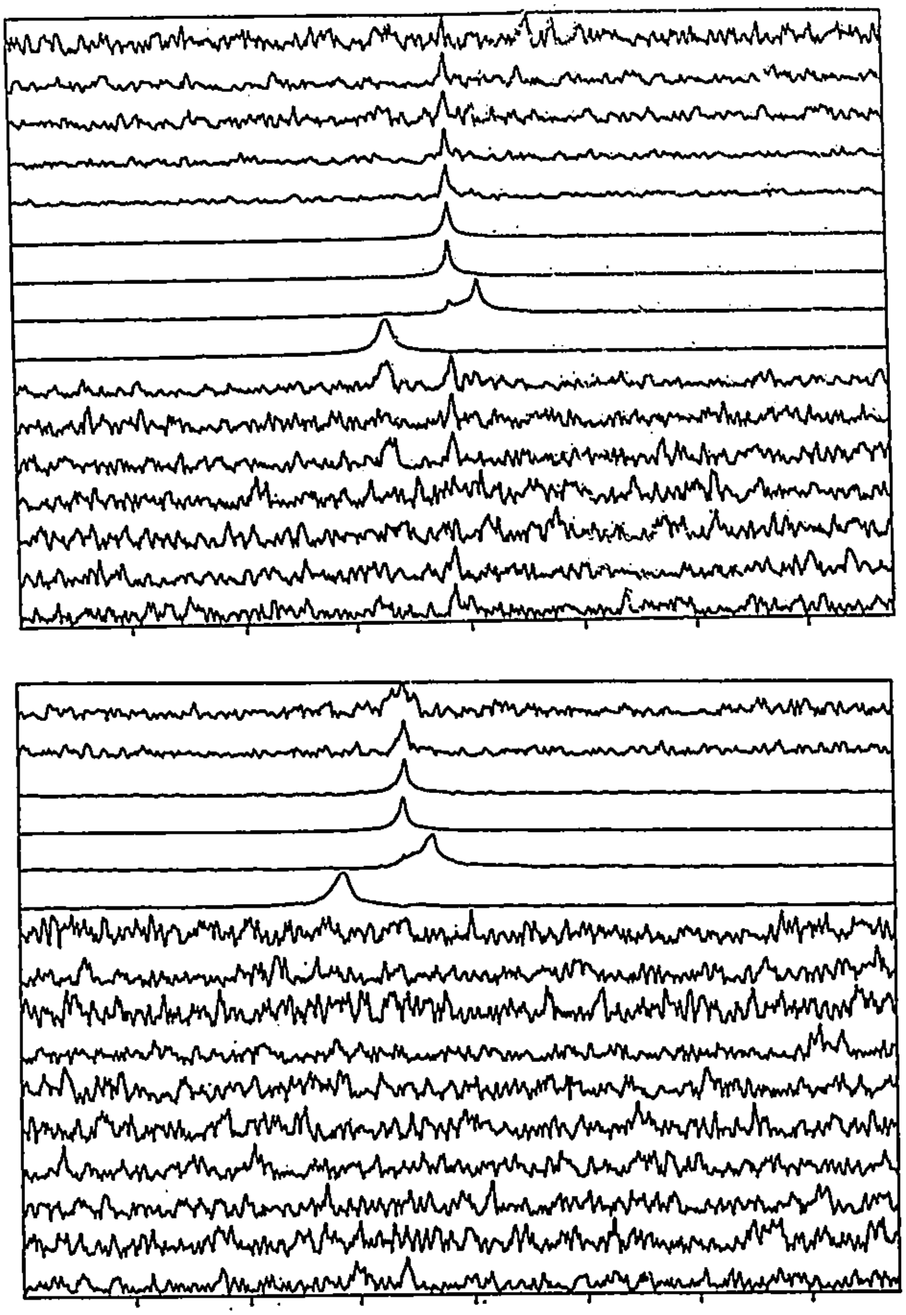

Figure 4.5: Demonstration of the effect of moving the phantom with respect to the isocentre of the magnet. Two identical CSI experiments were performed with the same phantom.

The fact that the CSI spectra are centred at the isocentre of the magnet is a significant advantage. Magnetic resonance images, usually based on water content, are obtained using similar techniques, i.e. phase encoding and read gradients. Therefore they are also centred at the isocentre of the magnet. The Magnetom, like most imagers, is capable of overlaying, on any of its images, a grid designating the isocentre. Actual distances have also been calibrated and thus the grid indicates the isocentre and actual distances from the isocentre on the image. The calibration of the distances on the Magnetom images was regularly checked in standard quality control procedures.

Figure 4.6 shows an image taken of a set of phantoms used to verify the spatial accuracy of the spectroscopic imaging sequence. The vertical axis is designated the y axis and the horizontal axis is x. The image represents a 6 mm slice taken at a position where z equalled 7.2 mm. The grid numbers are centimeters from the isocentre. The small vial at the bottom (y=-5 cm) was filled with PPA and served to indicate the location of the 9 cm surface coil. The surface coil was centred underneath the set of phantoms, and was lying flat in the x-z plane. The larger square bottle was filled with Na_3PO_4 and was placed in the range from -4 cm to -1 cm in the y direction on the image. A petri dish which

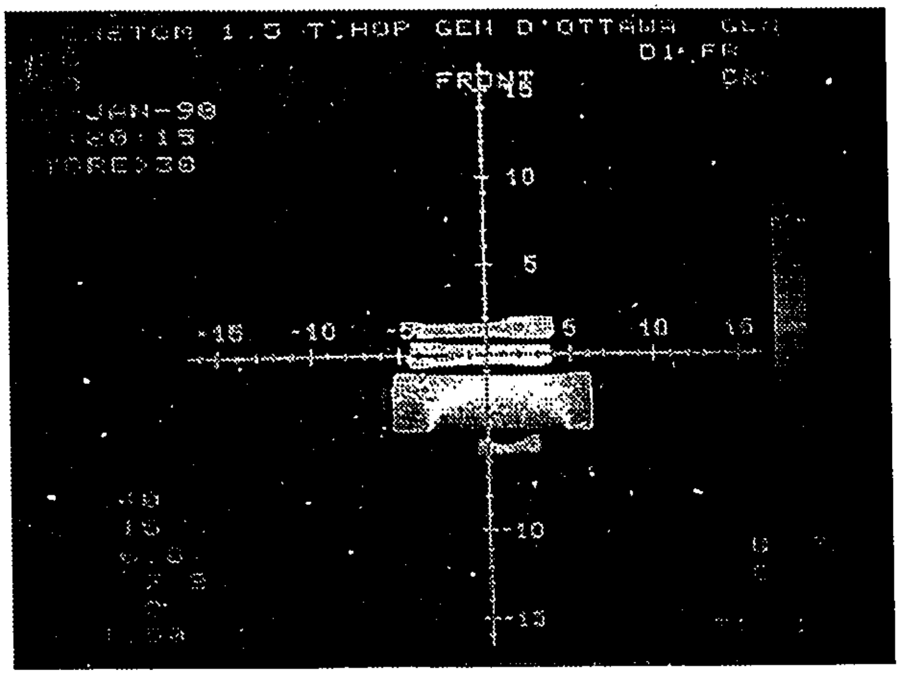

Figure 4.6: Image taken of phantom (CSI spectra in Figure 4.7) with grid indicating spatial dimensions and the isocentre.

was filled with H_3PO_4 was located at the isocentre. The final phantom was a petri dish filled with PPA and was located at approximately 1 cm above the isocentre. The darkening of the image at the larger square bottle also served to indicate the placement of the surface coil. The darkening was caused by absorption of the radiofrequency by the coil.

A chemical shift imaging experiment with sixteen phase encoding steps was performed in the y direction with the phantoms set up as described above and shown in Figure 4.6. The field of view was 16 cm and each of the sixteen resulting spectra represented 1.0 cm in the y direction. Ten of the resulting spectra are shown in Figure 4.7 and have been numbered. The peaks were all identified by their relative position in the spectra. Starting from downfield, the three peaks are PPA, Na_3PO_4 and H_3PO_4. The spectra were plotted such that the top spectrum (not shown) represented the bottom CSI voxel. Each spectrum represented the signal from a disk-shaped voxel which was 1 cm thick and which had an approximate diameter of 9 cm. The field of view must be centred on the isocentre and therefore covered the area from -8 centimeters to +8 centimeters in Figure 4.6. Spectrum 3, for example, covers the area from y values of -6 cm to -5 cm. The small vial of PPA was in that voxel of the image and therefore, a peak representing PPA is in spectrum 3. Spectra 4 to 7 covered the area in which the large bottle of Na_3PO_4

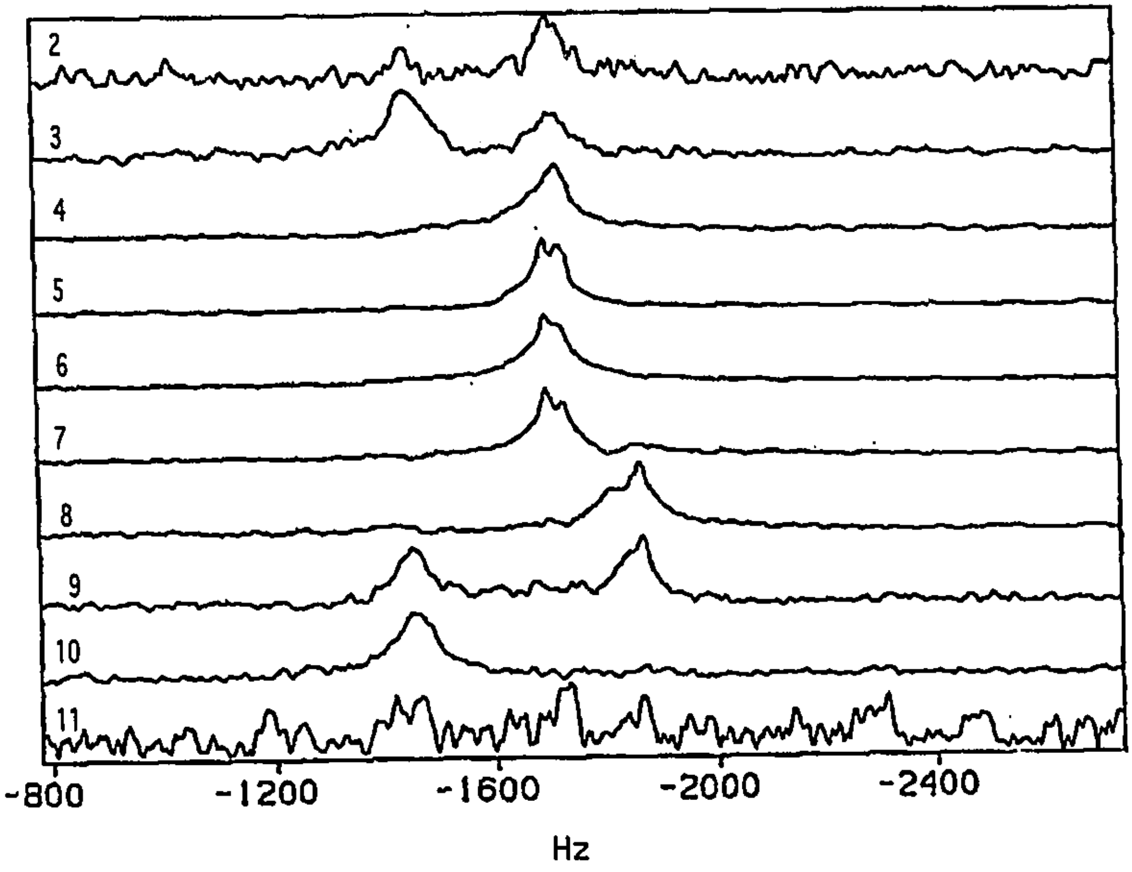

Figure 4.7: Chemical shift imaging spectra corresponding to the image in Figure 4.6.

was located and consequently peaks for this compound were in spectra 4 to 7. Similarly, all aspects of the CSI experiment could be correlated to the image. Combined, the two figures illustrated that the CSI experiment functioned properly on phantoms. The next step was application to human subjects.

The final sequences which were used on human volunteers and patients are reproduced in Appendix 3. The two sequences used with brain tumour patients had sixteen phase encoding steps and maximum gradient strengths resulting in fields of view of 16 cm and 24 cm. The resolution was 1 cm and 1.5 cm per spectrum respectively and the recyle time was 1 s. Before proceeding to obtain CSI spectra of human brain, the sequence was verified in vivo on human liver. Human liver was used because the liver itself does not contain any PCr (77). The overlying muscles, however, contain large amounts of PCr. If the sequence was localizing properly in vivo, it would be possible to obtain a spectrum without a signal from PCr.

To obtain spectra from the liver, the volunteers were placed on the magnet table supine. The 9 cm coil was placed over their right side where the liver was located. In some cases images were taken to verify the position of the liver in the volunteer. A CSI sequence was run using 16 phase encoding steps and gradients adjusted such that each spectrum represented a depth of 1 cm. Two spectra taken from such a set of CSI spectra are shown in Figure 4.8. The two spectra were clearly quite different. The top spectrum was characteristic of liver tissue, with a large PDE peak and a significant PME peak. There was some small contamination from muscle, as can be seen by a small PCr peak, but this could have been caused by inexact localization on the liver or contamination caused by the CSI method itself. The bottom spectrum was clearly from overlying muscle as demonstrated by the dominant PCr peak. The ability to obtain localized spectra in vivo was therefore confirmed.

4.3 Conclusions

The specific protocol used for brain tumour patients will be described in Chapter 5. This chapter has attempted to outline all the important parameters which must be evaluated when CSI experiments are applied to a magnetic resonance imager. The types of experiments, used to verify that the sequence was functioning properly, were described. It is important to realize that a CSI sequence which works on phantoms must be tested in vivo. It is folly to assume that a sequence tested on phantoms will work immediately on humans. Many parameters, such as ring down time of the gradients, had to be readjusted to optimize them for work

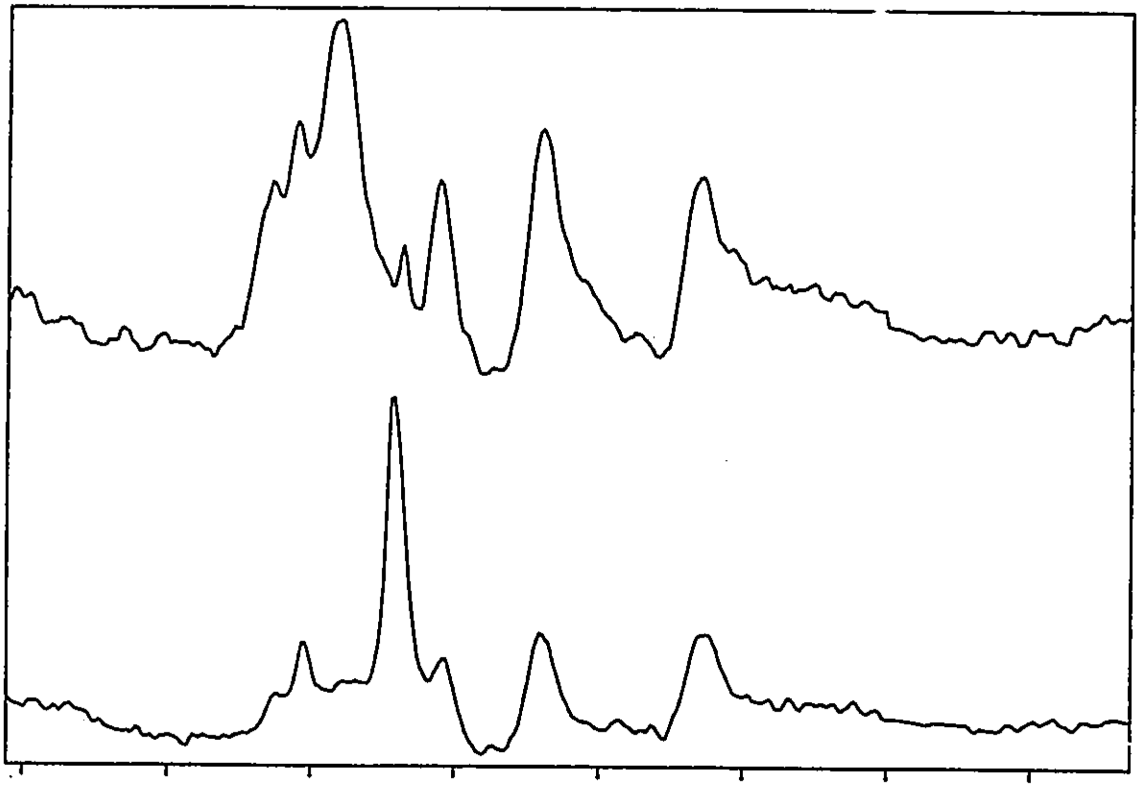

Figure 4.8: Two CSI spectra from a volunteer. The top spectrum is characteristic of liver and the bottom spectrum of muscle.

with human subjects. Once the experiments in this chapter had been completed, the method was attempted on brains of normal volunteers and experiments with tumour patients were started.

CHAPTER 5

1D CSI of Human Brain Tumours

^{31}P chemical shift imaging spectroscopy was successfully performed in vivo on twenty-eight patients with untreated brain tumours. The goal was to characterize the tumours according to their pathology. This noninvasive characterization could aid pathological diagnosis from biopsy samples and possibly ultimately eliminate the need for biopsies. Further, if in vivo ^{31}P NMR proves to be an early predictor of response to therapy, a baseline characterization of untreated brain tumours such as this study is required.

5.1 Materials and Methods

The Siemens Magnetom and the 9 cm surface coil are described in Chapter 4. The procedure, described below for patients with brain tumours, was established and followed without any significant changes thoughout the project. Only patients with large tumours, who could easily comply with the procedure, were recommended by the neurosurgeon for this study.

Before the arrival of the patient, the CT scans were obtained and the approximate size and location of the tumour were determined. If available, MRI scans were used for this purpose. If an MRI had not been performed on the patient previously, then, once the patient had arrived, the questions shown on the checklist in Appendix 4 were asked. These questions were used to verify that the procedure could be performed safely on the patient. A registered nurse was in attendance for all patients as an additional precaution.

The patient was positioned comfortably on the patient table. A small vial of 0.1 M PPA (phenylphosphonic acid) was placed on the side of the patient's head in the approximate location of the tumour. A nylon strap with Velcroed ends was used for this purpose. The strap, to which the vial was permanently taped, was wrapped around the patient's head, positioning the vial over the tumour. The patient was given earphones through which music and two way communication were provided. Once instructions had been given to the patient regarding noise levels and test length, the patient was moved into the magnet such that the tumour was at the isocentre of the magnet in the z direction. Magnetic resonance images, in three dimensions, were then taken of the area which would be covered by the CSI experiment, using the sequence SESMS

(Appendix 1).

The first set of images was taken in the z direction and consisted of eight images centred at the isocentre. The slice thickness was 7 mm and adjacent slices were separated by 5 mm. The slices therefore covered an area 9 cm thick, the approximate area from which signal would be received by the surface coil during the CSI measurement, in the z direction. The images were viewed using a grid to determine whether a 16 or 24 cm CSI measurement in the x direction would be appropriate. The reference and ultimately the coil was always placed on the side of the patient's head, often just above the ear and the CSI measurement was performed in the x direction (i.e. from ear to ear) for all patients. A typical image is shown in Figure 5.1. The grid, which is shown in Figure 4.6, would be overlaid on the image to indicate the isocentre and actual dimensions in centimeters. If the z images indicated that the patient's head or the reference vial was further than 8 cm from the isocentre in the x direction, the 24 cm CSI sequence was used, to ensure that no folding occurred. If the head and reference vial were within a field of view of 16 cm, centred at the isocentre, the 16 cm CSI sequence was used. Since the patient's head was approximately centred, a field of view of 24 cm, centred at the isocentre, was sufficient for all patients and volunteers.

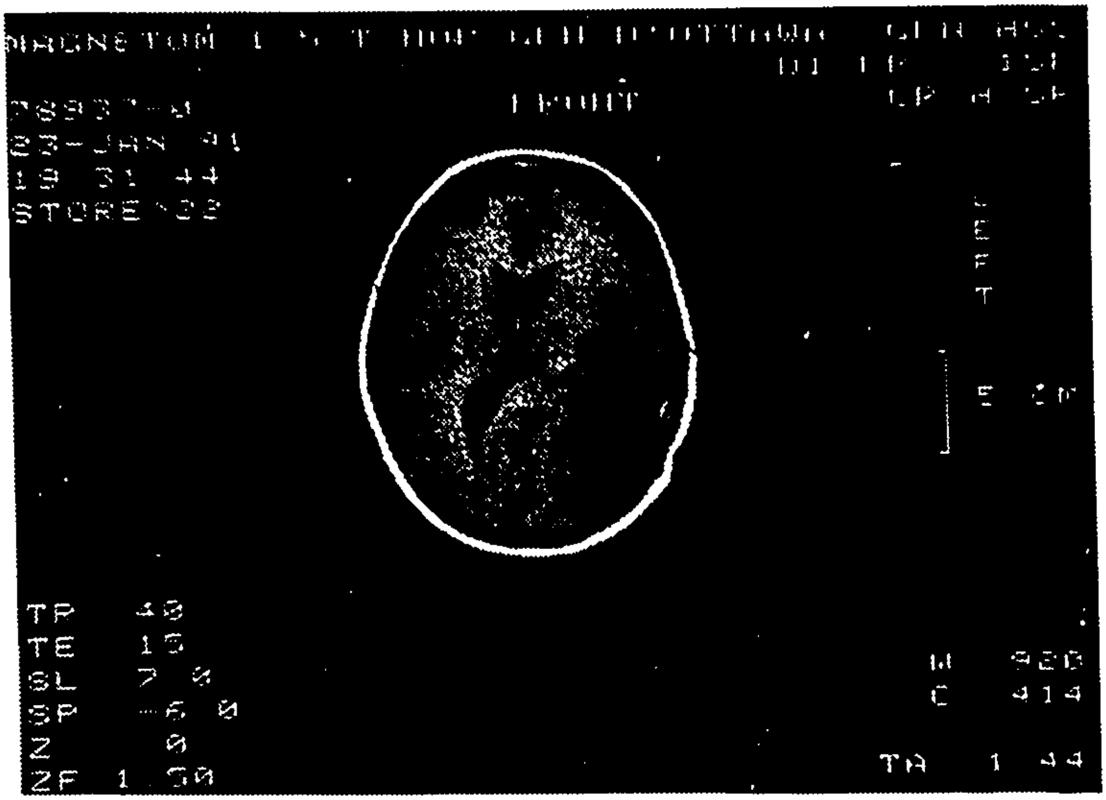

Figure 5.1: Typical image of a brain tumour used for localization. Note the location of the reference vial adjacent to the tumour.

The next set of images was taken in the x direction and consisted of ten images centred at the isocentre. The x direction was the direction of the chemical shift imaging measurement and therefore the spacing of the slices was determined once the CSI sequence was chosen. If the 16 cm CSI measurement had been determined to be appropriate, the 7 mm slices were separated by 1 cm; for a 24 cm sequence they were separated by 2 cm. This ensured that the entire area covered by the CSI experiment would be imaged. The final set of images was taken in the y direction and was set up as described for the z direction except that they were centred on the vial, not the isocentre. The surface coil was centred on the vial in the y direction and thus these images would cover the volume, in the y direction, from which signal would be received from the surface coil during the CSI experiment.

Once images had been taken in the three spatial dimensions, the patient was taken out of the magnet, but was cautioned not to move relative to the patient table. The 9 cm surface coil was positioned over the reference vial and snugly against the patient's head by taping it to the Velcroed strap. If the images had indicated that the vial/tumour alignment was correct, i.e. the vial was properly positioned adjacent to the tumour, the surface coil was centred on the reference vial in the z and y direction. If the alignment was incorrect then the surface coil was positioned adjacent to the tumour and its location relative to the vial was noted. The coil was always placed over the vial but the coil could be placed such that the vial was flush with the edge of the coil in the y or z direction as opposed to centred. The patient was asked not to move during the attachment of the coil. If, however, the patient did move, the reference vial was attached to his head, and, since signal from the vial is present in the images and the CSI spectra, the correlation between images and spectra could still be made. Once the coil was positioned properly the tuning of the surface coil and body coils was performed.

For patients in the early part of the study optimization of all shim coils was performed in order to obtain a homogeneous B_0. Once a good set of initial shim settings had been established, only x, y, z and z^2 shims were adjusted for each patient. An unlocalized, except by the surface coil, spectrum of 16 scans was taken and used to adjust the frequency to the left of the PME peak. The sequence CSI1DE16 or CSI1DE18 (Appendix 3) was loaded for a 24 cm or 16 cm CSI experiment respectively. With the self adjustment of frequency and transmitter turned off, the transmitter was manually adjusted to 40 V. This value of the transmitter produced a 90° pulse at a depth of approximately 3 cm with the 9 cm surface coil.

The CSI sequence was 16 steps and 1024 points in the chemical shift dimension. The dwell time was 255 μs and the sweep width was 4000 Hz. The phase encoding steps were in the x direction in all cases. Initially 128 scans were taken but this was switched to 64 scans as magnet homogeneity was improved through better shimming. With 64 scans the acquisition time was 17 minutes with a 1 s delay. The total procedure could be completed in one hour.

The two dimensional Fourier transform of the data was performed in FTNMR as outlined in Chapter 4. The MR images were filmed and saved on magnetic tape. The technique usually yielded 3 to 6 spectra for each patient, with each spectrum correlated to a specific disk shaped area or voxel on the image. A typical data set is shown in Figure 5.2. The voxels were 1.0 or 1.5 cm thick with an approximate diameter of 9 cm. The correlation between the images and the CSI spectra was checked with the reference vial. Table 5.1 shows how the data were tabulated. The rows with tumour, edge of tumour and "normal" tissue were designated where possible, as well as the row in which signal from the reference vial was present.

The spectra were processed with convolution difference to eliminate the broad hump in the PDE area. Convolution difference is widely used to eliminate the broad component of

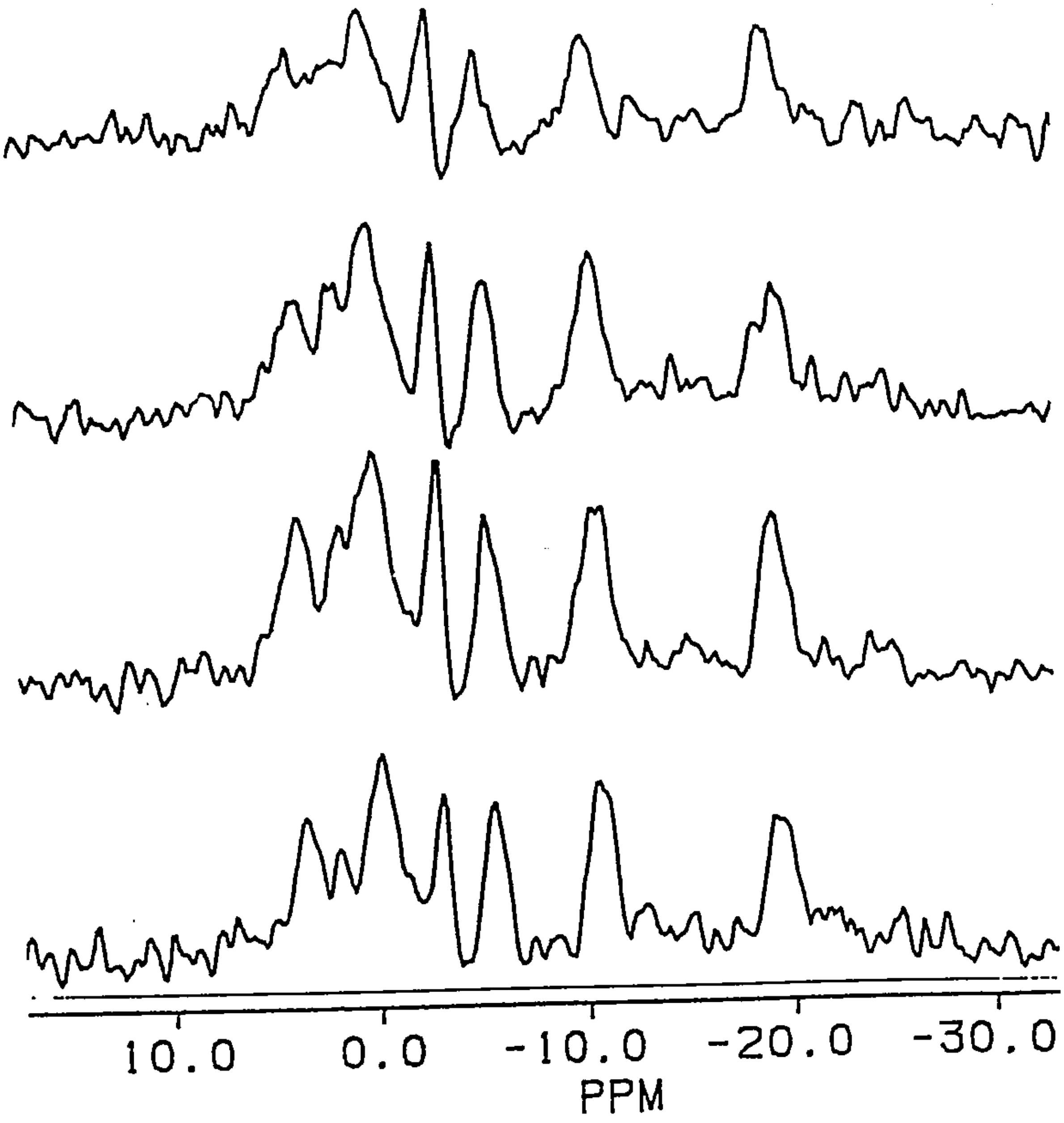

Figure 5.2: Typical set of CSI spectra taken from a normal volunteer.

FILE NAME:

Patient Name:

Patient #:

File #							
PME							
Pi							
PDE							
PCr							
γ- ATP							
α- ATP							
β- ATP							
Pi (ppm)							
pH							

CSI 16 24

No. of Scans:

Ref in Row:

Tumour in Rows:

Coil/Ref. Alignment:

Other:

Table 5.1: Data sheet used for 1D CSI experiments

the baseline evident in Figure 2.1. The free induction decay (FID) is multiplied by an exponentially decaying function (line broadened) with a decay constant comparable to the broad component or baseline (78). The resultant FID is weighted to a fraction and then subtracted from a copy of the FID which has been line broadened with a decay constant comparable to the linewidths of the high resolution lines. In the CSI spectra the very broad component in the baseline was eliminated because the sequence had an approximately 2 ms delay before acquisition. However, convolution difference was still used to eliminate to less broad hump which underlies PME, PDE and Pi in the spectra. For this thesis, each spectrum was line broadened to 40 Hz, multiplied by 0.9 and then the resulting spectrum was subtracted from the original spectrum which had been linebroadened to 10 Hz. An FTNMR program named CONDIF (Appendix 2) was written for this purpose. This procedure eliminated the hump and made it easier to obtain reproducible integrals. Other, more detrimental effects of convolution difference using these parameters would be a reduction of the contribution of the broad components of PDE to the spectrum. The procedure could also reduce the integrals of PME, PCr and Pi. However, all spectra were processed identically and thus these effects would be consistent on all spectra.

After convolution difference was performed, representative baseline points were entered and the baseline was corrected with a polynomial automatic baseline correction. If the signal to noise ratio was less than 3:1, the spectrum was not used. The pH was determined using the Pi chemical shift relative to PCr and the formula taken from Ng et al (28). The integrals which were taken for PME, Pi, PDE, PCr and the three ATP peaks are truncated, i.e. there was no curve fitting or triangulation of the peaks. The data taken from the spectra were transferred to LOTUS 123 software and various ratios and parameters were calculated. Areas relative to α-ATP, pH using the formula taken from reference 28, and areas as fractions of total P were calculated. The centre of the spectrum was always placed just downfield of the PME resonance. Because of this the intensity and phasing of the β-ATP peak was subject to off-resonance effects and thus could not be used in the ratios. The β-ATP peak would have been preferable to the α-ATP peak because it has no contribution from ADP. All future references to ratios of ATP in this thesis refer to ratios of α-ATP.

Quantitative concentrations are not obtained in this thesis. In order to compare tumour tissue to normal brain tissue some type of number is required. Integrals which have been normalized to ATP were chosen because they were believed to be more indicative of quantity than peak heights. The α-ATP peak includes contributions from ADP and other nucleotide triphosphates, and thus the ATP integral used does not reflect only the quantity of ATP. The removal of the hump underlying PDE diminishes the integrals in that area of the spectrum. As stated above, the processing of the spectra was identical in all cases. Changes, relative to α-ATP, in the quantities of PDE, PME, Pi and PCr will be reflected in their respective ratios.

5.2 Results and Discussion

Depending on the size of the tumour, spectra were obtained from voxels which were predominantly tumour and from voxels of normal tissue surrounding the tumour. Some tumours were very large and their position in the brain was such that only tumour spectra were obtained. Spectra of normal tissue adjacent to the tumour were often not obtained for tumour patients because of the size of the tumour. Because of this normal tissue in the brain of tumour patients could not be used as a control. Furthermore, using adjacent normal tissue as a control could be misleading because significant differences between normal brain tissue in volunteers and uninfiltrated brain tissue spectra from tumour patients have been noted by other groups (79). Occasionally the signal to noise of the acquired spectra was poor and only two spectra were obtained from the patient or normal volunteer. As discussed in Chapter 2, the CSI voxels will have some contamination from neighbouring voxels.

As discussed above, PDE/ATP, PME/ATP, PCr/ATP, Pi/ATP and pH were tabulated for each spectra. The spectra from each patient generally showed great heterogeneity. Figure 5.3 shows typical results for PDE/ATP from a patient with an astrocytoma. Note that the PDE/ATP reaches a maximum, not in the centre of the tumour, but just outside the centre. From each patient, or normal volunteer, two to five spectra were obtained. Thus, for every patient and normal volunteer a number of values of each parameter were obtained. In Figure 5.3 the four values of PDE/ATP obtained from an astrocytoma are plotted. The variability in the values represents the heterogeneity in the tumour tissue and in the surrounding "normal" tissue. Rather than average the values to obtain, for example, an average PDE/ATP value for a tumour; one value of PDE/ATP was chosen. The most obvious choice for this one value would be the value from the voxel positioned at the centre of the tumour. But, not only was this not available for some tumours, it was also often not the most abnormal value. It was decided, therefore, that the most abnormal, i.e. the highest value, would be chosen for each parameter regardless of voxel position.

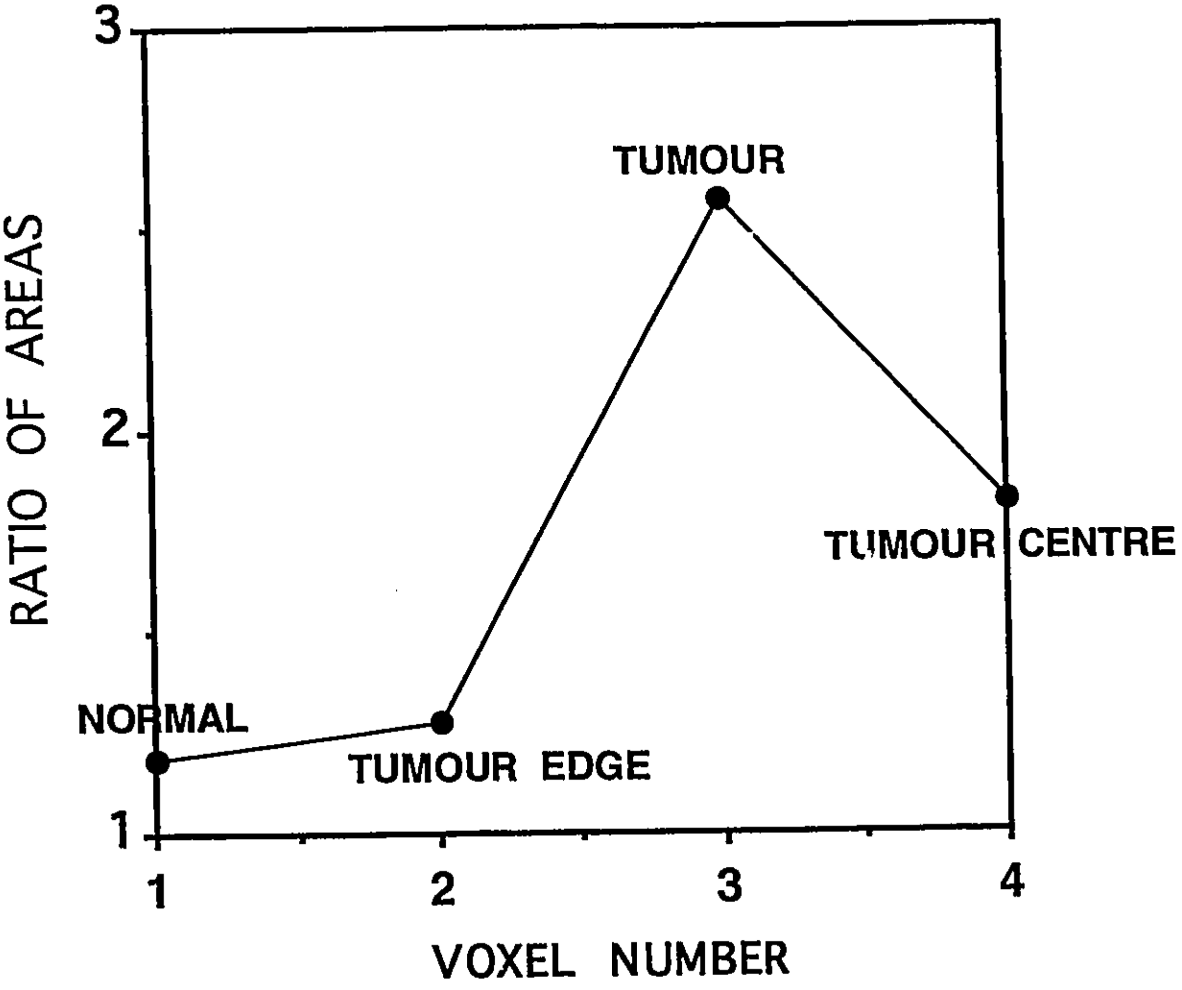

Figure 5.3: PDE/ATP values for an astrocytoma.

This highest value was assumed to be characteristic of the tumour for patients and of normal tissue for normal volunteers. The highest value for a parameter could be located (according to the definition of the tumour boundary in the image) outside the tumour, at the edge of the tumour or in the centre of the tumour. The highest values for all parameters were usually not in the same voxel. The highest value of Pi/ATP, for example, might be expected in the necrotic centre of a tumour. Conversely the highest value of PDE/ATP would be expected at the edge of the tumour where infiltration of normal tissue and the most rapid growth was occurring.

The highest values, selected as described above, will be used in all comparisons of tumours and normal brain in this chapter. While characterization of the tumours according to pathology is the main goal of this chapter, some biochemical interpretation will be attempted. Only limited biochemical inferences can be made because 1) one value of PDE/ATP, PME/ATP, PCr/ATP, Pi/ATP and pH was chosen to be representative of the tumour in each patient and of normal brain in each normal volunteer and 2) in the patients the ratios reflect quantities of PME, PDE, Pi and PCr in one area of a heterogeneous tumour.

The results will be discussed in terms of four types of tumour tissue, namely, astrocytomas, glioblastomas, meningiomas and metastases, relative to the normal brain tissue of volunteers. The CSI spectra from normal brains were obtained from nine volunteers with a mean age of 33, with the age ranging from 25 to 45. The results from these nine volunteers were used as normal values for all parameters. The values for PDE/ATP, PME/ATP, PCr/ATP, Pi/ATP and the pH are plotted in Figures 5.4, 5.5 and 5.6 for each group. Means and standard deviations were calculated, Table 5.2, and a two tailed t test was used to determine if there was a significant difference ($p < 0.05$) between tumour patients and normal volunteers for these parameters.

Astrocytomas

The eight subjects with astrocytomas were all male and ranged in age from 22 to 54 years old with a mean age of 33. Included in this group were two oligoastrocytomas and one pilocytic astrocytoma. Of the remaining five astrocytomas in the group, three were grade I-II and two were grade II-III. Two of these five tumours were recurrent. The results from the pilocytic astrocytoma were eliminated from the group because this tumour had been treated with radiation therapy before the CSI experiment was performed. The values obtained for PME and Pi for this tumour were significantly

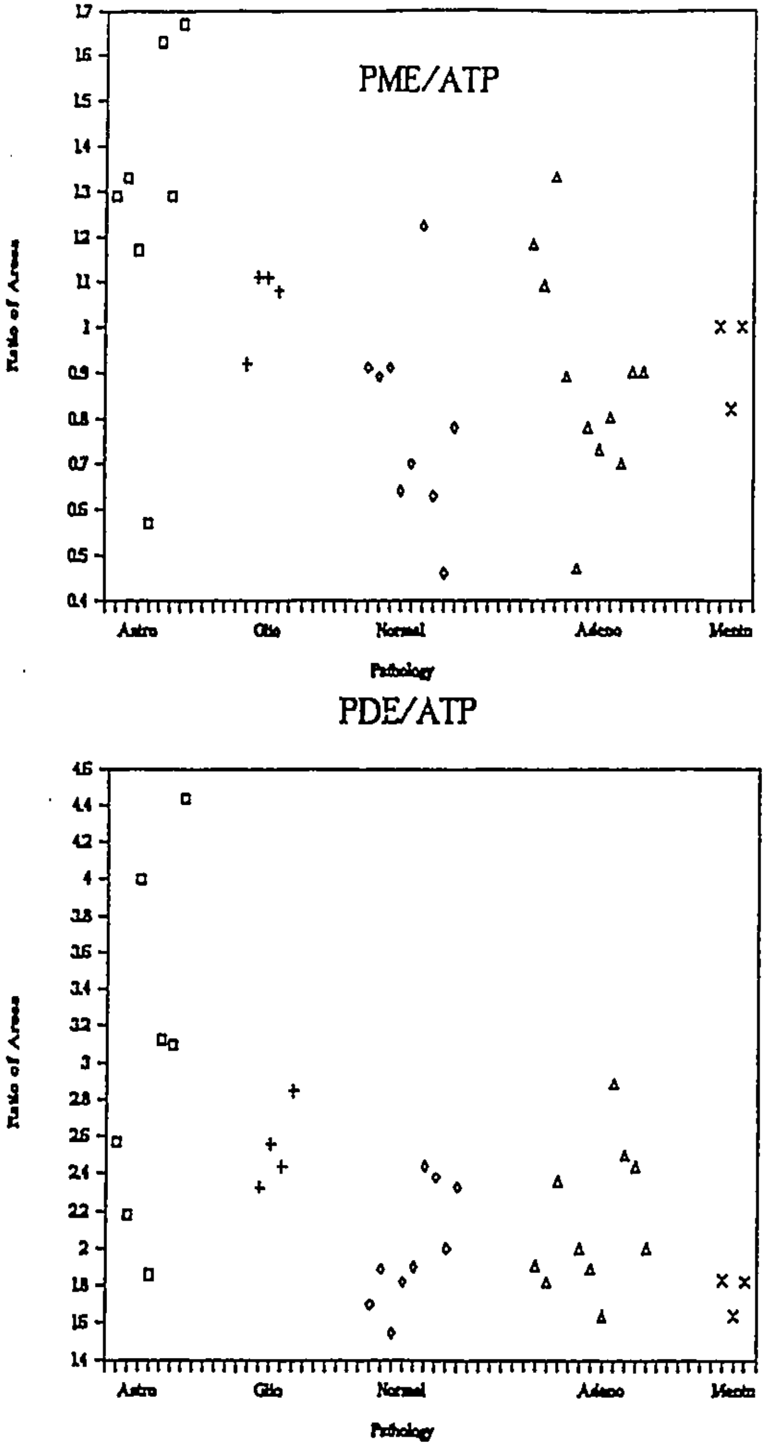

Figure 5.4: Plots of a) PME/ATP and b) PDE/ATP versus pathology.

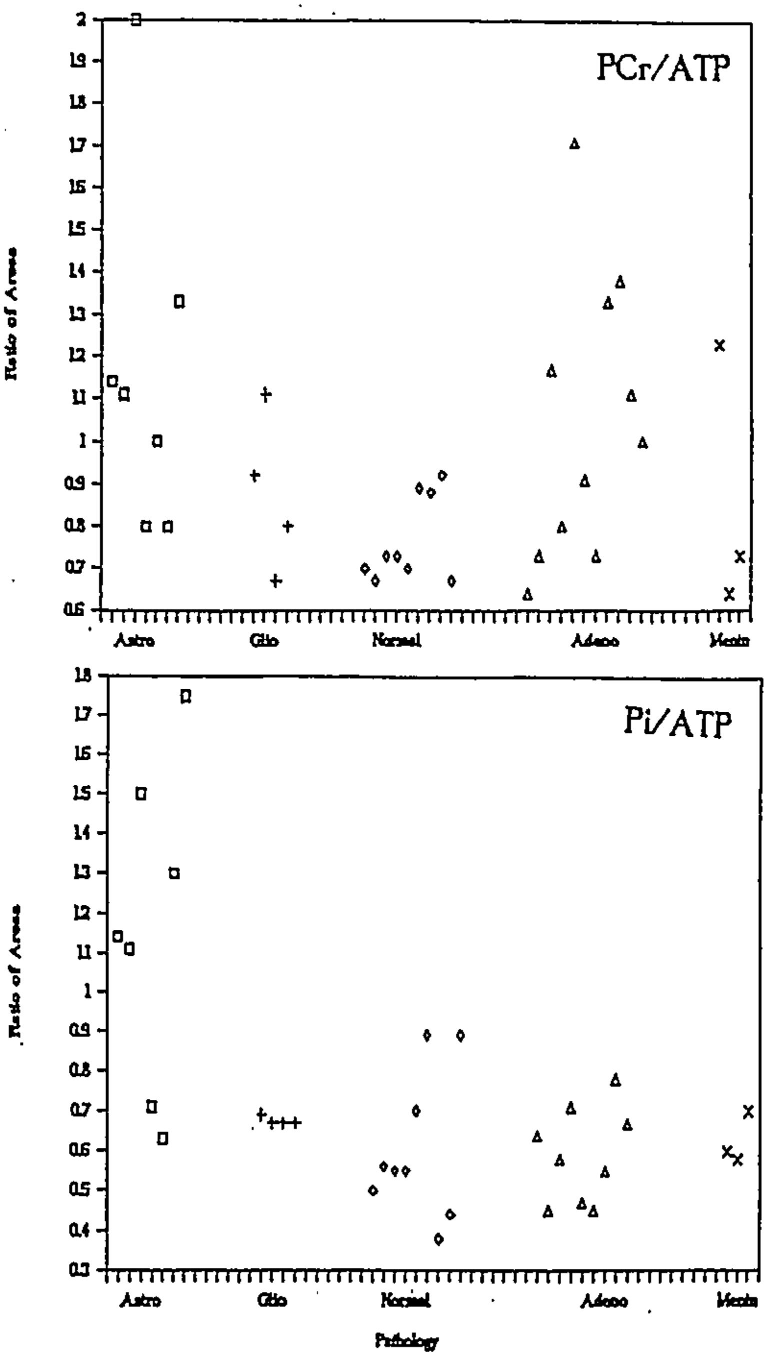

Figure 5.5: Plots of a) Pi/ATP and b) PCr/ATP versus pathology.

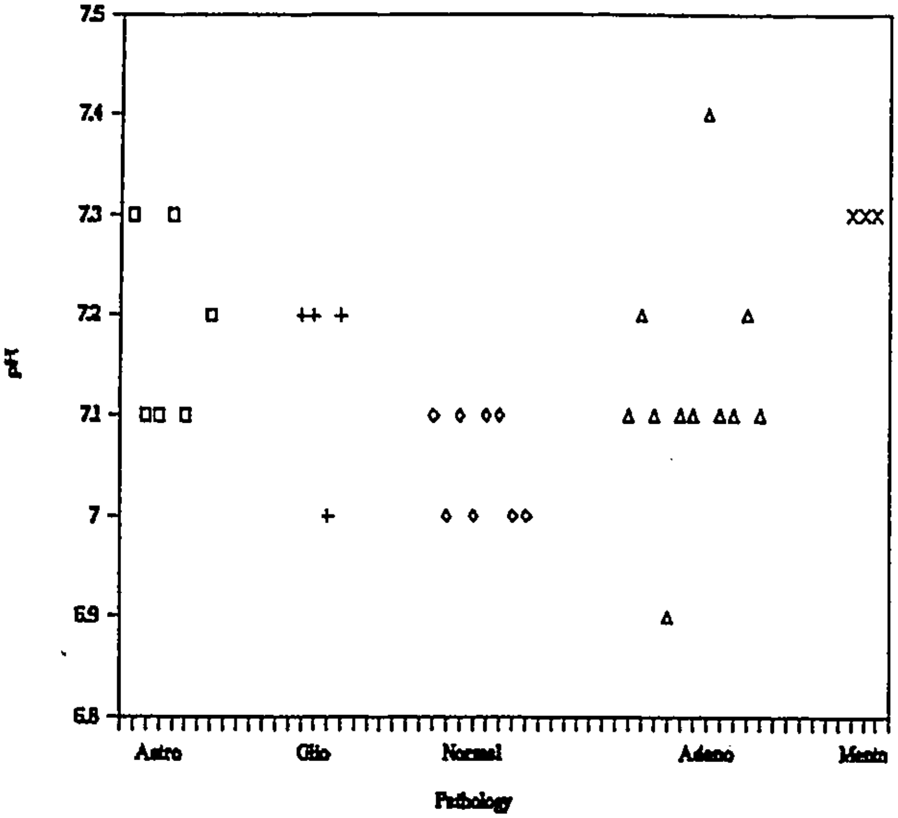

Figure 5.6: A plot of pH as calculated from the shift of inorganic phosphate versus pathology.

	Astro	Glio	Normal	Adeno	Menin
PME/ATP	1.28 (0.36)	1.06 (0.09)	0.79 (0.22)	0.90 (0.23)	0.94 (0.10)
PDE/ATP	3.04 (0.94)	2.55 (0.22)	2.00 (0.32)	2.57 (1.47)	1.76 (0.11)
PCr/ATP	1.17 (0.41)	0.88 (0.19)	0.77 (0.03)	1.05 (0.33)	0.89 (0.36)
Pi/ATP	1.16 (0.40)	0.68 (0.01)	0.61 (0.03)	0.59 (0.13)	0.63 (0.06)
pH	7.24 (0.18)	7.15 (0.10)	7.05 (0.05)	7.13 (0.12)	7.30 (0.00)

Table 5.2: Means and one standard deviation for the tumour groups for PDE/ATP, PME/ATP, Pi/ATP, pH and PCr/ATP.

lower than the rest of the group. A decrease in PME values in response to radiation and/or chemotherapy has been reported for some patients (38, 80, 81) but generally Pi increased after treatment. Unfortunately pretreatment values were unknown for this tumour.

Astrocytomas have values of PCr/ATP, Pi/ATP, PDE/ATP and PME/ATP which are generally higher than normal values. Despite some overlap with normals, evident in the plots (Figures 5.4 and 5.5), statistically significant difference can be shown ($p < 0.05$) for all four parameters. The means and standard deviations of the ratios are shown in Table 5.2. The pH of the astrocytomas ranged from normal to alkaline, Figure 5.5. Neither recurrence or grade could be correlated to any of the ratios nor the pH in this study.

The rise in the ratio of phosphocreatine to ATP is difficult to interprete biochemically. Elevation of the ratio may be caused by increases in the creatine concentration although Lowry et al (55) reported lower creatine concentrations in gliomas. Increased ATP was found in some astrocytomas in the same study. It is unknown whether the PCr/ATP in our study is raised by higher PCr or lower ATP levels, although the highest values for total ATP, as a percentage of total phosphorus, were not significantly different from normal values. An increase in PCr with a decrease in Pi, might indicate healthy, as opposed to necrotic, tumour tissue. In this study, however, high PCr/ATP and high Pi/ATP were characteristic of astrocytomas. PCr/Pi, a ratio sometimes postulated to discriminate between healthy and necrotic tissue, was not significantly different from normal brain. An elevation of the Pi/ATP ratio has been postulated to be caused by necrosis in the tumours, although an increase of Pi could not be correlated with a higher grade of tumour.

PME/ATP and PDE/ATP were significantly higher in astrocytomas. Because PME and PDE are intermediates in membrane metabolism, increases in PME/ATP and PDE/ATP may reflect increased membrane production required by rapidly growing tumours (33).

It is difficult to compare results from this study to the literature because 1) methods of localization can affect the ultimate spectral ratios which are recorded, 2) spectral processing varies from research group to another and ratios and/or areas are not always reported and, 3) most groups obtained one spectrum from the entire tumour and whereas this study used the most abnormal slice through or surrounding the tumour. Data from astrocytomas from five studies (1, 6, 79, 82, 83) which were performed between 1986 and 1991 using four different localization methods can be summarized as follows.

PME/ATP is generally but not consistently elevated. All five studies reported normal to alkaline pH for all astrocytomas. PCr/ATP is reported as decreased (79, 83), unchanged (6) and elevated (1). PDE/ATP was reported to be reduced or at normal levels in the astrocytomas. Our results are generally in agreement with the Cadoux-Hudson et al (5) who reported elevated PCr/ATP and PME/ATP using the B_1 gradient for localization. PDE was not elevated relative to normal volunteers, which is in conflict with our data, but given the large hump underlying PDE, it is the resonance most likely to be affected by processing and acquisition parameters.

Glioblastomas

The patient's age in this group ranged from 40 to 65 with a mean age of 51, and again all subjects were male. Two of the glioblastomas were recurrent tumours. As compared to the astrocytomas, each ratio calculated for the tumours in this group formed a tighter group (Figures 5.4 and 5.5). The pathology of the glioblastoma is very distinct, as opposed to the wide range of pathology indicated by grade I to grade III astrocytomas. The data indicate that the chemical environment, as seen by NMR, is also very consistent. The recurrent glioblastomas were indistinguishable from the first occurence glioblastomas.

Glioblastomas were characterized by significantly higher ratios of PME/ATP and PDE/ATP than normals, Table 5.2. As in the astrocytomas, pH ranged from normal to alkaline with a slightly higher percentage of the glioblastomas having alkaline pH. PCr/ATP and Pi/ATP were indistinguishable from normal values. By definition, the glioblastomas have significantly higher levels of necrosis than the low grade astrocytomas therefore the elevated Pi/ATP cannot be correlated with necrosis. The ratio may be affected by greater amounts of ATP (55) in the more aggressive tumours or may be reflecting the efficiency of elimination mechanisms for Pi in these aggressive tumours. Total ATP as a percentage of total phosphorus was not significantly different from normals. No differences in the ratio PCr/Pi in astrocytomas, glioblastomas, and normals can be shown, indicating the viability of the tissues as determined by this ratio is unchanged.

The elevated PDE and PME ratios may be caused by, as discussed above, the increased requirement for membrane synthesis.

The literature for glioblastomas is more limited than that for astrocytomas because glioblastomas are often included with astrocytomas under the general classification of glioma. In six studies in the literature (1, 6, 79, 82, 83, 84), PME and pH are generally reported to be elevated in glioblastomas, in agreement with this study, and PCr diminished relative to normal values. The only group reporting PDE/ATP reported statistically significant reductions in that parameter (6); however, that ratio was calculated using peak heights.

Meningiomas

Four patients with meningiomas were referred for spectroscopy. Of these only three patients were included in this study. Data could not be obtained from one patient because the signal intensity from the meningioma was too low. Metabolic concentrations have been reported to be low in a meningioma previously (85). The age range of the remaining two male and one female patients was from 24 to 62 years, with a mean age of 43. The 24 year old patient was a male with an agressive tentorial meningioma. The other two meningiomas were benign transitional. Despite the inclusion of both types of meningiomas, the values which were obtained from these tumours were very consistent for all parameters except PCr/ATP as can be seen in Figures 5.4 to 5.5. The tentorial meningioma was distinguishable from the benign tumours by an elevation of that ratio. The meningiomas were generally an easily recognized, distinct group, characterized by normal levels of PME/ATP and PDE/ATP and a consistently alkaline pH as shown in Table 5.2. All three tumours had a pH of 7.3. Normal values of PME and PDE have generally been associated with benign tumours (33) and this is supported by our data on meningiomas and gliomas.

As with the gliomas, the reports in the literature of _in vivo_ ^{31}P spectroscopy of meningiomas are few. In four studies (5, 6, 82, 83), which looked at twenty-three meningiomas, the pH is alkaline and PCr is low. Most of these studies analyze using peak heights, not areas. In the meningiomas reported in this thesis PCr/ATP is normal but, the areas are examined. If PCr is decreased it may be caused by the low total creatine in meningiomas (55, 58). Contrary to our results PME and PDE are reported to be elevated in some studies.

Metastases

Metastases to the brain are quite common, especially from the lung. The cases in this group totalled eleven and included eight adenocarcinoma from the lung, one squamous cell from lung, one metastases from the kidney and one adenocarcinoma from breast. The age range of the group was 37 to 72 years, with a mean age of 62. Seven males and four females were included in the group. The adenocarcinomas ranged from well differentiated to poorly differentiated. As is apparent in Figures 5.4 to 5.5, the calculated ratios for metastases overlapped with normals more than did the other tumours. Even if the adenocarcinomas from lung were taken as a group the scatter of the data was not reduced. The metastases could generally be distinguished by at least one parameter being higher or lower than values obtained for normal volunteers. PCr/ATP was found to be significantly different than normal values, but the overlap with normals was extensive. The variation could not be correlated to either the degree of differentiation or the type of tumour. Patients with adenocarcinoma from lung were divided into groups according to whether the metastases were diffuse or limited to brain metastases, but this did not delineate the scatter.

No accounts of ^{31}P in vivo spectroscopy of adenocarcinoma metastases to the brain could be found in the literature. There have been studies of primary squamous cell carcinoma (39, 83), and small cell metastases from lung (86) which report elevated PME. ^{31}P in vivo spectroscopy of primary breast adenocarcinoma has been reported in vivo (83) and in vitro (87). The one patient reported in vivo had elevated PME/ATP and Pi/ATP. The in vitro report characterized the phospholipids from benign and malignant breast cancer. Phosphatidylethanolamine was found to be significantly elevated in malignant tissue. Results from the one metastatic tumour from breast were in agreement with the in vitro study, having slightly elevated PDE/ATP, but in disagreement with the in vivo study, having normal levels of PME/ATP. In general, the metastases, as seen by ^{31}P NMR, are a widely diverse group, and while most tumours differ from normal brain tissue, no unique spectral characteristics can be found.

Miscellaneous pathology

Three other patients submitted to the CSI procedure, with pathologies which did not fit into the four groups above. The first case was a 27 year old woman with an abscess. The calculated ratios were all slightly elevated. The Pi peak was very broad and indicative of a number of compartments with differing pH. Total ATP was much higher than that determined for any tumours or normal brain reported in this thesis.

The second patient was a 68 year old woman with a lymphoma, and again all ratios were slightly elevated with respect to those of normal brain. A lymphoma included in an in vivo study (79) had decreased levels of PDE, PME, PCr and increased levels of ATP and Pi relative to total P.

The last tumour in this study was a pituitary tumour in a 46 year old male. PDE/ATP, PCr/ATP and Pi/ATP were elevated and the pH was alkaline. The pH measurement is in agreement with the results from a pituitary tumour in another study (6). This study measured peak intensities and found elevated PME and low levels of PDE, PCr and Pi, contrary to our results.

5.3 Conclusions

The primary brain tumours were found to have characteristic spectra using the CSI technique. Table 5.3 lists all parameters which were significantly different from normal brain. Astrocytomas had elevated PCr/ATP, Pi/ATP, PME/ATP and PDE/ATP. Glioblastomas had slightly elevated PME/ATP and PDE/ATP. The meningiomas were easily recognized by normal values of PME/ATP and PDE/ATP in combination with alkaline pH. The metastases, in contrast do not have characteristic spectra, but can generally be distinguished from normals by at least one parameter being lower or higher than normal values.

Consistent with other studies of human brain tumours, the pH of all tumours ranged from neutral to alkaline. This is contrary to the long held belief, which had been proven in animal models, that the intracellular pH of tumours would be acidic because of the lactic acid produced by anaerobic glycolysis. The lack of acidosis could be caused by the much

Pathology	Characteristics
glioblastoma	↑ PME/ATP ↑ PDE/ATP
astrocytoma	↑ PCr/ATP ↑ Pi/ATP ↑ PME/ATP ↑ PDE/ATP
meningioma	alkaline pH
adenocarcinoma	↑ PCr/ATP

Table 5.3: Characteristic parameters for primary brain tumours.

smaller size relative to host size, of the tumours, or by different vascularization in the human tumours (28).

The expected increase in PCr/Pi in large tumours predicted by animal models was not demonstrated, possibly also due to the smaller size relative to host size or differences in vascularization. While elevation of Pi/ATP occurred in astrocytomas, it cannot be correlated with necrosis in the gliomas in this study, because glioblastomas had normal values of Pi/ATP. The phosphocreatine to ATP ratio was elevated for the astrocytomas and the aggressive tentorial meningioma. PDE and PME ratios to ATP were high in almost all aggressive tumours indicating that elevation of these parameters may be caused by increase membrane turnover.

Attempts to compare data from this study to those of other studies were difficult because different data processing and localization techniques were used. Values for pH, which were less likely to be affected by these procedures, were in agreement with the literature. Because CSI was used, spectra were obtained from many voxels within and surrounding each tumour. The most abnormal value of a parameter was taken wherever it was located with respect to the tumour. This has allowed us to obtain characteristic spectral parameters for glioblastomas, astrocytomas and meningiomas. This information should be extremely valuable in the planning of surgery and therapy and will hopefully be a step towards eliminating invasive biopsies.

Chapter 6

Application of a Three Dimensional Localization Sequence

Once the one dimensional chemical shift imaging sequence was being used routinely with patients, the development of a three dimensional localization sequence was begun. A two dimensional chemical shift imaging experiment in combination with a slice selective pulse was determined to be the sequence of choice. This would allow spectra to be obtained within and surrounding the tumour but the spectral acquisition time would be shorter than for a full three dimensional CSI experiment. The development of the sequence and its application to phantoms and human volunteers will be discussed in this chapter.

6.1 Materials and Methods

The Siemens Magnetom and software was described in Chapter 4. The phosphorus head coil was designed and built by Paul Morris Instruments Ltd and the coil type is solenoid.

A picture of the head coil is shown in Figure 6.1. The phosphorus head coil was designed such that positioning of a person in the coil was identical to that of a person in the Magnetom proton head coil. The functioning of the phosphorus head coil, with respect to the imager, was the same as the surface coil. Usage of the head coil differed only in that once average tuning settings were obtained for a human head, the tuning was not readjusted. Tuning values of the head coil were strongly affected by the static magnetic field and thus the coil had to be adjusted inside the magnet. All other adjustment procedures were identical to those described in Chapter 4. Phantoms of PPA, DMMP, Na_3PO_4, and H_3PO_4 were prepared as described in Chapter 4.

6.2 Results and Discussion

Phantoms

The initial step in producing the three dimensional sequence was the expansion of the 1D CSI sequence into a two dimensional CSI sequence. This was accomplished by the addition of a second phase encoding gradient in an orthogonal dimension. For each phase encoding step the second phase encoding gradient must be stepped through. The factors governing the 2D CSI are identical to those for 1D CSI outlined in Chapter 4. In this case the sequence was

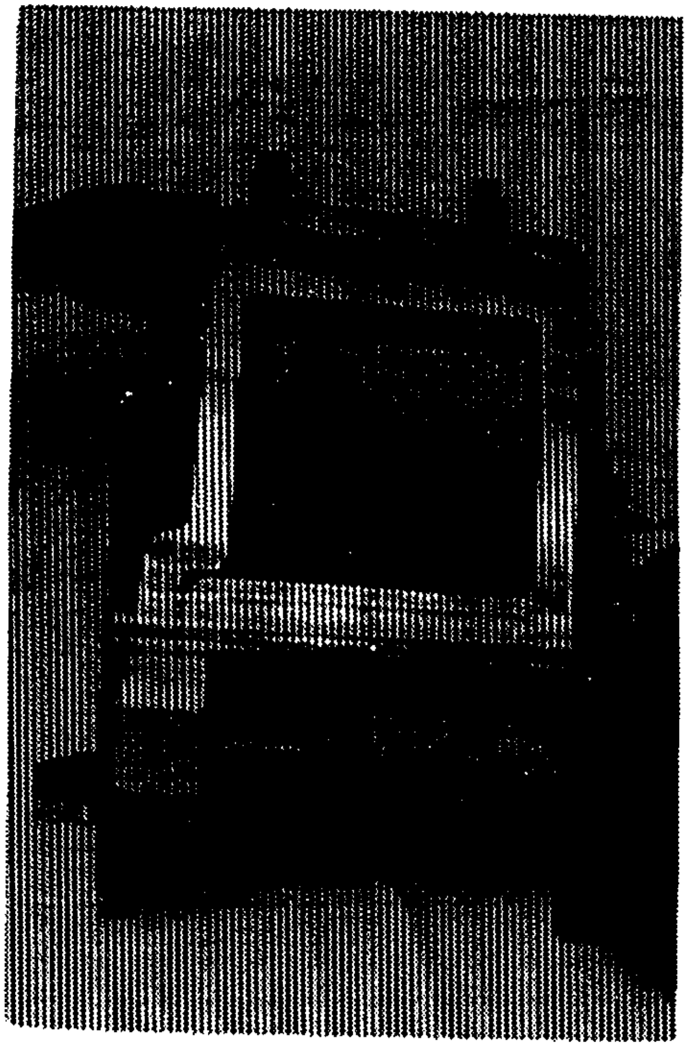

Figure 6.1: Phosphorus head coil designed and built by Paul Morris Instruments Ltd.

verified using a phantom comprised of 4 vials taped together. Each vial contained a different phosphate compound and thus had a unique NMR signal. This phantom is schematically shown in Figure 6.2 along with its phosphorus spectrum taken with the 9 cm surface coil.

A 2D CSI sequence was performed with gradients set such that the field of view was 24 cm by 24 cm. Eight phase encoding steps were used in each CSI dimension, resulting in voxels of 4 cm by 4 cm. The third dimension was limited by the B_1 field of the coil. The 9 cm surface coil was placed flat in the x-z plane underneath the phantoms. Figure 6.3 shows the results of the 2D CSI experiment. Each spectrum represents a voxel 4 cm by 4 cm in the x-z plane.

Processing the raw data from the 2D CSI experiment was accomplished by writing three new algorithms in FTNMR. The data set was 8 X 8 X 512 with the 512 points in the spectral dimension. The raw data set was in the form of 8 serial data files. Initially each serial file was processed individually by loading it into a matrix file and performing a 2D FT using algorithms AR2 and AR11. The third FT must be performed across the rows of the matrices and FTNMR macros AR3D1, AR3D2 and AR3D3 were written for that function. All five macros are reproduced in Appendix 2.

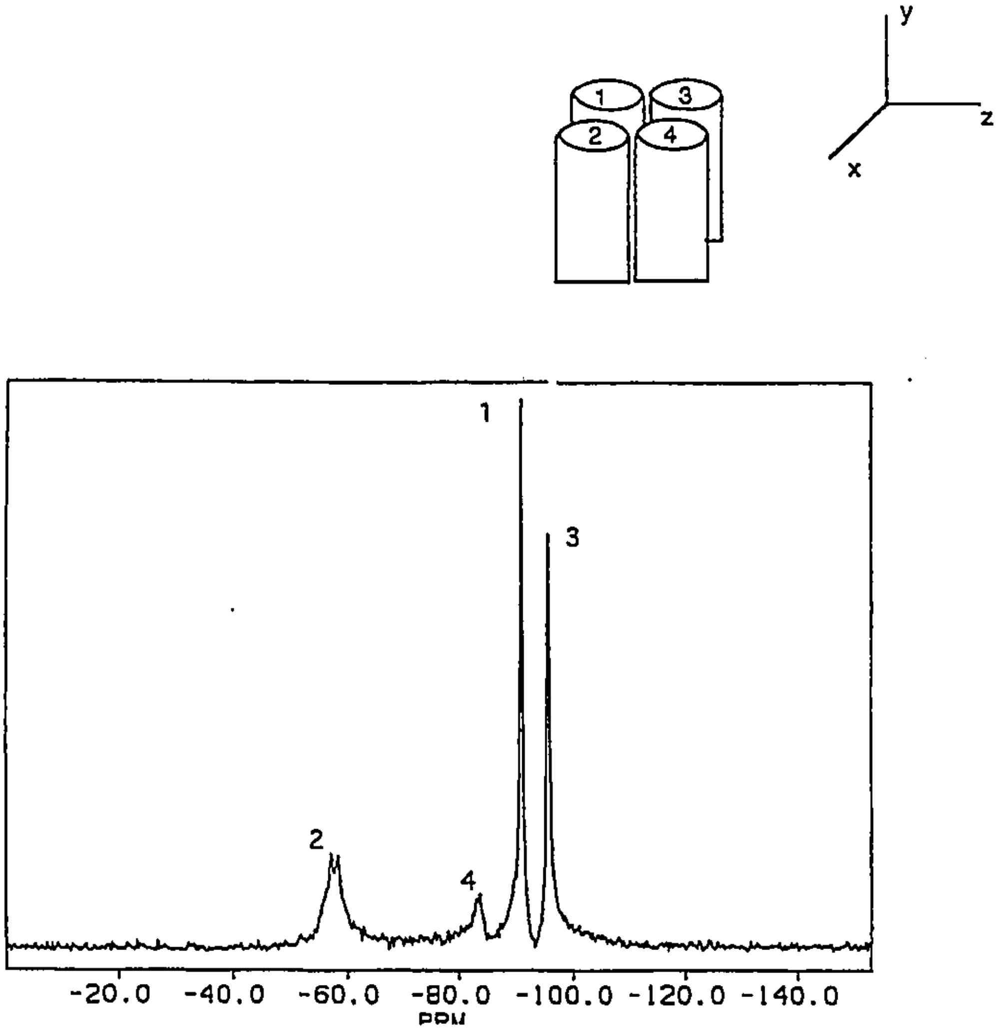

Figure 6.2: Phantom set up for testing 2D CSI sequence and the unlocalized phosphorus nmr spectrum of the phantom. The numbers indicate the position in the spectrum and the placement in the phantom of 1) Na_3PO_4, 2) DMMP, 3) H_3PO_4, and 4) PPA.

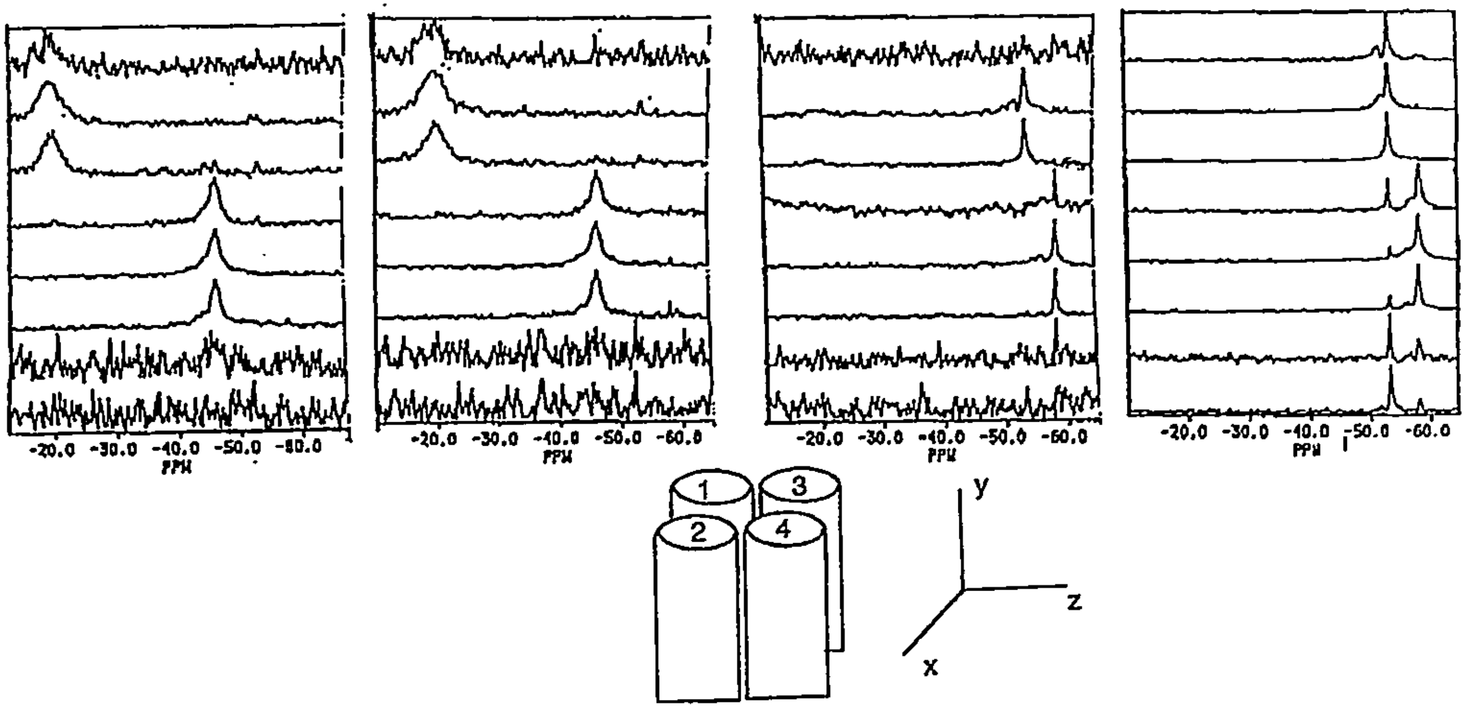

Figure 6.3: Results of the 2D CSI sequence on the phantom shown. The numbers indicate the position in the spectrum and the placement in the phantom of 1) Na_3PO_4, 2) DMMP, 3) H_3PO_4, and 4) PPA (see Figure 6.2 for chemical shift position). The axis refers to the phantom positioning in the magnet. Across the columns of spectra is the x spatial direction and down the rows is the z direction.

The full 3D localization sequence required the addition of a slice selection gradient. Before adding the slice selection to the 2D CSI sequence, a simple slice selection sequence was used with the head coil. The selective pulse used was a sinc pulse with a bandwidth of 340 Hz when applied for a duration of 5120 μs. Bandwidth is inversely related to the duration of the pulse and thus when the same pulse was used in the simple slice selection sequence CSI3DE19.UCR (Appendix 3) with a duration of 640 μs, the bandwidth was 2720 Hz. The calculated slice thickness was verified using various gradient strengths and phantoms. Slices which were centred where no phantom was present were used to check the quality of the slice. Trimming, or adjustment of the refocussing gradient pulse was performed when the slice thickness was changed. Figure 6.4 shows the performance of the slice selection pulse as compared to a pulse of shorter duration, a so-called "hard" pulse. The signal to noise obtained with this pulse was never as good as with hard pulses. In Figure 6.4 some of the signal to noise loss was caused by T_2 effects.

The complete 3D localization sequence, CSI3DE24.UCR (Appendix 3) which was used with volunteers is shown schematically in Figure 6.5. When this sequence was used with phantoms, voxels were of 3 cm by 3 cm in the two CSI dimensions and were limited in the third dimension by the

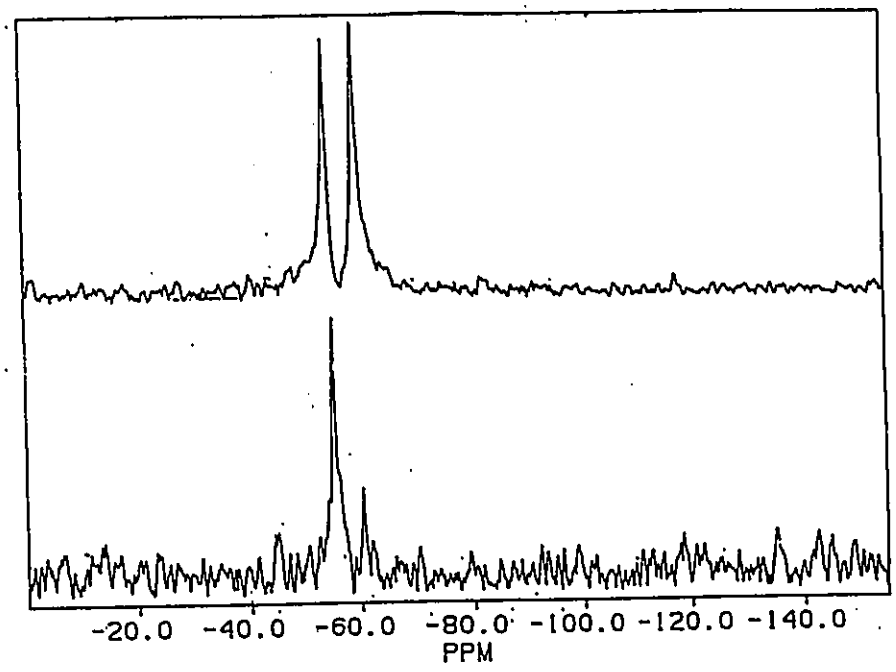

Figure 6.4: Performance of the slice selective pulse (bottom) as compared to a hard pulse (top). The hard pulse spectrum was obtained in 1 scan and the slice selective pulse spectrum was obtained in 16 scans.

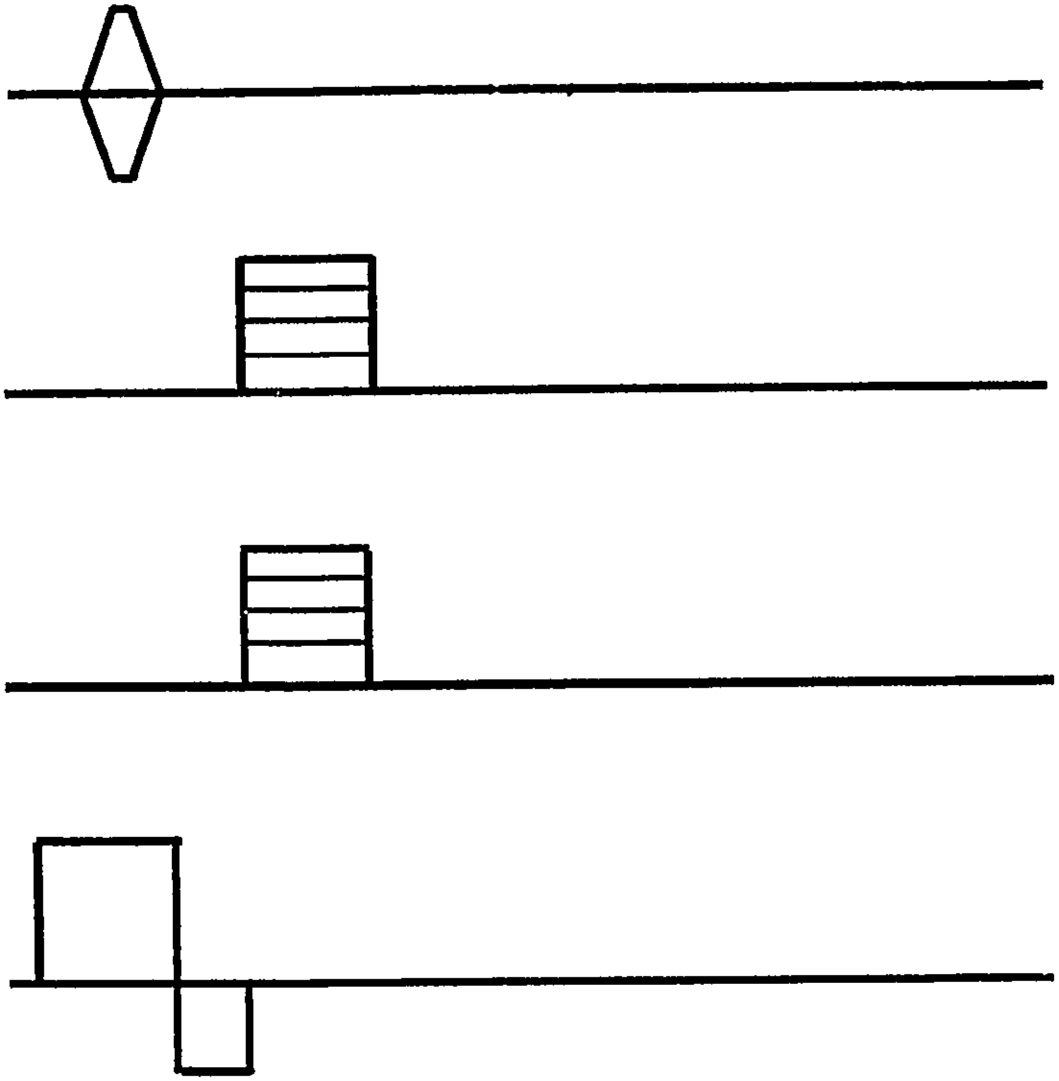

Figure 6.5: 3D localization sequence.

thickness of the slice, as defined by the slice select gradient (usually 3 or 4 cm). The sequence was verified on phantoms and then the gradients and dimensions of the CSI experiment were changed to suit the dimensions of the human head.

Human Volunteers

To obtain a reasonable signal-to-noise ratio it was necessary to increase the size of the voxels to 5 cm by 4 cm by 4 cm. The slice select gradient was adjusted to obtain a slice 5 cm thick. The CSI dimension covered an area 32 cm by 32 cm and 8 phase encoding steps were used in both directions. As in the 1D CSI of patients, images were taken of the volunteers in three dimensions before spectroscopy. In this case the Siemens proton head coil was used to take the images and given the identical positioning of the subject in the proton and phosphorus head coils, the images and the localized spectra could be correlated. Throughout the procedure a reference vial was attached to the volunteer's forehead to ensure that the correlation could be made.

Once the images had been taken, the volunteer was put into the phosphorus head coil, body coils were tuned automatically and shimming was performed. An unlocalized spectrum was obtained and used to set the frequency between γ-ATP and α-ATP. The slice selection only sequence CSI3DE19.UCR was then loaded and used to adjust the transmitter power. The transmitter power was found to change significantly from volunteer to volunteer. The 3D sequence, CSI3DE24.UCR was then loaded. The number of scans obtained was 32 and the spectral acquisition time was 34 minutes with a delay time of 1 s.

The results from one volunteer are shown in Figures 6.6 and 6.7. The image in Figure 6.6 is covered by a grid which indicates the voxels from which spectra were obtained. The spectra are shown in Figure 6.7.

6.3. Conclusion

The three dimensional sequence was successfully written and performed on phantoms and humans. The developmental work was performed so that the 3D sequence could be used on brain tumour patients. By the time the sequence was working on volunteers, spectroscopy had been performed on a number of patients using the 1D CSI sequence. Because of the lower signal to noise obtained in the 3D sequence and the ability to obtain multiple spectra of the tumour using the 1D CSI sequence, it was decided that the 3D CSI sequence would not be used on patients for this project.

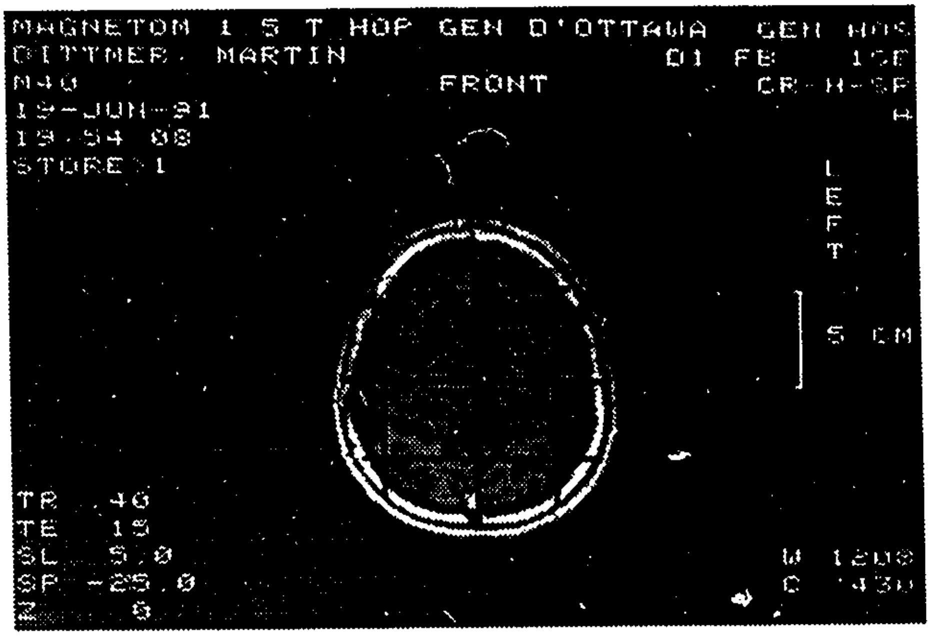

Figure 6.6: Image of a volunteer overlaid with a grid indicating the position of the CSI voxels.

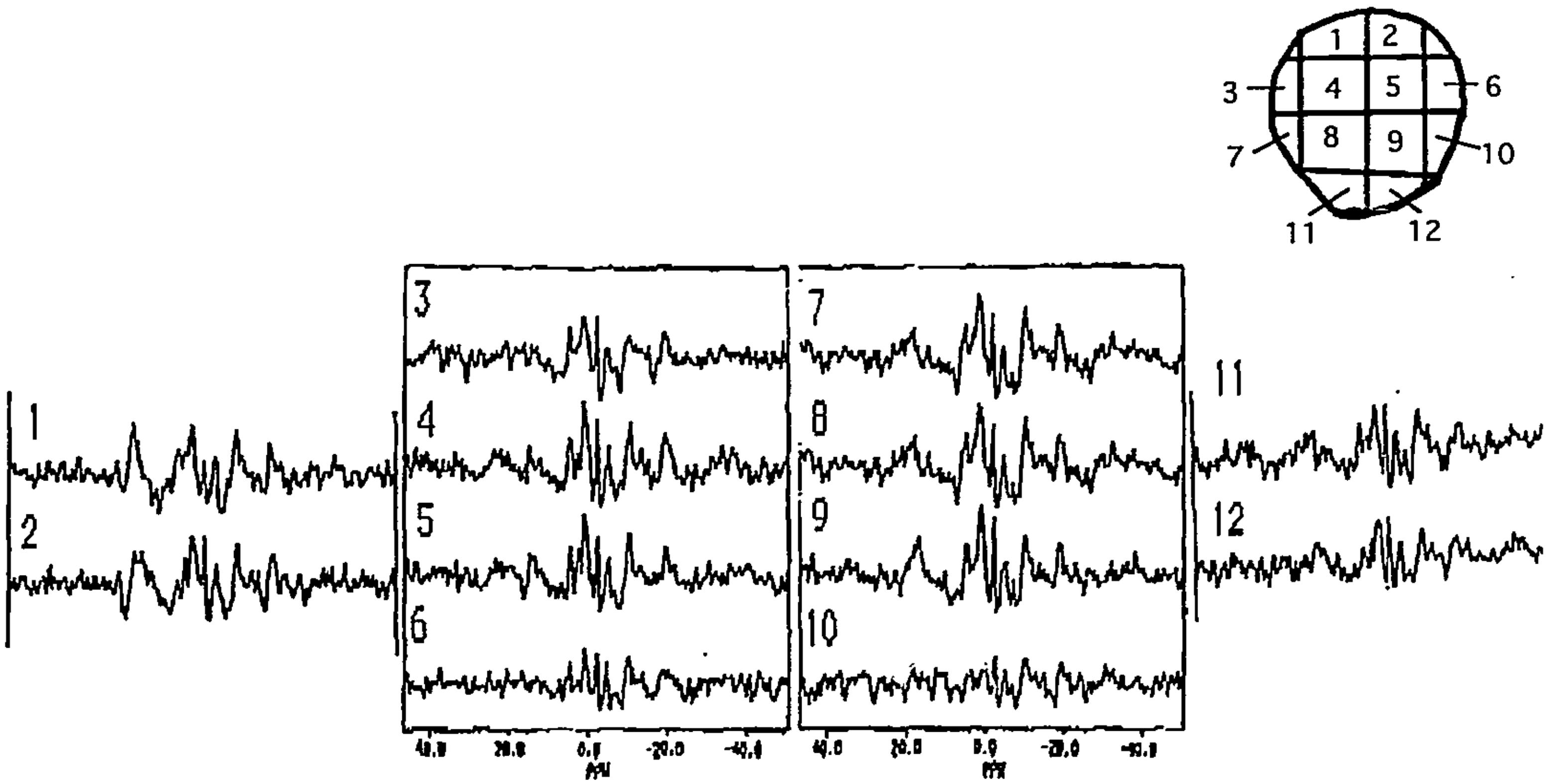

Figure 6.7: Results from the 3D sequence. Spectra are from the voxels indicated in Figure 6.5 and the numbering indicates the corresponding voxels. The peaks from the reference of PPA which was placed on the forehead of the volunteer is in spectra 1 and 2.

There are, however, a number of advantages to be gained by using the 3D sequence. The 3D sequence allows spectra to be obtained from both hemispheres of the brain at one session and thus the obvious control is obtained. With improved coil design it may be possible to achieve improved resolution. This 3D sequence with voxels small enough to accomodate multiple voxels in and around a tumour would yield the most information.

CHAPTER 7

Ex vivo ^{1}H NMR Spectroscopy of Brain Tumour Biopsies

Proton spectroscopy of human brain tumours was performed ex vivo and the one dimensional spectrum, the two dimensional COSY spectrum and T_2 data were obtained from each specimen. Once the pathological diagnosis was available, the spectroscopic data were compared to the diagnosis. As discussed in Chapter 3, ^{1}H spectroscopy has the potential to characterize brain tumours (56, 58), to further our understanding of the metabolism of these tumours (63), and to yield information regarding the degree of malignancy (72, 73). The research described in this chapter is concerned with the characterization of brain tumours and with the degree of malignancy of the tumour as expressed in the proton NMR spectrum.

7.1. Materials and Methods

Sample Preparation

During the scheduled craniotomy or stereotaxic biopsy, samples of the brain tumours were placed in Dulbecco's phosphate-buffered saline in D_2O (PBS-D_2O) within 15 s of surgical biopsy and immediately immersed in liquid nitrogen. When possible separate samples of normal brain tissue were also obtained from the patient. The samples were stored in liquid nitrogen or in a -70° C freezer until the spectroscopy was performed.

Before spectroscopy, the tissue was allowed to thaw. Sample volume ranged from 30 μL to 500 μL. Once thawed, the sample was inserted in a capillary using the method described by Kuesel _et_ _al_ (88). The capillaries used were for Micro/pettor, model I, o.d. 2 mm, i.d. 1.8 mm, length 9.5 cm, Scientific Manufacturing Industries. If the tissue was greater than approximately 50 μL, one or two small pieces, were cut from the sample, to facilitate insertion into the capillary. If there was any remaining portion of the sample it was refrozen. Using capillary action approximately 2 cm of the capillary was filled with PBS-D_2O. The sample was then introduced into the buffer-containing end of the capillary using tweezers. If the first sample was small and sufficient tissue was available another small piece of the tissue was inserted . A syringe needle (25 G 5/8) filled with buffer was used to move the sample approximately 7 mm from the end of the capillary and to ensure no air bubbles were introduced into the sample. The capillary was sealed with a teflon plug (Teflon plunger tips for Micro/pettor, Scientific Manufacturing Industries). The sample was checked for air bubbles and the capillary was put into a 5 mm NMR tube already filled with 300 μL of phosphate buffer saline in D_2O with anisic acid (0.05 mM) as a reference. The final positioning is shown in Figure 7.1. The placing of the sample in a capillary in this manner ensured the sample was correctly and stably positioned in the rf coils of the magnet.

Spectroscopy

360 MHz ^1H NMR spectra were taken using a Bruker wide bore spectrometer equipped with a 5 mm selective probehead. The temperature was stabilized at 37°C. The sample was locked to the resonance of D_2O and tuned. Most samples were shimmed to approximately 1 Hz half width at half height and 8 Hz at 10% of full height. The width at 10% was found to be a better indicator of the quality of the water suppression. A presaturation sequence, using simple irradiation at the water frequency to suppress the water signal was used to determine the 180° pulse. The pulse sequence ARCPCOP.AU (reproduced in Appendix 5) which acquired a 1D spectrum, performed a T_2 experiment, a COSY experiment and finally acquired 1D spectra until the sequence was terminated, was used for all samples.

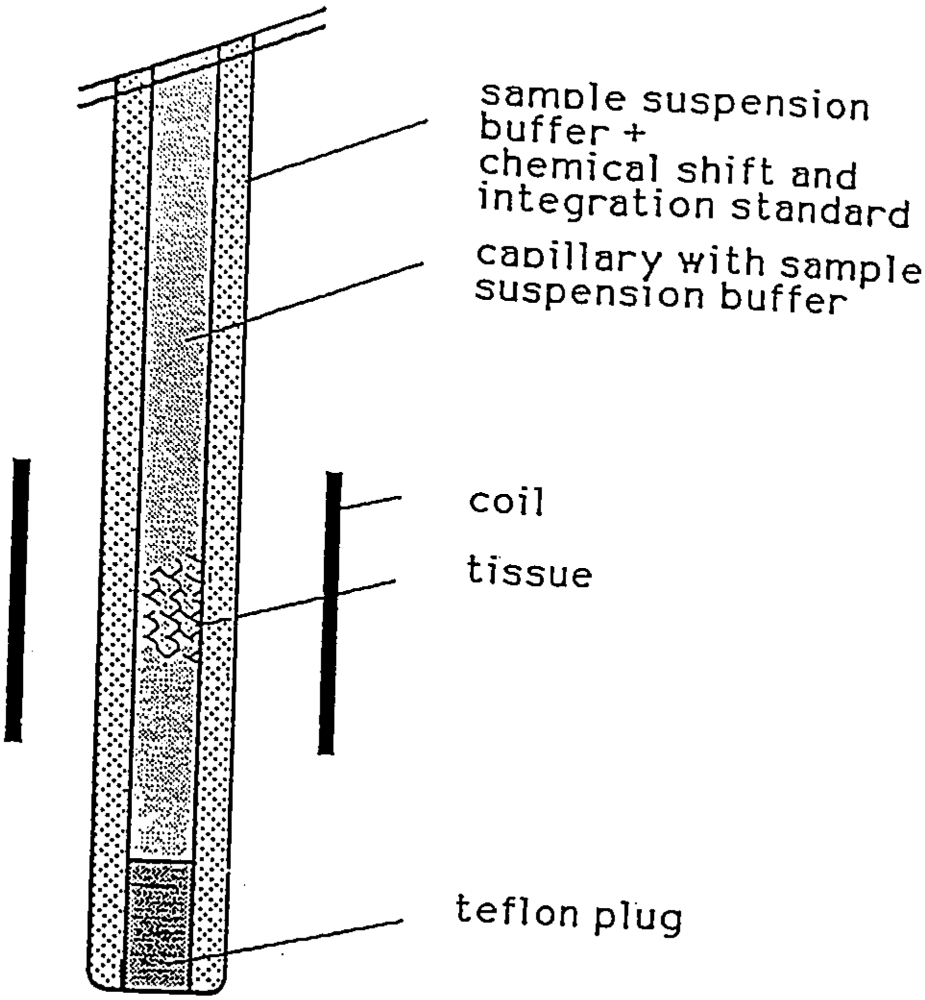

Figure 7.1: Positioning of the sample in the capillary and nmr tube.

Acquisition parameters for the 1D spectra were as follows: acquisition time 0.8 s; total recycle time 2.8 s, sweep width 2428 Hz; 4K data points; and number of scans 640. The 90° pulse for the 1D sequence was usually between 7 and 8 μs. The T_2 experiment was performed with the same parameters as the 1D spectra but only 64 scans were collected. The CPMG pulse sequence, described in Chapter 3, was used with a 1 ms delay between the 90° pulse and the 180° pulse. The number of n values was 28 with tau values ranging up to 1024 ms. The COSY experiment was 2K by 160 data points with a 1 s relaxation delay and 120 scans were collected.

Data Processing

All data processing was performed using Bruker software DISR86 or DISR89. The 1D spectra were line broadened to 1 Hz. The methoxy peak of the anisic acid was used as a reference, with a chemical shift of 3.887 ppm. Baseline correction was done using an eight point spline. The positioning of the eight points was approximately the same for each spectrum. Integrals were recorded for the areas between the following chemical shifts: 4.4 to 4.1, 4.1 to 3.4, 3.4 to 3.1, 3.1 to 2.9, 2.9 to 2.5, 2.5 to 2.2, 2.2 to 1.8, 1.8 to 1.5, 1.5 to 1.1, and 1.1 to 0.5 ppm. These areas of integration were chosen after many spectra had been processed. Although the spectra were quite diverse, most

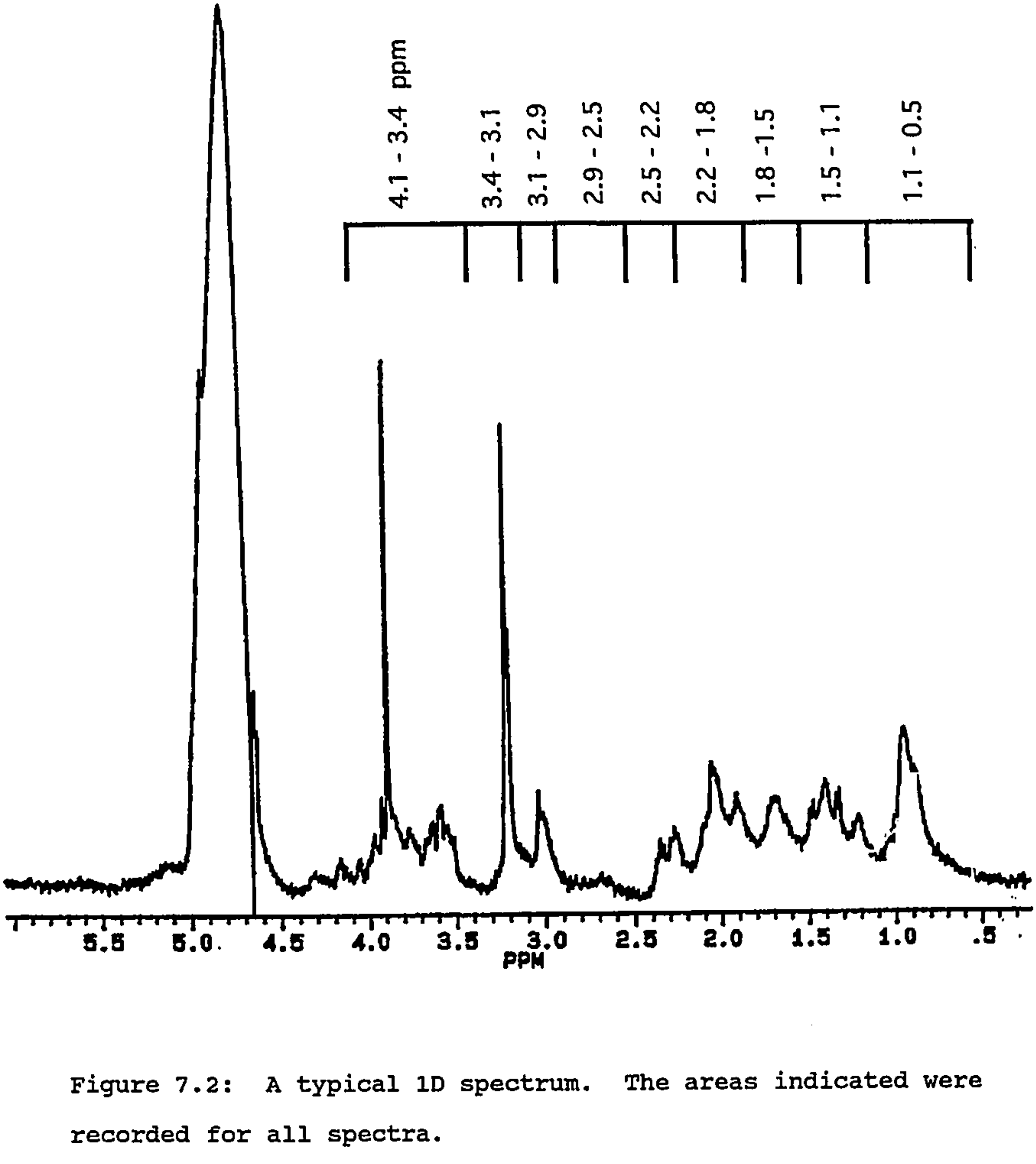

Figure 7.2: A typical 1D spectrum. The areas indicated were recorded for all spectra.

spectra could be broken up into these areas without dividing any peak into two areas. Figure 7.2 indicates these areas on a typical spectrum of a tumour. The area of the anisic acid peak at 7.0 ppm was also determined. The intensity of the 3.887 ppm peak relative to the 7.0 ppm peak was determined for the reference only and this information was used to subtract out intensity from the reference methoxy peak from the area between 4.1 and 3.4 ppm. Given the variety in size, texture and density of the samples areas were only reported as ratios or percentage of total signal minus the reference and water peak.

The COSY spectra were 2K by 160 points. In the t_2 dimension only the first 512 points were used and the t_1 dimension was zero filled to 512 points. A sine bell window was applied in both dimensions. This processing of the COSY spectrum ensured that short T_2 species such as lipids were detected (89). The COSY spectra were plotted from 8.04 ppm to 0.22 ppm and then symmetrized before plotting a more expanded COSY from 6.04 to 0.22 ppm. The 6.04 to 0.22 symmetrized plot was used to identify the useful crosspeaks. A transparent overlay was prepared on which each crosspeak was circled and numbered. New numbered peaks were added when they appeared in at least two COSY spectra. The overlay was placed over each COSY spectrum and the cross peaks present recorded. This was repeated on a later date, any discrepancies were reviewed and the data was entered into a LOTUS 123 file. This compiling of peaks was done in a blind fashion, i.e. the type of tumour was unknown until after the crosspeaks had been entered and finalized. Once the cross peaks had been recorded the data were compared to the pathological diagnosis.

Data from the T_2 experiments were processed automatically with line broadeneding of 1 Hz. The T_2 of the resonance at 1.3 ppm was determined. The automatic T_2 program was used to obtain a printout of peak intensity and tau values. The intensities were fitted using LOTUS 123 and the two exponential equation,

$$M_o(Ae^{(-tau/T_{2A})} + Be^{(-tau/T_{2B})}).$$

The two T_2 values and their relative contributions, A and B, were adjusted until the best match with the experimental data was obtained. Results from this visual fitting for two specimens was compared to analysis of the data using two different algorithms. The first, CONTIN, assigns a continuous distribution of T_2 values. The second considers the data to be a number of discrete relaxation times and fitted the data to mono, bi and tri exponentials.

7.2 Results and Discussion

Proton nuclear magnetic resonance was performed on a total of forty two samples from twenty six patients. Some duplicate samples were obtained, and normal samples were obtained whenever possible. Of these forty two samples, data from three samples were discarded because the samples were too small and thus signal to noise levels in the spectra were unacceptable. The pathology of the samples obtained and the number of patients is shown in Table 7.1. Included in the group of astrocytomas were three tumours of mixed pathology, oligodendroglioma and astrocytoma. Four samples in the group of astrocytomas were from recurrent tumours. In one case a specimen was obtained from the initial occurence of a tumour and the recurrent tumour approximately one year later. Two of the glioblastomas were recurrent tumours. The brain metastases included six adenocarcinomas from lung, one adenocarcinoma from breast. Both of the meningiomas were benign transitional meningiomas. One lymphoma was included in the study.

1D Spectra

Typical spectra for a glioblastoma and an astrocytoma are shown in Figures 7.3 and 7.4. The peak at 3.9 is due to

PROTON SPECTROSCOPY EX VIVO

PATHOLOGY	SAMPLES	PATIENTS
NORMAL TISSUE	11	10
ASTROCYTOMA	11	8
GLIOBLASTOMA	6	5
MENINGIOMA	3	2
METASTASES	7	7

Table 7.1: Tumours included in this study

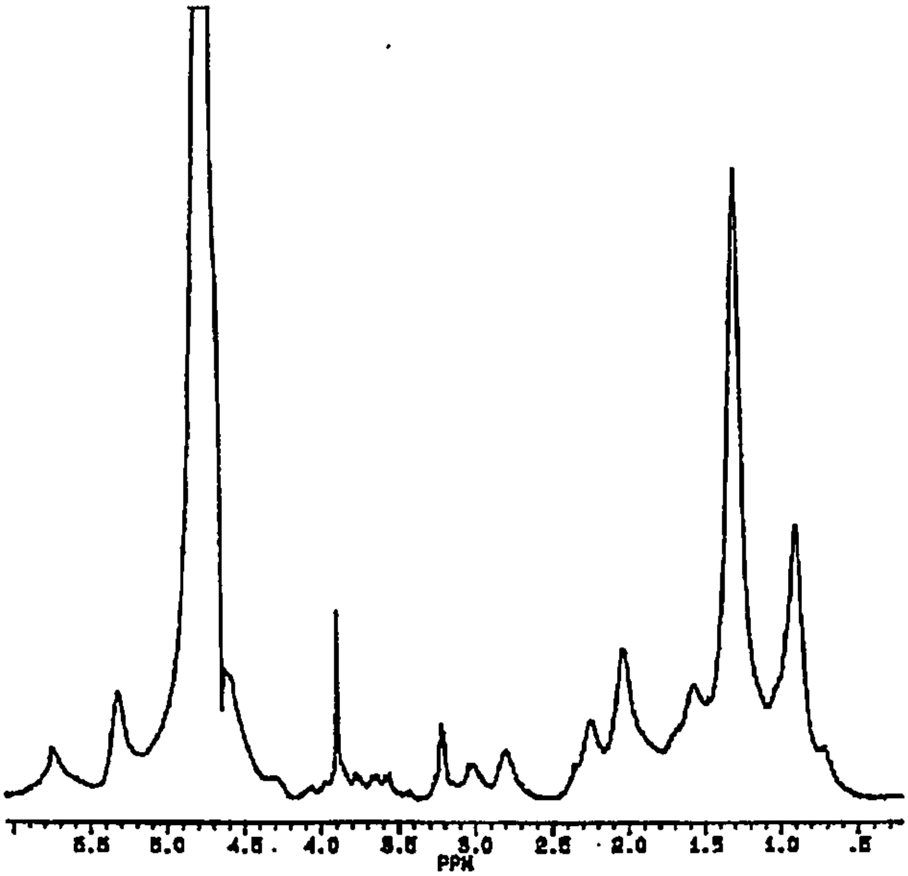

Figure 7.3: Typical spectrum from a glioblastoma.

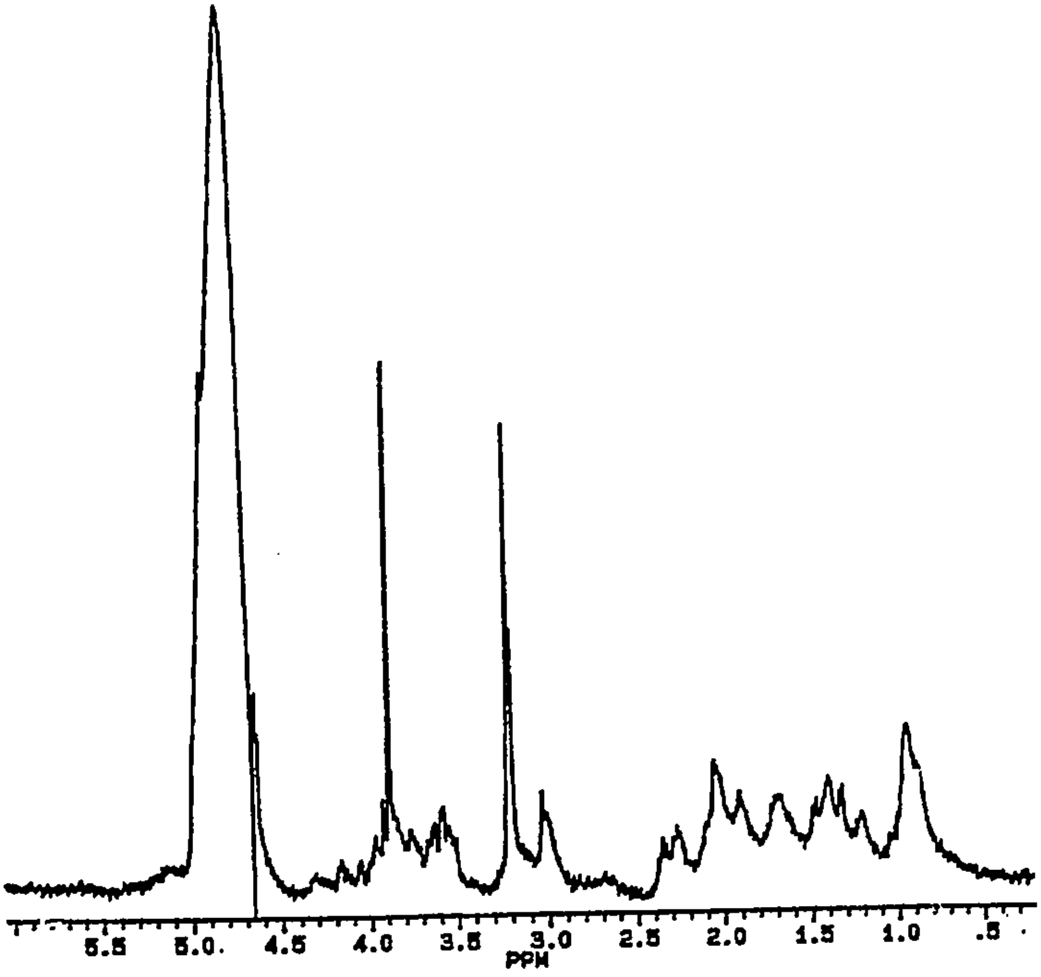

Figure 7.4: Typical spectrum from an astrocytoma.

the methoxy group of the anisic acid reference. Note the intensity at 1.3 ppm and 0.9 ppm in the spectrum of the glioblastoma. The astrocytoma has an intense peak at 3.2 ppm. In order to discriminate between these two pathologies, an area parameter, P, was defined as the ratio of the area between 3.4 ppm and 3.1 ppm over the area between 1.5 ppm and 1.1 ppm. This parameter discriminated glioblastomas and metastases from normal tissue and astrocytomas, but was not useful for separation from meningiomas. The area parameter, P, is plotted in Figure 7.5 for glioblastomas, astrocytomas and normal tissue. Values of P were greater than 0.19 for normals and astrocytomas and less than 0.19 for glioblastomas.

One glioblastoma and two samples from one recurrent astrocytoma cannot be classified according to pathological diagnosis when P is used as a criterion. The glioblastoma was classified as a malignant astrocytoma by the pathologist using the sample obtained by stereotaxic biopsy. The sample provided for spectroscopy was also taken during stereotaxic biopsy and according to the parameter, P, is an astrocytoma or a normal sample. The more abundant sample obtained during craniotomy and made available to the pathologist (but not for NMR) indicated that the pathology was consistent with a glioblastoma. The two samples from one recurrent astrocytoma were both classified with the glioblastoma and metastases

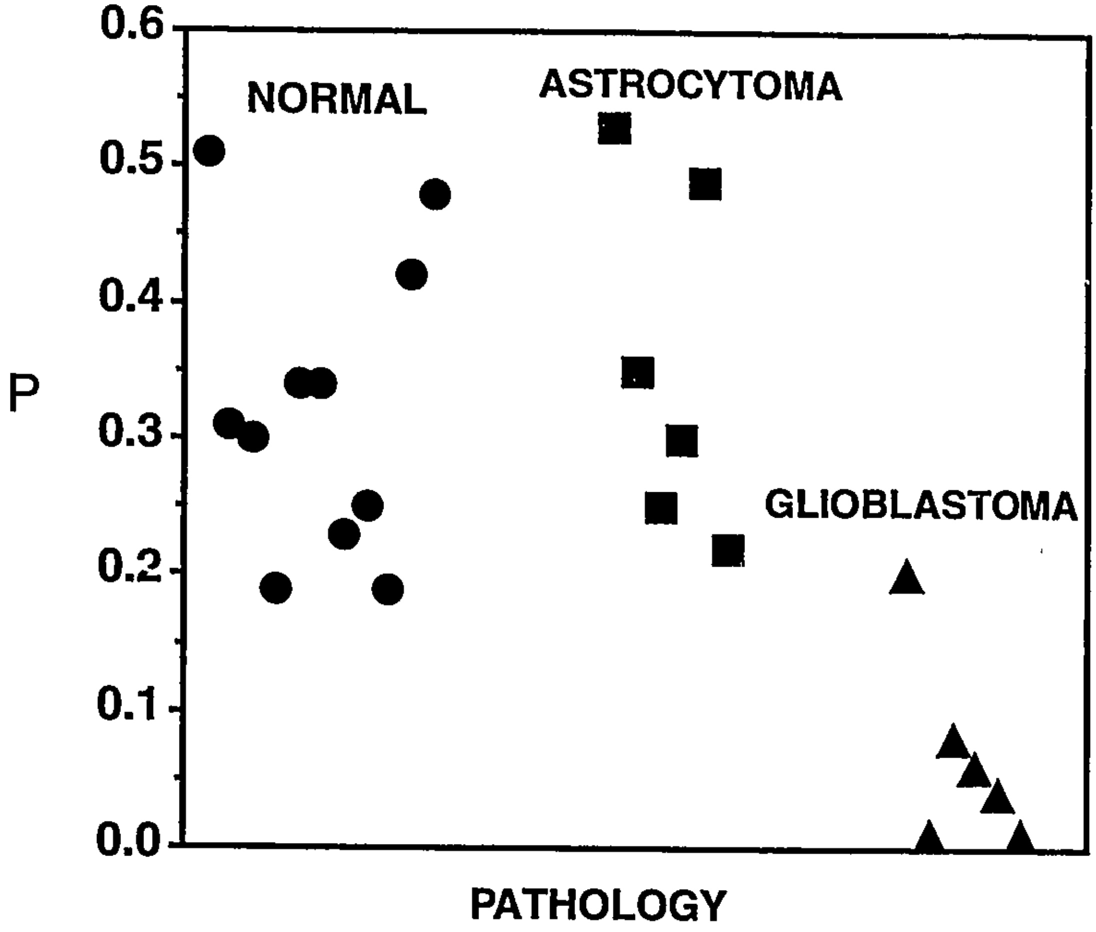

Figure 7.5: The area parameter, P, plotted as a function of pathology for normals and gliomas.

samples using the areas parameter, P. The malignant potential or biological aggressiveness of a recurrent astrocytoma is similar to that of a glioblastoma (90). Discrepancies between pathological diagnosis and diagnosis by spectroscopic parameters could be caused by errors in pathological diagnosis (91), or could reflect the sensitivity of spectroscopy to malignant potential (92). Error in pathological diagnosis could be caused by the portion submitted for initial pathological diagnosis not being representative of the entire tumour. Ultimately a comparison between patient survival time and this parameter would be most useful, as well as pathological grading of samples after spectroscopy.

Metastases from primary tumours elsewhere in the body are split into two groups using the parameter P value of 0.19. This value was chosen because it separated the glioblastomas from the astrocytomas and normals. Of the seven metastases five have a value of P less than 0.19 and are classified with the glioblastomas. The other two metastases have a value of P greater than 0.19 and are classified with the normals and the astrocytomas. The two tumours with P greater than 0.19 could not be distinguished from the other metastases by histopathological criterion. Further analysis of patient history and pathology reports yielded no further explanations as to the basis of the two groups of metastases. Both degree of differentiation of the tumours and the extent of metastases were considered.

The resonances at 1.3 ppm and 0.9 ppm are predominantly due to the methyl and methylene groups respectively of fatty acyl chains (93, 94). The NMR visibility of these moieties indicate that large amounts of triglycerides are present in the plasma membrane, and, that they are tumbling rapidly and isotropically (71). An increase in some types of lipids has been observed in brain tumours previously (95). These resonances are not visible in _in vitro_ NMR studies of extracts because the lipids are removed by the extraction procedure. The short T_2 of these lipids has made detection difficult _in vivo_, but with technical improvements, reports of lipids in brain tumours are being made (60). In a localized _in vivo_ proton NMR study of rat gliomas Remy _et al_ (96) demonstrated an increase in the 1.3 ppm lipid peak with increasing tumour size.

The resonance at 3.2 ppm is consistent with the $N(CH_3)_3^+$ group of choline. Increases in choline have been reported _in vivo_ in the proton spectra of astrocytomas (56, 97, 98, 99). Gill _et al_ (56) reported that the choline/creatine ratio was significantly higher in extracts of biopsy samples of grade IV astrocytomas as compared to normal and lower grade astrocytomas. In this study the area between 3.4 ppm and 3.1

ppm as a percentage of the total area of the spectrum (excluding water and reference peaks) was low in the glioblastomas relative to the astrocytomas and normal specimens. Normals and astrocytomas were indistinguishable.

In colon biopsy samples, the choline peak was found to increase in height and decrease in linewidth with increasing grade of tumour. However, in the terminal stages of cancer, this trend reverses (100, 101) and the linewidth increases and the peak height decreases becoming indistinguishable from normal tissue.

Gill et al (56) also reported that the alanine to choline ratio was significantly elevated in meningiomas. Peeling and Sutherland (58) found elevated alanine levels in the extracts of meningiomas and brain metastases. Because of the large methyl resonance at 1.3 ppm the alanine peak at 1.5 ppm could not always be clearly resolved.

The ex vivo proton NMR area parameter, P, predominantly reflects an increase in the 1.3 ppm peak which has been assigned to lipid methylene peaks. The doublet of lactic acid underlies these peaks but was not visible in any of the ex vivo spectra. The intense absorption at 1.3 ppm is characteristic of glioblastomas and most metastases and absent in the spectra of specimens such as normal tissue, astrocytomas and meningiomas. These observations support the hypotheses of Mountford _et al_ that these lipid peaks are indicative of malignancy (72).

COSY Spectra

The COSY spectrum resolves some of the crowded information in the 1D proton spectrum. Typical COSY spectra of a glioblastoma and an astrocytoma are shown in Figures 7.6 and 7.7. In Figure 7.8 the overlay is shown illustrating the numbering of the COSY cross peaks. The COSY spectra in Figures 7.6 and 7.7 are dramatically different due to the significant intensity in five cross peaks in the glioblastoma. These cross peaks which predominate in the COSY spectrum of the glioblastoma, are not present in the COSY spectrum of the astrocytoma. The presence of these five peaks appears to correspond to the intensity at 0.9 ppm and 1.3 ppm in the 1D spectra discussed above.

These five peaks which were numbered 2, 2a, 15, 24, and 25, were used to separate the samples into two groups: group 1 composed of glioblastomas and five out of seven metastases; and group 2 composed of astrocytomas, meningiomas, two remaining metastases and normal tissue. No specimen from normal brain, meningiomas or astrocytomas had

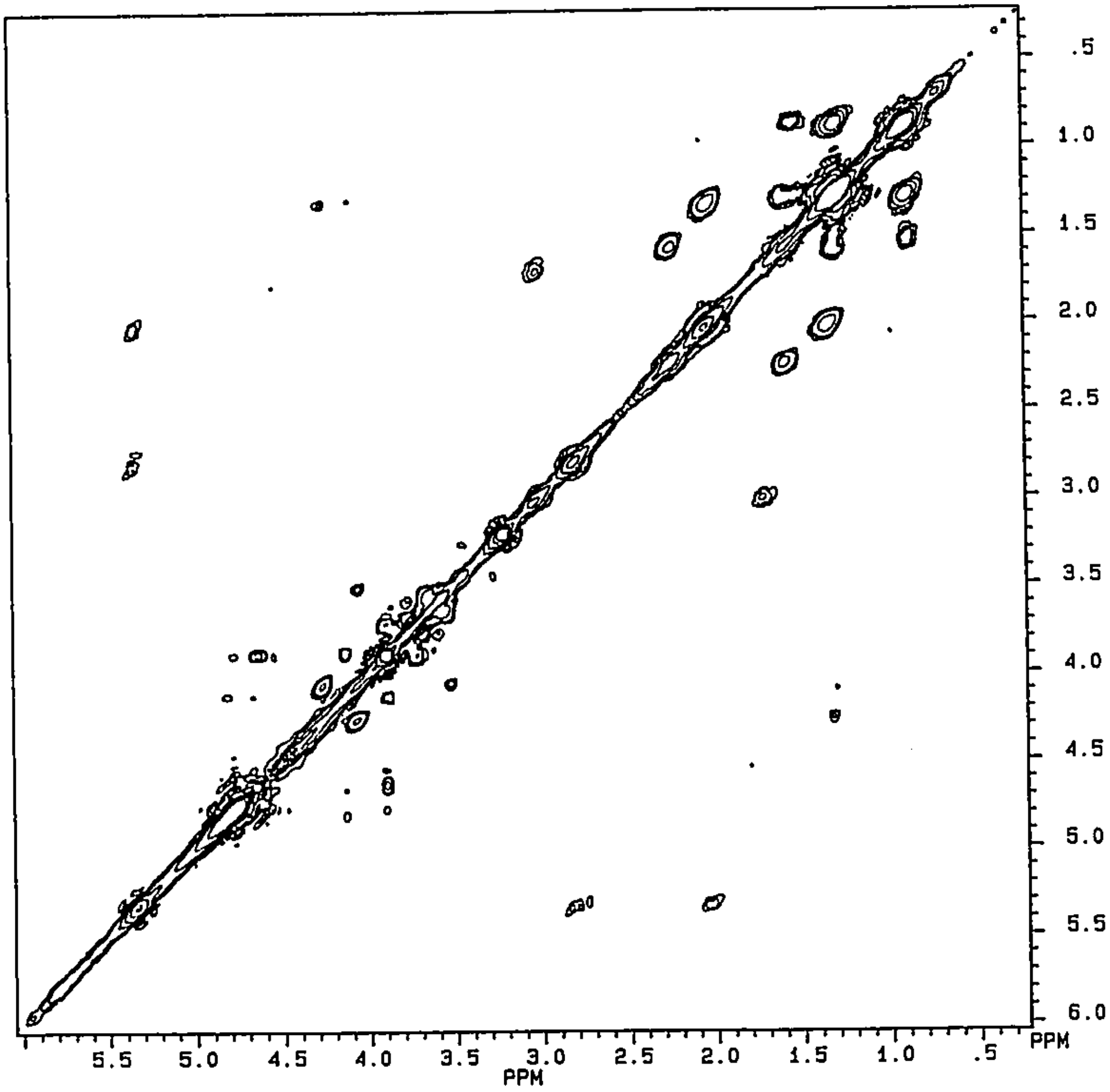

Figure 7.6: 2D COSY spectrum of a glioblastoma

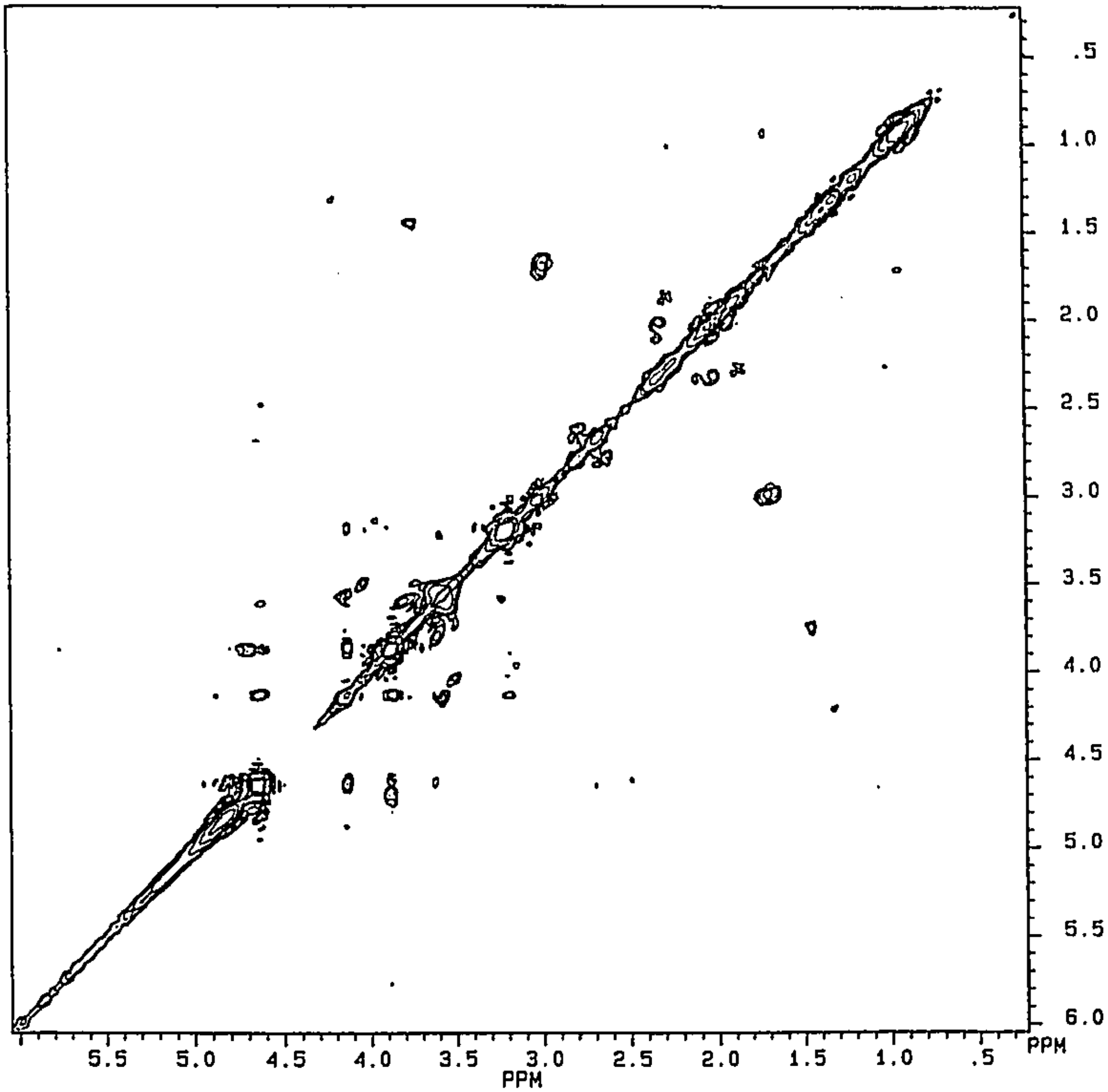

Figure 7.7: 2D COSY spectrum of an astrocytoma.

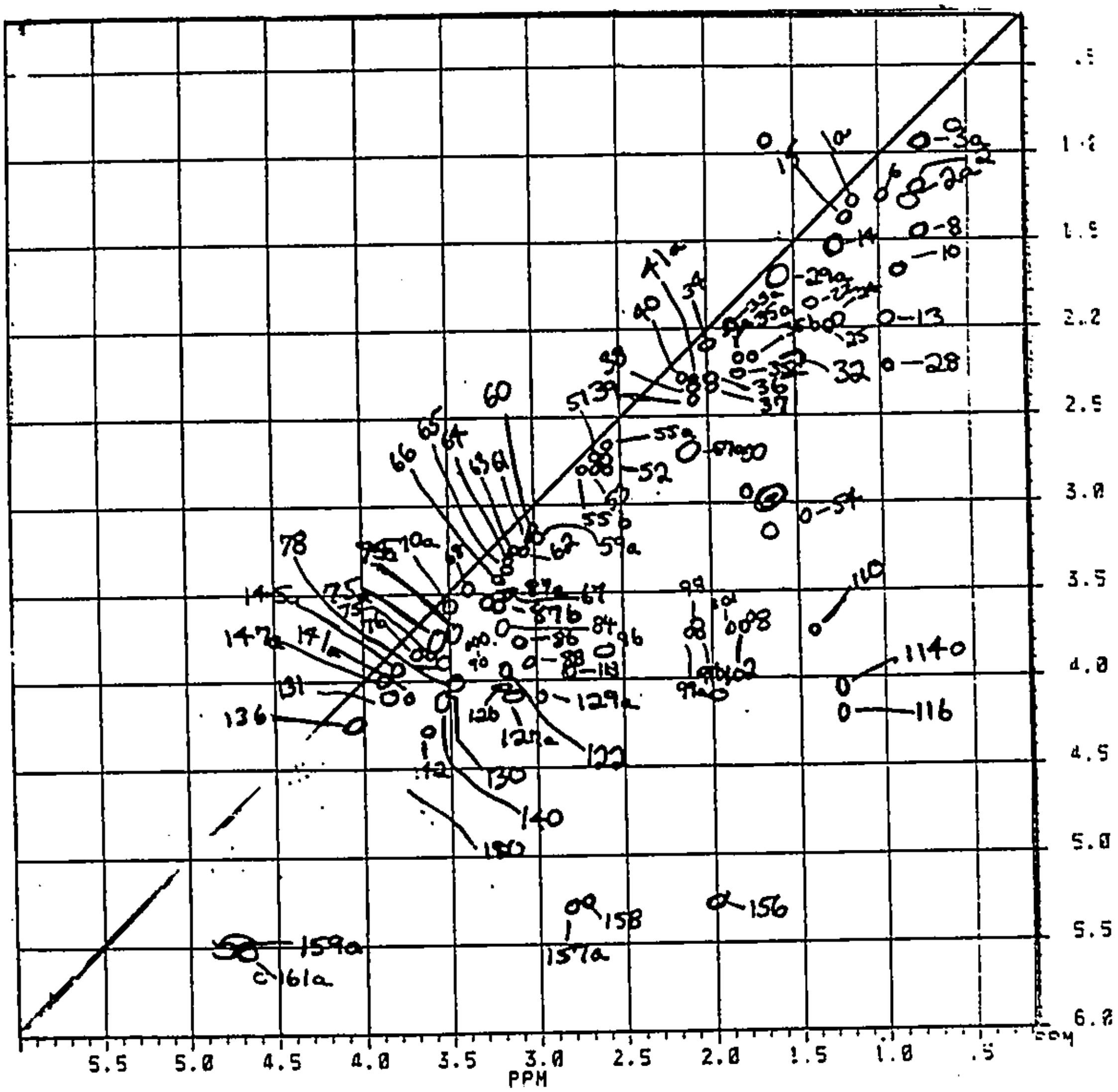

Figure 7.8: Numbering of crosspeaks in the 2D COSY spectrum.

all these peaks present, and if any of the five peaks were present, they were of low intensity. One recurrent astrocytoma (which could also not be classified according to the pathological diagnosis using the 1D area parameter, P) was the only exception to this. As discussed above, this discrepancy could be caused by error in the pathological diagnosis (most likely caused by an unrepresentative sample). Alternatively, the cross peaks in the COSY may be providing information not available in the standard pathological examination of the tissue, such as malignant potential.

The grouping of the metastases mirrored the classification by the one dimensional area parameter, P. As discussed earlier for the 1D spectra, nothing in patient history or in the pathology of the tumour could explain the separate grouping of two out of the seven metastases. With the metastases the spectroscopy appears to be providing new information which at this point is difficult to interpret.

The five cross peaks were compared to literature values (64, 65, 93). The cross peaks 2, 2a probably represent only one coupling, as do the cross peaks 24 and 25. The crosspeak 2/2a is at 1.35 and 0.9 and is consistent with the methyl methylene coupling in fatty acids (93) as shown in Figure 7.9. The 24/25 crosspeak is at 2.05 and 1.3 and is

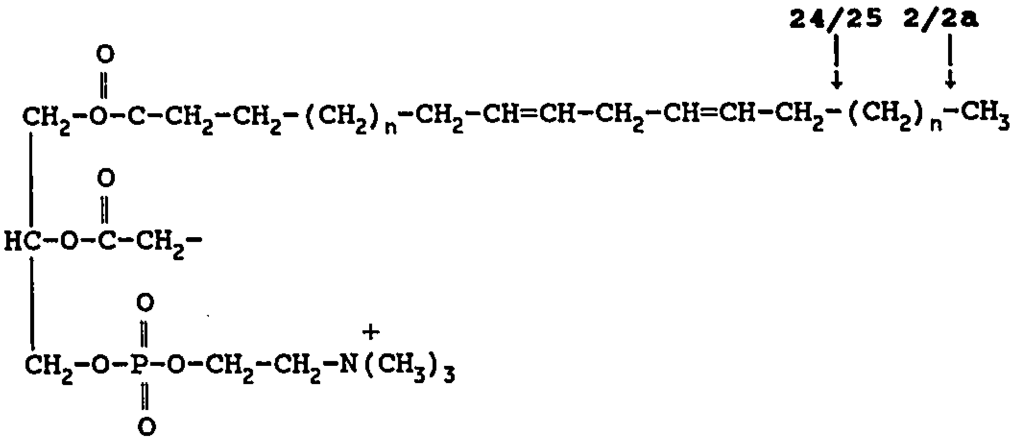

Figure 7.9: Possible assignments for crosspeaks 2/2a and 24/25.

consistent with the coupling shown in the figure.

The 2D COSY crosspeaks were used to classify all groups of tumours according to their pathology. This is illustrated in Figure 7.10. Glioblastomas can be separated from the group of five metastases by the presence of all the following crosspeaks: 1a, 14, 32, 51, 53, 70a, 114, and 145a. The COSY spectrum of all five metastases specimens had all of these cross peaks, and no COSY spectrum of a glioblastoma sample had all these cross peaks. The only astrocytoma in group 1, was classified as a glioblastoma by this scheme. This astrocytoma was recurrent and the classification as a glioblastoma may better reflect the malignant potential of the tumour than the pathological classification. The other two metastases could not be classified by their COSY spectra. One is erroneously classified as a normal specimen and the other as an astrocytoma by the scheme in Figure 7.10. Because the COSY spectra of the meningiomas had all of cross peaks 34, 39, 41a, 55b, 66, 86, 95a, 102, and 118, they can be separated from the group 2, composed of meningiomas, normal samples and astrocytomas. None of the meningiomas, normal samples or astrocytomas had all of these peaks. Similarly the COSY spectra of the astrocytomas and oligoastrocytomas had all of the following peaks: 1a, 10, 28, 33a, 36, 38, 52, 53, 60, 61,76, 127a, and 130, whereas no normal spectra have all these crosspeaks.

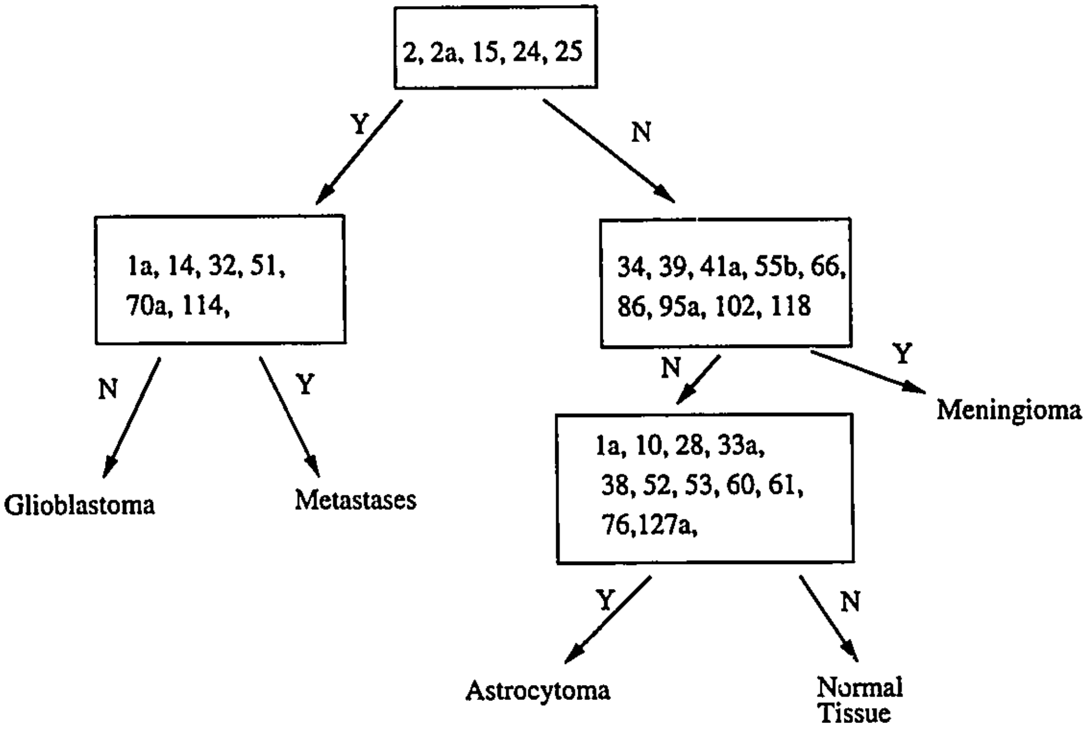

Figure 7.10: Classification scheme using COSY crosspeaks.

The classification of the tumours according to pathology beyond the initial division into two groups, was at times based only on the presence of one or two cross peaks. The discrimation of the tumour groups in this manner is tenuous. With the addition of more samples, it may be become evident that certain cross peaks are critical and that the classification scheme in Figure 7.10 is valid. Alternatively, as the groups grow larger they may become more diverse and the ability to discriminate amongst them may be lost.

T_2 Experiments

In all specimens, the T_2 of the resonance at 1.3 ppm could be fitted by means of a double exponential using visual criterion of goodness of fit. The first T_2 component ranged from 20 to 120 ms. The longer T_2 ranged from 250 to 1200 ms. The contribution or weighing of the first and shorter component was usually larger, with the weighting ranging from 0.45 to 0.75 for this component.

The data for the long T_2 component, plotted against pathology, is shown in Figure 7.11. Groupings similar to those evident in the 1D spectra and the 2D COSY spectra were apparent in the long T_2 data. Normal brain and glioblastomas were clearly separated with normal brain having a significantly longer long T_2 component than glioblastomas. Astrocytomas overlap both normal brain and glioblastoma. Astrocytomas are plotted, according to grade in Figure 7.11. The length of the long T_2 component correlates negatively with increasing grade. Recurrent tumours, which have a malignant potential similar to that of glioblastomas, have shorter "long T_2" components. In Figure 7.11, the metastases demonstrate the same two groups evident in the COSY and 1D spectra data. Two metastases are grouped with the normal tumours and five are grouped with the glioblastomas.

The shorter "long T_2" component was evident in the glioblastomas, recurrent astrocytomas and the majority of metastases. A longer value for this "long T_2" component was characteristic of normal brain tissue and astrocytomas of grades I to II. The brain tumours studied in this thesis suggest that the shorter long T_2 component is characteristic of malignant potential in the brain. This is an unexpected conclusion because, as discussed in Chapter 3, Mountford *et al* (70, 72) reported a very long T_2 component at 1.3 ppm in malignant cell lines and malignant human ovarian and colonic tumours.

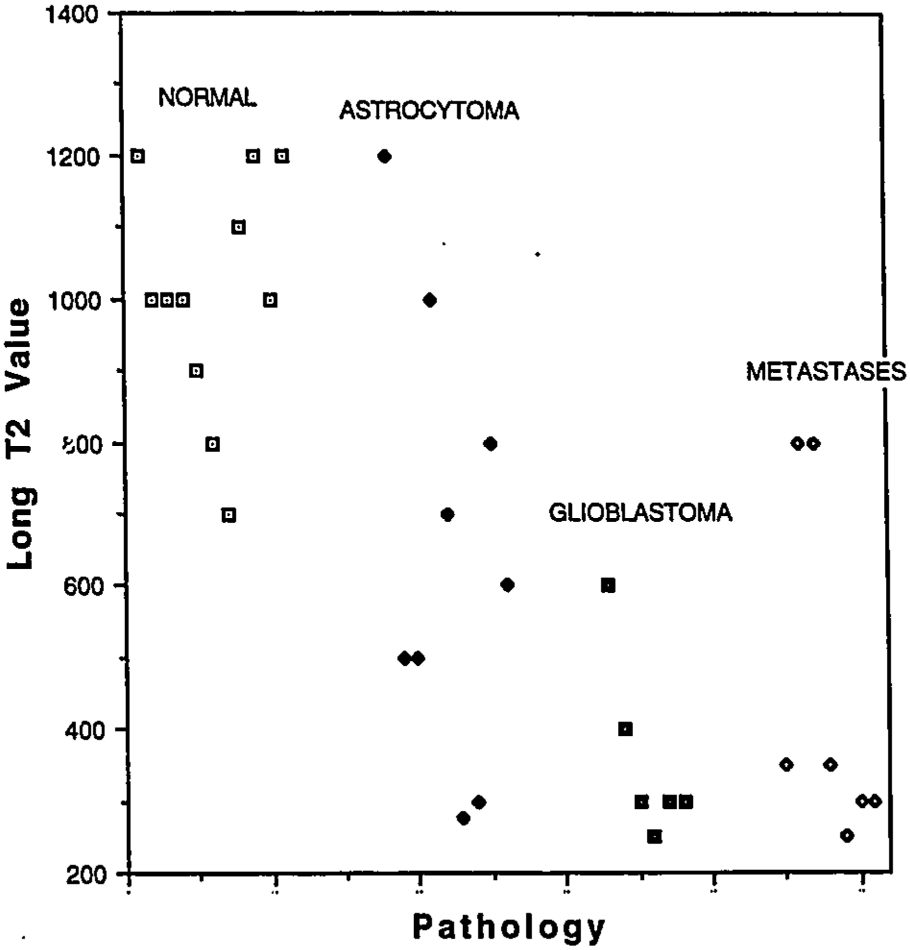

Figure 7.11: The "long T_2" component versus pathology.

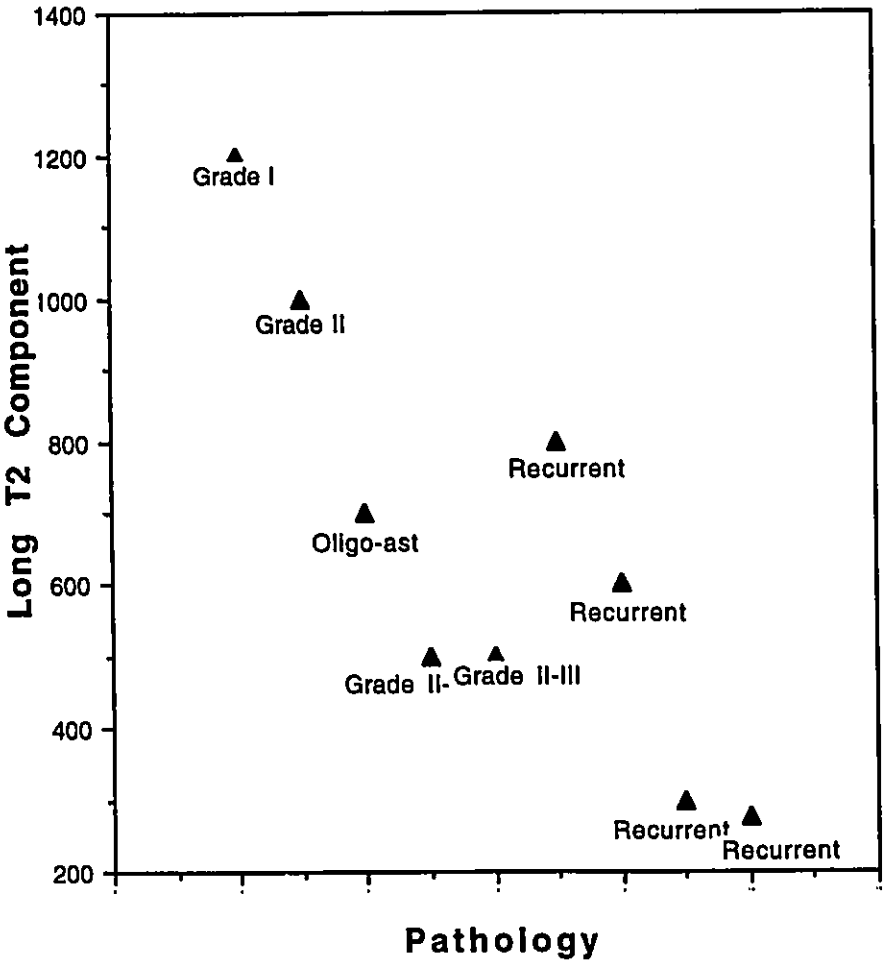

Figure 7.12: The "long T_2" component plotted for astrocytomas with the grade of tumour indicated. Note the trend towards a longer "long T_2" component with lower grades.

7.3. Conclusions

The *ex vivo* specimens were successfully classified according to pathological diagnosis using the two dimensional COSY spectra. The one dimensional spectra and the COSY spectra appear to reflect malignancy, with glioblastomas, the most malignant brain tumours, and the majority of the metastases, which originate from very malignant tumours, being classified together. The less malignant specimens of astrocytomas, meningiomas and normal tissue were in another group. The basis for the discrimination between these two groups appears to be the presence of lipids in both the one dimensional spectrum and the COSY spectrum. The finer discrimination of these two groups was possible using the COSY spectra. Not all metastases could be classified properly and one recurrent astrocytoma was classified as a glioblastoma. Classifications which do not agree with histological diagnosis may be yielding additional information regarding degree of malignancy. The recurrent astrocytoma could have the malignant potential of a glioblastoma and the two metastases classified in the less malignant group, may for some reason be exhibiting less biological aggressiveness than the other metastases.

The transverse relaxation times of the resonance at 1.3

ppm were fitted to a two exponential equation. The "long T_2" component clearly discriminated glioblastomas from normal brain tissue. The astrocytomas had a large range of the long T_2 component, and the grade of tumour could be roughly correlated with the grade of the tumour.

Chapter 8

Proton Spectroscopy of Extracts of Human Brain Tumour Biopsies

Extracts were made from tumour specimens if sufficient tissue remained after the ex vivo spectroscopy was performed. Extract spectra have better resolution and less contamination from lipids and proteins, which facilitates identification of metabolites. Just as more information is available in the ex vivo spectra discussed in Chapter 7, as compared to in vivo spectra, the simpler in vitro extract spectra can yield information not available in the ex vivo spectra.

8.1. Materials and Methods

Sample Preparation

Extracts (65, 102) were prepared from brain tumour biopsy specimens after a sample for ex vivo spectroscopy had been taken. If the entire brain tumour specimen was not used for ex vivo proton spectroscopy (Chapter 7) the remaining portion of the sample was refrozen. The remaining portion of the sample was usually left thawed for approximately one hour, until initial shimming was performed. Once it was clear that the sample setup of the ex vivo proton spectroscopy was free of air bubbles the remaining sample was frozen at -70°C.

To prepare the extract the sample was first lyophilized. The sample was allowed to thaw and taken out of the PBS-D_2O in which it had been frozen. The wet sample was weighed and the sample was placed in an Eppendorf tube which had a small hole punched in the top. The sample was refrozen in liquid nitrogen and then left on the freeze drier overnight.

The freeze-dried sample was weighed and added to 10 mg of silica (BDH Chemicals) in a glass test tube. A metal rod was used to grind the sample with the silica. 200 μL of cold perchloric acid from Aldrich Chemical Company (7%) were added, the sample vortexed and left on ice for at least three minutes. After centrifuging for two minutes, the supernatant was added to a second glass test tube containing 0.036 mL of 2.5 M potassium carbonate (Anachemia). The sample was re-extracted by adding another 200 μL of perchloric acid to the initial precipitate remaining in the first tube, and, again was left on ice for three minutes, centrifuged for two minutes and the supernatant was added to a third test tube containing 0.036 mL of 2.5 M potassium carbonate. The second and third test tubes were vortexed and left on ice for at least one minute. After centrifuging these two test tubes, the supernatants were combined. The pH of the extract was checked using pH paper. The pH was adjusted to 6.5 to 7.0.

The extract was added to an Eppendorf tube with a hole in the top for freeze-drying. The extract was frozen in liquid nitrogen and left overnight on the freeze drier. Once removed from the drier, the dried extract was stable as long as the tube was sealed with Parafilm until needed for spectroscopy.

Spectroscopy

The extract was dissolved in 400 μL of D_2O and centrifuged. The supernatant was adjusted to pH 7.0 using DCl and NaOD (Aldrich Chemical Company, Inc.) and 350 μL of the extract solution was placed in a 5 mm NMR tube. A reference solution of 5 mM or 2.5 mM anisic acid was inside a glass insert of approximate o.d. 1 mm. This sealed reference was inserted into the 5 mm NMR tube. The temperature control unit of the spectrometer was set at 292°K.

Spectroscopy was performed as described for 1D *ex vivo* samples in section 7.1 of the previous chapter. For some samples a 60^{0} pulse was used. Linewidth at half height was approximately 1 Hz.

8.2. Results and Discussion

High resolution spectroscopy was performed on a total of ten extracts. The pathology of the samples from which the extracts were taken was as follows: four normal brain samples, three astrocytoma samples, one glioblastoma sample, and two brain metastases samples. The two metastases were adenocarcinomas with one originating from lung, and the other originating from breast tissue. The three astrocytoma samples included one oligoastrocytoma.

Peaks in the extract spectra were identified by comparison to brain extract spectra and published lists of chemical shifts (58, 65, 103, 104). No quantification of metabolites was attempted because, as described in the materials and methods section above, samples destined to become extracts were left thawed usually for at least one hour.

A spectrum of an extract of an oligoastrocytoma is shown in Figure 8.1. The reference peak of the methoxy group of anisic acid is at 3.88 ppm. The dominant peaks in the spectrum are the reference, the doublet of the lactate

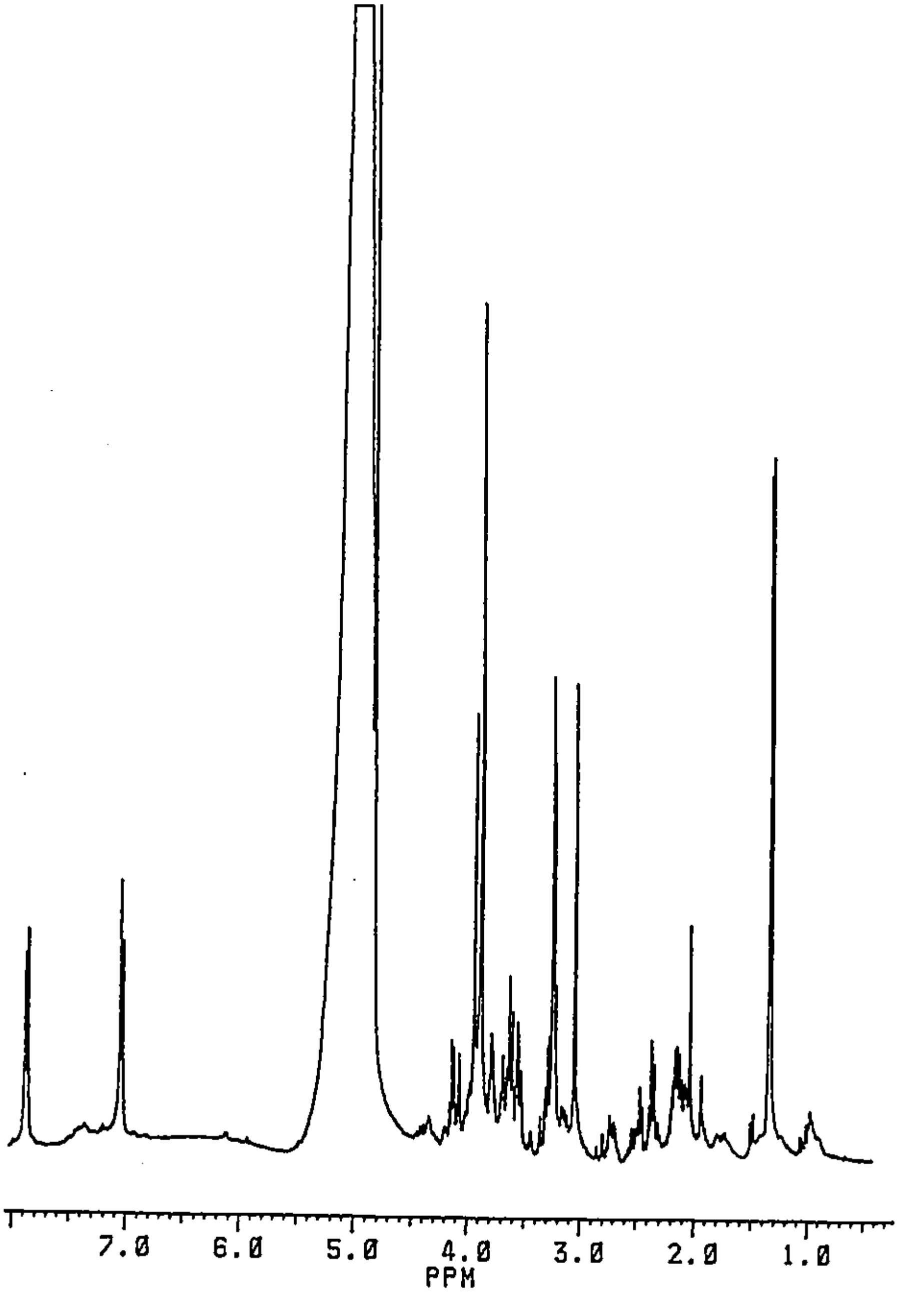

Figure 8.1: Extract spectrum of an oligoastrocytoma.

anion at 1.3 ppm, the acetate anion singlet at 1.92 ppm, creatine and phosphocreatine peaks at 3.0 and 3.9 ppm, and choline and phosphocholine peaks at 3.2 and 3.6 ppm. A partial list of the chemical shift values used to identify the peaks in the extracts are listed in Table 8.1.

The intensity of the lactate peak in the extract spectra was compared to the intensity at 1.3 ppm in the *ex vivo* samples (Chapter 7). The *ex vivo* spectra of the glioblastoma and the metastases from breast were dominated by resonances at 1.3 and 0.9 ppm. These resonances were attributed to lipids. While the extract spectra of these samples contain some lactate, a comparison to the *ex vivo* spectra indicates that the contribution of lactate to the peak at 1.3 ppm in the *ex vivo* spectra is small.

Other compounds, which were present in the spectra but not in such high concentrations, were glutamate, glutamine, alanine, valine, N-acetyl-aspartate (NAA) and leucine. The NAA peak was quite variable in intensity, ranging from being not present at all, to higher than the creatine peak in some spectra. NAA peak was present in the extract spectra of some of the gliomas. Compounds such as inositol, glycine and GABA (γ-aminobutyric acid) have also been reported in extracts of human brain tissue (58, 104). These compounds may be present in the extracts presented in this thesis, but are of low

COMPOUND	CHEMICAL SHIFT
lactate	1.33 d, 4.11 q
acetate	1.92 s
NAA	2.01 s, 4.38 dd, 2.48 dd
creatine	3.04 s, 3.93 s
phosphocreatine	3.05 s, 3.94 s
choline	3.21 s, 3.50 t, 4.05 t
phosphocholine	3.22 s, 3.61 t, 4.19 t
glutamate	2.09 m, 2.34 dt, 3.75 t
glutamine	2.14 m, 2.45 m, 3.77 t
glycine	3.56 s
leucine	0.94 d, 0.96 d, 1.69 m, 1.72 m, 3.69 t
alanine	1.47 d, 3.18 t
valine	0.98 d, 1.05 d, 2.26 m, 3.55 d

Table 8.1: Partial list of chemical shift values used to identify peaks in the extract spectra. (s=singlet, d=doublet, t=triplet, q=quartet, m=multiplet, dd=doublet of doublets, dt=doublet of triplets)

concentration and/or are obscured by other peaks in the spectra. As can be seen from Figure 8.1, there are many low lying peaks which cannot be identified.

8.3. Conclusion

The extract spectra in this thesis serve to identify many of the metabolites present in the spectra of normal brain and brain tumour extracts. The spectra are consistent with those previously reported in the literature (58, 104) with lactate, acetate, choline compounds and creatine compounds dominating the spectra. No attempt was made at quantification or comparison of metabolite levels due to the treatment of the samples before extraction. There was large diversity in the extract spectra of tumours of a given type. The low levels of NAA found in the extract spectra of some of the gliomas could be attributed to infiltrating brain tissue (58). The levels of lactate in the extract spectra support the data in Chapter 7, indicating that the resonance at 1.3 ppm in the *ex vivo* spectra is predominantly due to the methylene of lipids.

CHAPTER 9

Summary and Future Work

The work in this thesis explored two avenues of attacking a significant medical problem - the lethality of human brain tumours. With modern medical science the life of a patient diagnosed with a malignant brain tumour can be extended for only six to twelve months (8). The two approaches used towards researching this problem were ^{31}P chemical shift imaging *in vivo* and ^{1}H spectroscopy *ex vivo*. The application of nuclear magnetic resonance to brain tumour research has only started within the last five years and thus the research in this thesis leaves many questions unanswered.

9.1. Phosphorus Chemical Shift Imaging of Brain Tumours

Summary

In the last few years a number of *in vivo* studies of human brain tumours using phosphorus NMR have been published

(1, 6, 82, 83). Results from many studies are conflicting, but some of these studies have indicated that phosphorus NMR may have great promise in three areas of brain tumour research; eliminating invasive biopsies (4, 6), yielding biochemical information (1, 2) and predicting response to therapy (38, 39, 105).

Given the promising but conflicting results of the studies and the great need for progress in brain tumour therapies, more research is obviously needed. In this thesis chemical shift imaging was used to obtain in vivo phosphorus spectra of brain tumours. While CSI had previously been demonstrated to be applicable to human brain tumours (45, 46, 47), only a few test cases of brain tumours using CSI have been previously reported.

The one dimensional CSI sequence was successfully written and tested on a Siemens Magnetom 1.5 T imager, and implemented using a surface coil. Spectra from patients were obtained from voxels with a 9 cm diameter and a 1 or 1.5 cm thickness. Once the 1D CSI sequence was routinely being applied to patients, the writing and application of a three dimensional localization technique was begun. The two dimensional CSI with slice select was successfully used on volunteers, but due to the large size of the voxels, the poorer signal to noise, and the number of patients already accrued in the 1D CSI study, the sequence was never used on brain tumour patients.

PME/ATP, PDE/ATP, PCr/ATP, Pi/ATP, and pH were useful parameters which were calculated for all spectra from the 1D CSI of brain tumour patients and normal volunteers. The multiple spectra obtained from each subject reflected the heterogeneity of the brain tumours. By choosing the highest value for each parameter, statistical differences were found between the tumours and normal brain. PME/ATP and PDE/ATP were high in glioblastomas and astrocytomas. Pi/ATP and PCr/ATP were also high in astrocytomas. All tumours had normal to alkaline pH. Only meningiomas had consistently alkaline pH and normal levels of PME/ATP and PDE/ATP. Brain metastases were a diverse group and had no unique characteristics in the phosphorus spectra.

Future Work

The most significant problem with studying human brain tumours is obtaining a sufficient number of patients. The study in this thesis should be continued until the number of subjects for each group is much larger. Multi-site studies may be required to accrue sufficient patients. In light of the improved technology such as stronger magnets and improvements in coil design, now available, 1D CSI with a surface coil could be called a "primitive" technique. However, to prove or disprove statistically the clinical usefulness of in vivo spectroscopy a large study, using one technique only, is necessary. The use of computerized data analysis is now being applied to in vivo spectroscopy. This will allow for a more comprehensive comparison of normal and tumour spectra.

With the improved technology mentioned above the signal to noise problems of the 2D CSI with slice select technique can be improved and voxels can be made smaller. The three dimensional localization method has the advantage of obtaining spectra from the unaffected hemisphere of the brain. The hemisphere of the brain without tumour could serve as the control for the tumour and this would be a significant improvement over using normal volunteers as controls. The heterogeneity of tumours demonstrated in this study and others (58) could be explored using the 2D CSI with slice select technique with a surface coil.

9.2. Ex vivo and in vitro Proton Spectroscopy

Summary

Proton spectroscopy of cells and biopsy samples have been shown to yield information regarding the malignancy of the tissue observed (3, 72). It also has the potential to characterize brain tumours (56, 58) and to further our understanding of the metabolism of brain tumours (63). Long T_2 components and COSY spectra determined from _ex vivo_ cancer specimens have been useful in characterizing a tissue as malignant (72, 92).

In this thesis, the _ex vivo_ proton spectroscopy of brain tumours showed that 1D spectra, 2D COSY spectra and T_2 data are all useful in discriminating the tumour types according to histopathological classifications. The data indicated that information regarding malignancy and the biological aggressiveness of brain tumours is available from _ex vivo_ proton spectroscopy.

In the 1D spectra, a parameter P was defined as the ratio of the areas between 3.4 and 3.1 ppm and 1.5 to 1.3 ppm. This parameter could be used to discriminate between the normal brain and glioblastoma specimens in this thesis. Crosspeaks in the COSY spectra could be used to distinguish between glioblastomas, astrocytomas, meningiomas, brain metastases and normal brain. One recurrent astrocytoma was classified as a glioblastoma by this scheme. This misclassification according to histopathology may be an example of the proton spectra recognizing the similar malignant potentials of a recurrent astrocytoma and a glioblastoma. Two metastatic tumours also cannot be classified by their COSY spectra. The long T_2 component of the resonance at 1.3 ppm is longer for normals and astrocytomas, as compared to glioblastomas. The value of this component correlates roughly to the grade of the astrocytoma.

Proton spectroscopy of extracts was used to identify the predominent peaks in the spectra of brain tumours. These peaks were identified by comparison to other studies of proton extracts of brain (58, 104). The lactate anion, the acetate anion, creatine and choline derivatives and, in some cases NAA dominated the extract spectra. When compared, the ex vivo spectra contained these peaks, but also contained the lipid peaks at 0.9 and 1.3 ppm which were removed by the extraction procedure.

Future Work

As was the case for the phosphorus CSI, more samples are required for the ex vivo spectroscopy to verify the results in this thesis. To verify that the data are reflecting malignant potential and biological aggressiveness of the tumours, patients in this study must be followed over the long term. The proton NMR data can then be correlated to patient outcome, and not just to histopathological grading. Analysis of the spectra could also be performed by more sophisticated approaches such as computer analysis.

Appendix 1

SESMS Imaging Sequence

```
!--------------------------------------------------------------------------!
!                  loaded from file       DUAO:[KROEKER.SEQ]SESMS.UCQ;1    !
!    sequence      compatible version     VC2/GBS2                         !
!                  saving date            22-JAN-1987 11:16:36.17          !
!                  owner                  SIEMENS                          !
!--------------------------------------------------------------------------!
!
.comment=   SESMS.UCQ
!
!------------------------- global parameters ------------------------------!
!
!  .available     directives are controlling the possible features
!                 that  are  available  with  this  sequence file
!
.available/FREQUENCY_RANGE/min=  40.000/max=  65.000
.available/MAX_GRAD_AMPL    =10.000
.available/SEQUENCE_TYPE    = IMAGING
.available/GATING           = YES
.available/IR_SEQUENCE      = no
.available/MULTIECHO_CPGM   = no
.available/3DIM             = no
.available/PHASE_IMAGE      = YES
.available/SLICE_SHIFT      = YES
.available/CHEMICAL_SHIFT   = no
.available/FILTER/GAUSS= YES /HANNING= YES /FERMI= YES /default=none
.available/INTERPOLATIONS/SINC= YES /default=SINC
.available/MATRIX/SQUARE= YES /RECTANGULAR= no /HALF_FOURIER_ISO = no
.available/MATRIX/EXTENDED= YES
!
!   .dialog        parameters for the  dialog choices in NUMARIS
!
.dialog/SEQUENCE_STRING = SE
.dialog/MATRIX_TO_CALC /min=     128/max=     256/inc= BASE2  /def=     256
.dialog/LINES          /min=     128/max=     256/inc= BASE2  /def=     256
.dialog/COLUMNS        /min=     128/max=     512/inc= BASE2  /def=     256
.dialog/ACQUISITIONS   /min=       1/max=     128/inc= BASE2  /def=       1
.dialog/3D_PART_THICKNESS/min=   0.000
.dialog/3D_PARTITIONS     /min=      0
.dialog/TR      /num=  1/min=  40000/max=20000000/inc=    1000
.dialog/TI      /num=  1/min=      0/max=       0/inc=       0
.dialog/TE      /num=  1/min=  15000/max=   22000/inc=    1000
.dialog/SLICES         /min=       1/max=      20/inc=       1
.dialog/SLICE_THICK    /min=   2.000/max=  20.000/inc=   1.000
.dialog/SLICE_DIST     /min=   0.500/max=  99.000/inc=   0.010
.dialog/ZOOM_FACTOR    /min=   1.000/max=   5.000/inc=   0.010
.dialog/PARAXIAL_ANGLE / none
.dialog/SAMPLE_INTERVAL/min=       0/max=       0/inc=       5
.dialog/PREPARING_SCANS/min=       1/max=      20/inc=       1/def=       6
.dialog/FLIP_ANGLE_ALPHA /none
.dialog/RF_BAND_WIDTH  /none
.dialog/GATING_RATIO   /min=   0.100/max=   1.000/inc=   0.100/def=   0.200
.dialog/LINES_GATE_OPEN/min=       1/max=   65535/inc=       1/def=       1
.dialog/MEASURE_TIME_FACTOR=   1.000
!
!    .dps       (Data  Processing  System)  directives  for the
!               preprocessing and FFT software in the BSP & VAX
!
.dps/CALC_ALGO          = SE
.dps/LOOP_STRUCTURE     = SE
.dps/LINE_FFT           = no
.dps/OFFSET_IGNORE      = no
.dps/NO_ME_COMBINATION  = no
.dps/HALF_FOURIER       = no  /TYPE= none     /LINES_AFTER_ZERO=    8
.dps/ECHO_ALTERNATING   = YES
```

```
!
!
!
!
! .gradampl   the  logical  reference gradient amplitudes in  [mT/m] for
!          matrix 256, zoom factor 1.0, slice thickness 10 mm, FOV 50cm
!
.gradampl/GP=  1.566000 GR=  1.566000/GS=  2.400000
.gradampl/GS_MIN=  1.200000/GS_MAX= 10.000000
!
!    .msc     parameters for the  Measurement and Sequence Controller
!
.msc/trigger/NUMBEROFSCANS=sliceloop
!
!
.external /     SRF_FILENAME = none
.external /     R_P_FILENAME = none
.external /GRAD_TAB_FILENAME = none
!
.adj/CHEM_SHIFT_MAX_TIME =      0
.adj/READOUT_TIME =    7680
!
!
|--------------------------- sequence timing ----------------------------|
.TIMINGTABLE
!Time/ | RF-Cabinet| ADC-|  Gradient Amplitude Factor  |Sync-|Relative
! usec |   01 |  02 | Type|phasecode| readout |selection| Bits|  Time
!
.do /OFFSET /REP=  1                ! offset correction measurement  +
   1000                                                 OSCO      1000
   3000                                                           4000
   7680             ON                                           11680
   8320                                                          20000
.end                                ! offset correction measurement  +
!
.do /LINES                          ! fourier lines loop - - - - - - +
.do /ACQUISITIONS                   ! acquisitions loop  - - - - - - +
.do /PREPARE                        ! prepare the inner loops  * - - +
.do /SLICES                         ! slice loop, I=SLICE/SERIES - - +
   1000                                       PULS01    OSCO      1000
   2560 SRF01                                 PULS01              3560
   1400                   TAB01     PULS02                        4960
   1140                   TAB01     PULS02    PULS03              6100
   1300                   TAB01     PULS02                        7400
    100                             PULS02                        7500
TEFIL01                                                              !
   1000                                       PULS01              8500
   2560 SRF02                                 PULS01             11060
    480                                       PULS01             11540
TEFIL01                                                              !
    400                                                          11940
   1500                             PULS04                       13440
   7680             ON              PULS04                       21120
  15000                                       PULS05             36120
   3880                                                          40000
TRFIL01                                                              !
.end                                ! slice loop - - - - - - - - - - - +
.RF / ALTERNATE
.end                                ! prepare loop - + * + - + * + - +
.end                                ! acquisitions loop  - - - - - - +
.end                                ! fourier lines loop - - - - - - +
.END / TIMINGTABLE
!
|------------------------ rf types definitions --------------------------|
```

```
!Name   | ce |angle|angle| code  |pointer| factor  |uator | pts.|algorithm
SRF01     I      90    90    +-       1     1.2500000   1       512  NORMAL
SRF02     I     180     0    ++       2     1.9000000   1       512  NORMAL
.END / RFTABLE
!
!
!
!--------------------- gradient table definitions -----------------------!
.GRADTABLE
!TAB-|  Steps   |  First  |  Last   |Calc| RAMP-UP-params |RAMP-DOWN-params
!Name| through |amplitude|amplitude|algo|algo|samp| time |algo|samp| time
TAB01  LINES    -1.000000 1.0000000 NORM NORM   20   1000 NORM   20   100
.END / GRADTABLE
!
!--------------------- gradient puls definitions ------------------------!
.PULSTABLE
PULS01 1.0000000 NORM   20   1000 NORM   20   1000
PULS02 1.1776650 NORM   20   1000 NORM   20   1000
PULS03 -1.000000 NORM   20   1000 NORM   20   1000
PULS04 1.0000000 NORM   20   1000 NORM   20   1000
PULS05 #-8.00000 NORM   20   1000 NORM   20   1000
.END / PULSTABLE
!
.END
```

Appendix 2

FTNMR Algorithms

AR2

```
for row 1 &nrows
re &file
con
bc
em
ft
sr &row
ty row=&row
next
fl
end
```

AR11

```
for col 1 &ncol
lc &col
zf 32
ft
sc &col
next
fl
end
```

CONDIF

```
zbf 1
sd 0
ift
psh
em 30
mul .9
sbf 1
lbf 1
ft
sd 0
psh
end
```

AR3D1

```
for bf 1 32
zbf &bf
next
sd 0
for matrix 1 7
smx 3d&matrix
lr &3d
psh
next
smx 3d8
lr &3d
end
```

AR3D2

```
smx 3db&3d 32 512
for buffer 1 8
lbf &buffer
sr &buffer
next
fl
end
```

AR3D3

```
for col 1 &ncol
lc &col
zf 32
ft
sc &col
next
fl
end
```

Appendix 3

Chemical Shift Imaging Sequences

CSI1DE16.UCR

```
!-----------------------------------------------------------------------------!
!                  loaded from file      DUAO:[SPEC]CSI1DE16.UCR;1            !
!    sequence      compatible version    VC2/GBS2                             !
!                  saving date           26-JAN-1990 18:01:51.66              !
!                  owner                 USER                                 !
!-----------------------------------------------------------------------------!
!
.comment=   SESMS.UCR
!
!-------------------------  global parameters  -------------------------------!
!
!  .available    directives are controlling the possible features
!                that  are  available  with  this  sequence file
!
.available/FREQUENCY_RANGE/min=  40.000/max=  65.000
.available/MAX_GRAD_AMPL    =10.000
.available/SEQUENCE_TYPE    = IMAGING
.available/GATING           = no
.available/IR_SEQUENCE      = no
.available/MULTIECHO_CPGM   = no
.available/3DIM             = no
.available/PHASE_IMAGE      = YES
.available/SLICE_SHIFT      = YES
.available/CHEMICAL_SHIFT   = no
.available/FILTER/GAUSS= YES /HANNING= YES /PERMI= YES /default=none
.available/INTERPOLATIONS/SINC= no  /default=none
.available/MATRIX/SQUARE= YES /RECTANGULAR= no /HALF_FOURIER_ISO = no
.available/MATRIX/EXTENDED= YES
!
!   .dialog       parameters for the  dialog choices in NUMARIS
!
.dialog/SEQUENCE_STRING = SE
.dialog/MATRIX_TO_CALC /min=        8/max=    1024/inc= BASE2  /def=      256
.dialog/LINES          /min=        8/max=     256/inc= BASE2  /def=      256
.dialog/COLUMNS        /min=      512/max=    1024/inc= BASE2  /def=      128
.dialog/ACQUISITIONS   /min=        1/max=     512/inc= BASE2  /def=        1
.dialog/3D_PART_THICKNESS/min=   0.000
.dialog/3D_PARTITIONS    /min=       0
.dialog/TR     /num=  1/min=  262000/max=20000000/inc=     1000
.dialog/TI     /num=  1/min=       0/max=       0/inc=        0
.dialog/TE     /num=  1/min=       0/max= 1000000/inc=     1000
.dialog/SLICES         /min=        1/max=      20/inc=        1
.dialog/SLICE_THICK    /min=    2.000/max=  20.000/inc=    1.000
.dialog/SLICE_DIST     /min=    0.000/max=  99.000/inc=    0.010
.dialog/ZOOM_FACTOR    /min=    1.000/max=   3.000/inc=    0.010
.dialog/PARAXIAL_ANGLE / none
.dialog/SAMPLE_INTERVAL/min=        0/max=       0/inc=        0
.dialog/PREPARING_SCANS/min=        1/max=      20/inc=        1/def=        6
.dialog/FLIP_ANGLE_ALPHA /none
.dialog/RF_BAND_WIDTH  /none
.dialog/GATING_RATIO   /min=    0.100/max=   1.000/inc=    0.100/def=    0.200
.dialog/LINES_GATE_OPEN/min=        1/max=   65535/inc=        1/def=        1
!
!    .dps      (Data  Processing  System)  directives  for the
!              preprocessing and FFT software in the BSP & VAX
!
.dps/CALC_ALGO         = none
.dps/LOOP_STRUCTURE    = FID
.dps/LINE_FFT          = no
.dps/OFFSET_IGNORE     = no
```

```
.dps/NO_ME_COMBINATION = no
.dps/HALF_FOURIER      = no  /TYPE= none     /LINES_AFTER_ZERO=    8
.dps/ECHO_ALTERNATING  = no
.dps/DIRAC_ELIMINATION = no
.dps/3D_RESOLUTION_FFT = no
.dps/TIMEOUT_FACTOR    =   1.000
!
!
!
!
! .gradampl   the  logical  reference gradient amplitudes in  [mT/m] for
!           matrix 256, zoom factor 1.0, slice thickness 10 mm, FOV 50cm
!
.gradampl/GP=  1.566000/GR=  1.566000/GS=  1.800000
.gradampl/GS_MIN=  1.200000/GS_MAX= 10.000000
!
!   .msc     parameters for the  Measurement and Sequence Controller
!
.msc/trigger/NUMBEROFSCANS=sliceloop
.msc/GRADIENT_DELAY_CORRECTION = no
.msc/PARAX_RAMPTIME_INCREMENT  = none
!
!
.external/SRF /none
.external/     R_P_FILENAME = none
.external/GRAD_TAB_FILENAME = none
!
.adj/CHEM_SHIFT_MAX_TIME =     0
.adj/READOUT_TIME =  256000
!
!
!=========================== sequence timing ============================!
.TIMINGTABLE
!Time/ | RF-Cabinet| ADC |     Gradient references     |Sync-|Relative
! usec |  01 |  02 |      |phasecode| readout |selection| Bits|  Time
!
.do /OFFSET /REP=  1                ! offset correction measurement  +
   1000                                                  OSCO      1000
   3000                                                            4000
 256000            ON                                            260000
  50000                                                          310000
.end                                ! offset correction measurement  +
!
.do /LINES                          ! fourier lines loop - - - - - - +
.do /ACQUISITIONS                   ! acquisitions loop  - - - - - - +
.do /PREPARE                        ! prepare the inner loops  * - - +
.do /SLICES                         ! slice loop, I=SLICE/SERIES - - +
   1000                                                  OSCO      1000
    250 R_P01                                                      1250
    540                    TAB01                                   1790
    835                                                            2625
 256000            ON                                            258625
   3570                                                          262195
TRFIL01                                                               !
.end                                ! slice loop - - - - - - - - - - +
.end                                ! prepare loop - + * + - + * + - +
.end                                ! acquisitions loop  - - - - - - +
.end                                ! fourier lines loop - - - - - - +
.END / TIMINGTABLE
!
```

```
!------------------------ rf types definitions ---------------------------!
.RFTABLE
!RFType|Sli-|Flip |Phase|Altern.| Scale |Empirical|Atten-|Supp-| Calc.
!Name  | ce |angle|angle| code  |pointer| factor  |uator | pts.|algorithm
R_P01          90    90    ++      1               1       1  NORMAL
.END / RFTABLE
!
!
!
!--------------------- gradient table definitions -----------------------!
.GRADTABLE
!TAB-| Steps |         Amplitudes         |Calc| RAMP-UP-params |RAMP-DOWN-params
!Name|through|  First |  Last   | Offset |algo|algo|samp| time |algo|samp| time
TAB01  LINES  #-4.0500 #4.05000 0.000000 NORM NORM   30   540  NORM   30    540
.END / GRADTABLE
! ·
!--------------------- gradient pulse definitions -----------------------!
.PULSETABLE
!Pulse| pulse   | RAMP-UP-params |RAMP-DOWN-params
!Name |amplitude|algo|samp| time |algo|samp| time
PULS01 1.0000000 NORM   20   1000 NORM   20   1000
.END / PULSETABLE
!
.END
```

CSIDE18.UCR

```
!---------------------------------------------------------------------------!
!                 loaded from file      DUAO:[SPEC]CSIIDE18.UCR;1            !
!    sequence     compatible version    VC2/GBS2                             !
!                 saving date            7-FEB-1990 19:20:16.01              !
!                 owner                 USER                                 !
!---------------------------------------------------------------------------!
!
.comment=   SESMS.UCR
!
!-------------------------- global parameters ------------------------------!
!
!  .available    directives are controlling the possible features
!                that  are  available  with  this  sequence file
!
.available/FREQUENCY_RANGE/min=  40.000/max=  65.000
.available/MAX_GRAD_AMPL   =10.000
.available/SEQUENCE_TYPE   = IMAGING
.available/GATING          = no
.available/IR_SEQUENCE     = no
.available/MULTIECHO_CPGM  = no
.available/3DIM            = no
.available/PHASE_IMAGE     = YES
.available/SLICE_SHIFT     = YES
.available/CHEMICAL_SHIFT  = no
.available/FILTER/GAUSS= YES /HANNING= YES /FERMI= YES /default=none
.available/INTERPOLATIONS/SINC= no  /default=none
.available/MATRIX/SQUARE= YES /RECTANGULAR= no /HALF_FOURIER_ISO = no
.available/MATRIX/EXTENDED= YES
!
!   .dialog       parameters for the  dialog choices in NUMARIS
!
.dialog/SEQUENCE_STRING = SE
.dialog/MATRIX_TO_CALC /min=       8/max=    1024/inc= BASE2  /def=     256
.dialog/LINES          /min=       8/max=     128/inc= BASE2  /def=     256
.dialog/COLUMNS        /min=     256/max=    1024/inc= BASE2  /def=     128
.dialog/ACQUISITIONS   /min=       1/max=     512/inc= BASE2  /def=       1
.dialog/3D_PART_THICKNESS/min=   0.000
.dialog/3D_PARTITIONS    /min=       0
.dialog/TR     /num=  1/min=  262000/max=20000000/inc=     1000
.dialog/TI     /num=  1/min=       0/max=       0/inc=        0
.dialog/TE     /num=  1/min=       0/max= 1000000/inc=     1000
.dialog/SLICES         /min=       1/max=      20/inc=        1
.dialog/SLICE_THICK    /min=   2.000/max=  20.000/inc=    1.000
.dialog/SLICE_DIST     /min=   0.000/max=  99.000/inc=    0.010
.dialog/ZOOM_FACTOR    /min=   1.000/max=   3.000/inc=    0.010
.dialog/PARAXIAL_ANGLE / none
.dialog/SAMPLE_INTERVAL/min=       0/max=       0/inc=        0
.dialog/PREPARING_SCANS/min=       1/max=      20/inc=        1/def=      6
.dialog/FLIP_ANGLE_ALPHA /none
.dialog/RF_BAND_WIDTH  /none
.dialog/GATING_RATIO   /min=   0.100/max=   1.000/inc=    0.100/def=  0.200
.dialog/LINES_GATE_OPEN/min=       1/max=   65535/inc=        1/def=      1
!
!    .dps        (Data  Processing  System)  directives  for the
!                preprocessing and FFT software in the BSP & VAX
!
.dps/CALC_ALGO          = none
.dps/LOOP_STRUCTURE     = FID
.dps/LINE_FFT           = no
.dps/OFFSET_IGNORE      = no
```

```
.dps/NO_ME_COMBINATION = no
.dps/HALF_FOURIER      = no  /TYPE= none     /LINES_AFTER_ZERO=    8
.dps/ECHO_ALTERNATING  = no
.dps/DIRAC_ELIMINATION = no
.dps/3D_RESOLUTION_FFT = no
.dps/TIMEOUT_FACTOR    =   1.000
!
!
!
!
! .gradampl   the  logical  reference gradient amplitudes in  [mT/m] for
!           matrix 256, zoom factor 1.0, slice thickness 10 mm, FOV 50cm
!
.gradampl/GP=  1.566000/GR=  1.566000/GS=  1.800000
.gradampl/GS_MIN=  1.200000/GS_MAX= 10.000000
!
!    .msc     parameters for the  Measurement and Sequence Controller
!
.msc/trigger/NUMBEROFSCANS=sliceloop
.msc/GRADIENT_DELAY_CORRECTION = no
.msc/PARAX_RAMPTIME_INCREMENT  = none
!
!
.external/SRF /none
.external/     R_P_FILENAME = none
.external/GRAD_TAB_FILENAME = none
!
.adj/CHEM_SHIFT_MAX_TIME =     0
.adj/READOUT_TIME =  256000
!
!
!========================== sequence timing ============================!
.TIMINGTABLE
!Time/ | RF-Cabinet| ADC |     Gradient references     |Sync-|Relative
! usec |  01 |  02 |      |phasecode| readout |selection| Bits|  Time
!
.do /OFFSET /REP=  1                ! offset correction measurement  +
   1000                                                 OSCO      1000
   3000                                                           4000
 256000           ON                                            260000
  50000                                                         310000
.end                                ! offset correction measurement  +
!
.do /LINES                          ! fourier lines loop - - - - - - +
.do /ACQUISITIONS                   ! acquisitions loop  - - - - - - +
.do /PREPARE                        ! prepare the inner loops  * - - +
.do /SLICES                         ! slice loop, I=SLICE/SERIES - - +
   1000                                                 OSCO      1000
    250 R_P01                                                     1250
    540               TAB01                                       1790
    835                                                           2625
 256000           ON                                            258625
   3570                                                         262195
TRFIL01                                                              !
.end                                ! slice loop - - - - - - - - - - +
.end                                ! prepare loop - + * + - + * + - +
.end                                ! acquisitions loop  - - - - - - +
.end                                ! fourier lines loop - - - - - - +
.END / TIMINGTABLE
!
```

```
!========================= rf types definitions ===========================!
.RFTABLE
!RFType|Sli-|Flip |Phase|Altern.| Scale |Empirical|Atten-|Supp-| Calc.
!Name  | ce |angle|angle| code  |pointer| factor  |uator | pts.|algorithm
R_P01            90    90    ++       1                   1       1  NORMAL
.END / RFTABLE
!
!
!
!===================== gradient table definitions =======================!
.GRADTABLE
!TAB-| Steps |         Amplitudes        |Calc| RAMP-UP-params |RAMP-DOWN-params
!Name|through|  First |  Last  | Offset |algo|algo|samp| time |algo|samp| time
TAB01  LINES  #-5.4000 #5.40000 0.000000 NORM NORM   30   540  NORM   30    540
.END / GRADTABLE
! '
!===================== gradient pulse definitions =======================!
.PULSETABLE
!Pulse| pulse   | RAMP-UP-params |RAMP-DOWN-params
!Name |amplitude|algo|samp| time |algo|samp| time
PULS01 1.0000000 NORM   20   1000 NORM   20   1000
.END / PULSETABLE
!
.END
```

CSI3DE19.UCR

```
!==========================================================================!
!                 loaded from file      DUA0:[SPEC]CSI3DE19.UCR;1           !
!    sequence     compatible version    VC2/GBS2                            !
!                 saving date           22-MAR-1991 17:35:00.61             !
!                 owner                 USER                                !
!==========================================================================!
!
.comment=   SESMS.UCR
!
!========================= global parameters ==============================!
!
!  .available    directives are controlling the possible features
!                that  are  available  with  this  sequence file
!
.available/FREQUENCY_RANGE/min=  40.000/max=  65.000
.available/MAX_GRAD_AMPL   =10.000
.available/SEQUENCE_TYPE   = IMAGING
.available/GATING          = no
.available/IR_SEQUENCE     = no
.available/MULTIECHO_CPGM  = no
.available/3DIM            = no
.available/PHASE_IMAGE     = no
.available/SLICE_SHIFT     = no
.available/CHEMICAL_SHIFT  = no
.available/FILTER/GAUSS= YES /HANNING= YES /FERMI= YES /default=none
.available/INTERPOLATIONS/SINC= no  /default=none
.available/MATRIX/SQUARE= YES /RECTANGULAR= no /HALF_FOURIER_ISO = no
.available/MATRIX/EXTENDED= YES
!
!   .dialog       parameters for the  dialog choices in NUMARIS
!
.dialog/SEQUENCE_STRING = SE
.dialog/MATRIX_TO_CALC /min=       8/max=    1024/inc= BASE2  /def=     256
.dialog/LINES          /min=       1/max=       4/inc= BASE2  /def=     256
.dialog/COLUMNS        /min=     512/max=    1024/inc= BASE2  /def=     128
.dialog/ACQUISITIONS   /min=       1/max=     512/inc= BASE2  /def=       1
.dialog/3D_PART_THICKNESS/min=   0.100
.dialog/3D_PARTITIONS    /min=       4
.dialog/TR      /num=  1/min=  135000/max=20000000/inc=    1000
.dialog/TI      /num=  1/min=       0/max=       0/inc=       0
.dialog/TE      /num=  1/min=       0/max= 1000000/inc=    1000
.dialog/SLICES         /min=       1/max=       1/inc=       1
.dialog/SLICE_THICK    /min=   2.000/max=  20.000/inc=   1.000
.dialog/SLICE_DIST     /min=   0.000/max=  99.000/inc=   0.010
.dialog/ZOOM_FACTOR    /min=   1.000/max=   3.000/inc=   0.010
.dialog/PARAXIAL_ANGLE / none
.dialog/SAMPLE_INTERVAL/min=       0/max=       0/inc=       0
.dialog/PREPARING_SCANS/min=       1/max=      20/inc=       1/def=       6
.dialog/FLIP_ANGLE_ALPHA /none
.dialog/RF_BAND_WIDTH  /none
.dialog/GATING_RATIO   /min=   0.100/max=   1.000/inc=   0.100/def=   0.200
.dialog/LINES_GATE_OPEN/min=       1/max=   65535/inc=       1/def=       1
!
!    .dps      (Data  Processing  System)  directives  for the
!              preprocessing and FFT software in the BSP & VAX
!
.dps/CALC_ALGO          = none
.dps/LOOP_STRUCTURE     = FID
.dps/LINE_FFT           = no
.dps/OFFSET_IGNORE      = no
```

```
.dps/NO_ME_COMBINATION = no
.dps/HALF_FOURIER      = no  /TYPE= none     /LINES_AFTER_ZERO=    8
.dps/ECHO_ALTERNATING  = no
.dps/DIRAC_ELIMINATION = no
.dps/3D_RESOLUTION_FFT = no
.dps/TIMEOUT_FACTOR    =   1.000
!
!
!
!
! .gradampl   the  logical  reference gradient amplitudes in  [mT/m] for
!           matrix 256, zoom factor 1.0, slice thickness 10 mm, FOV 50cm
!
.gradampl/GP=  1.566000/GR=  1.566000/GS= none
.gradampl/GS_MIN= none     /GS_MAX= none
!
!    .msc     parameters for the  Measurement and Sequence Controller
!
.msc/trigger/NUMBEROFSCANS=sliceloop
.msc/GRADIENT_DELAY_CORRECTION = no
.msc/PARAX_RAMPTIME_INCREMENT  = none
!
!
.ext/SRF/SL/mi=  2.0/ma= 20.0/GS= 2.000000/FI=[USER]SE_04D1_1.EXT
.external/     R_P_FILENAME = none
.external/GRAD_TAB_FILENAME = none
!
.adj/CHEM_SHIFT_MAX_TIME =     0
.adj/READOUT_TIME =  128000
!
!
!=========================== sequence timing ============================!
.TIMINGTABLE
!Time/ | RF-Cabinet| ADC |      Gradient references      |Sync-|Relative
! usec |  01  |  02 |       |phasecode| readout |selection| Bits|  Time
!
.do /OFFSET /REP=  1                  ! offset correction measurement  +
   1000                                                 OSC0       1000
   3000                                                            4000
 256000              ON                                          260000
  50000                                                          310000
.end                                  ! offset correction measurement  +
!
.do /LINES                            ! fourier lines loop - - - - - - +
.do /ACQUISITIONS                     ! acquisitions loop  - - - - - - +
.do /3DPARTITIONS                     ! 3D partition loop  - - - - - - +
.do /PREPARE                          ! prepare the inner loops  * - - +
.do /SLICES                           ! slice loop, I=SLICE/SERIES - - +
     540                                       PULS01    OSC0       540
     640 SRF01                                 PULS01              1180
     540                                                           1720
     910                                       PULS02              2630
     835                                                           3465
  128000              ON                                         131465
    3535                                                         135000
 TRFIL01                                                              !
 .end                                 ! slice loop - - - - - - - - - - +
 .end                                 ! prepare loop - + * + - + * + - +
 .end                                 ! 3D partition loop  - - - - - - +
 .end                                 ! acquisitions loop  - - - - - - +
```

```
.end                                   ! fourier lines loop - - - - - - +
.END / TIMINGTABLE
!
!======================== rf types definitions ==========================!
.RFTABLE
!RFType|Sli-|Flip |Phase|Altern.| Scale |Empirical|Atten-|Supp-| Calc.
!Name  | ce |angle|angle| code  |pointer| factor  |uator | pts.|algorithm
SRF01    I     90    90     ++      1    1.0000000   1     256       5
.END / RFTABLE
!
!
!
!===================== gradient pulse definitions ======================!
.PULSETABLE
!Pulse| pulse    ! RAMP-UP-params |RAMP-DOWN-params
!Name |amplitude|algo|samp| time |algo|samp| time
PULS01 #3.150000 NORM   30    540 NORM   30    540
PULS02 #-2.90000 NORM   30    540 NORM   30    540
.END / PULSETABLE
!
.END
```

CSI3DE24.UCR

```
!==========================================================================!
!                 loaded from file      DUAO:[SPEC]CSI3DE24.UCR;1          !
!    sequence     compatible version    VC2/GBS2                           !
!                 saving date            5-APR-1991 18:59:04.76            !
!                 owner                 USER                               !
!==========================================================================!
!
.comment=   SESMS.UCR
!
!======================== global parameters ===============================!
!
!  .available    directives are controlling the possible features
!                that  are  available  with  this  sequence file
!
.available/FREQUENCY_RANGE/min=  40.000/max=  65.000
.available/MAX_GRAD_AMPL   =10.000
.available/SEQUENCE_TYPE   = IMAGING
.available/GATING          = no
.available/IR_SEQUENCE     = no
.available/MULTIECHO_CPGM  = no
.available/3DIM            = YES
.available/PHASE_IMAGE     = no
.available/SLICE_SHIFT     = no
.available/CHEMICAL_SHIFT  = no
.available/FILTER/GAUSS= YES /HANNING= YES /FERMI= YES /default=none
.available/INTERPOLATIONS/SINC= no  /default=none
.available/MATRIX/SQUARE= YES /RECTANGULAR= no /HALF_FOURIER_ISO = no
.available/MATRIX/EXTENDED= YES
!
!   .dialog       parameters for the  dialog choices in NUMARIS
!
.dialog/SEQUENCE_STRING = SE
.dialog/MATRIX_TO_CALC /min=       8/max=    1024/inc= BASE2  /def=      256
.dialog/LINES          /min=       8/max=     128/inc= BASE2  /def=      256
.dialog/COLUMNS        /min=     256/max=     512/inc= BASE2  /def=      128
.dialog/ACQUISITIONS   /min=       1/max=     512/inc= BASE2  /def=        1
.dialog/3D_PART_THICKNESS/min=   0.100
.dialog/3D_PARTITIONS    /min=       4
.dialog/TR     /num=  1/min=  135000/max=20000000/inc=    1000
.dialog/TI     /num=  1/min=       0/max=       0/inc=       0
.dialog/TE     /num=  1/min=       0/max= 1000000/inc=    1000
.dialog/SLICES         /min=       1/max=       1/inc=       1
.dialog/SLICE_THICK    /min=  20.000/max=  20.000/inc=   1.000
.dialog/SLICE_DIST     /min=   0.000/max=  99.000/inc=   0.010
.dialog/ZOOM_FACTOR    /min=   1.000/max=   3.000/inc=   0.010
.dialog/PARAXIAL_ANGLE / none
.dialog/SAMPLE_INTERVAL/min=       0/max=       0/inc=       0
.dialog/PREPARING_SCANS/min=       1/max=      20/inc=       1/def=        6
.dialog/FLIP_ANGLE_ALPHA /none
.dialog/RF_BAND_WIDTH  /none
.dialog/GATING_RATIO   /min=   0.100/max=   1.000/inc=   0.100/def=    0.200
.dialog/LINES_GATE_OPEN/min=       1/max=   65535/inc=       1/def=        1
!
!    .dps      (Data  Processing  System)  directives  for the
!              preprocessing and FFT software in the BSP & VAX
!
.dps/CALC_ALGO          = none
.dps/LOOP_STRUCTURE     = FID
.dps/LINE_FFT           = no
.dps/OFFSET_IGNORE      = no
```

```
.dps/NO_ME_COMBINATION = no
.dps/HALF_FOURIER      = no  /TYPE= none     /LINES_AFTER_ZERO=    8
.dps/ECHO_ALTERNATING  = no
.dps/DIRAC_ELIMINATION = no
.dps/3D_RESOLUTION_FFT = no
.dps/TIMEOUT_FACTOR    =   1.000
!
!
!
!
! .gradampl   the  logical  reference gradient amplitudes in  [mT/m] for
!           matrix 256, zoom factor 1.0, slice thickness 10 mm, FOV 50cm
!
.gradampl/GP=  1.566000/GR=  1.566000/GS= none
.gradampl/GS_MIN= none     /GS_MAX= none
!
!    .msc     parameters for the  Measurement and Sequence Controller
!
.msc/trigger/NUMBEROFSCANS=sliceloop
.msc/GRADIENT_DELAY_CORRECTION = no
.msc/PARAX_RAMPTIME_INCREMENT  = none
!
!
.ext/SRF/SL/mi=  2.0/ma= 20.0/GS= 2.000000/FI=[USER]SE_04D1_1.EXT
.external/     R_P_FILENAME = none
.external/GRAD_TAB_FILENAME = none
!
.adj/CHEM_SHIFT_MAX_TIME =     0
.adj/READOUT_TIME =  128000
!
!
!=========================== sequence timing ============================!
.TIMINGTABLE
!Time/ | RF-Cabinet| ADC |     Gradient references     |Sync-|Relative
! usec |  01 |  02 |     |phasecode| readout |selection| Bits|  Time
!
.do /OFFSET /REP=  1                ! offset correction measurement  +
   1000                                                OSCO      1000
   3000                                                          4000
 256000             ON                                         260000
  50000                                                        310000
.end                                ! offset correction measurement  +
!
.do /LINES                          ! fourier lines loop - - - - - - +
.do /ACQUISITIONS                   ! acquisitions loop  - - - - - - +
.do /3DPARTITIONS                   ! 3D partition loop  - - - - - - +
.do /PREPARE                        ! prepare the inner loops  * - - +
.do /SLICES                         ! slice loop, I=SLICE/SERIES - - +
    540                                       PULS01    OSCO      540
    640 SRF01                                 PULS01             1180
    540                     TAB01    TAB02                       1720
    910                                       PULS02             2630
    835                                                          3465
 128000             ON                                         131465
   3535                                                        135000
TRFIL01                                                             !
.end                                ! slice loop - - - - - - - - - - +
.end                                ! prepare loop - + * + - + * + - +
.end                                ! 3D partition loop  - - - - - - +
.end                                ! acquisitions loop  - - - - - - +
```

```
                                        ! fourier lines loop - - - - - - +
.end
.END / TIMINGTABLE
!
!======================== rf types definitions ==========================!
.RFTABLE
!RFType|Sli-|Flip |Phase|Altern.| Scale |Empirical|Atten-|Supp-| Calc.
!Name  | ce |angle|angle| code  |pointer| factor  |uator | pts.|algorithm
SRF01   I     90    90     ++       1    1.0000000   1     256       5
.END / RFTABLE
!
!
!
!====================== gradient table definitions ======================!
.GRADTABLE
!TAB-| Steps |          Amplitudes          |Calc| RAMP-UP-params |RAMP-DOWN-params
!Name|through|  First |  Last   | Offset |algo|algo|samp| time |algo|samp| time
TAB01  LINES  #-1.3480 #1.34800 0.000000 NORM NORM   30   540  NORM   30    540
TAB02    30   #-1.3480 #1.34300 0.000000 NORM NORM   30   540  NORM   30    540
.END / GRADTABLE
!
!===================== gradient pulse definitions ======================!
.PULSETABLE
!Pulse| pulse    | RAMP-UP-params |RAMP-DOWN-params
!Name |amplitude|algo|samp| time |algo|samp| time
PULS01 #3.150000 NORM   30    540 NORM   30    540
PULS02 #-2.90000 NORM   30    540 NORM   30    540
.END / PULSETABLE
!
.END
```

Appendix 4

Patient Safety Checklist

	Avez-vous-Do you have:	oui-yes	non-no
1-	Un stimulateur cardiaque(pacemaker) ou autre appareil électronique? A heart pacemaker or other implanted electronic device?	☐	☐
2-	Une prothèse valvaire dans le coeur? An artificial heart valve?	☐	☐
3-	Une lentille prosthétique dans un oeil? An artificial eye lens (for cataracts)?	☐	☐
4-	Une implantation chirurgicale dans une oreille? A middle ear surgical implant?	☐	☐
5-	Des fragments métalliques dans la tête ou près des yeux? Any metal fragments in your head or near your eyes?	☐	☐
6-	Un clip ou une greffe chirurgicale métallique dans la tête ou ailleur dans votre corps? Any metal surgical implant or clip in your head or elsewhere in your body? Si oui, où et pourquoi?-If yes, where and why?	☐	☐

Date (j/d-m/m-ay)	Signature

Appendix 5

High Resolution Proton Sequence

ARCOPCP.AU

```
------ FILE: ARCPCOP .AU

 ; CHAIN OF PRESAT
 ;            CPMG
 ;            COSY
 ;            PRESAT

  RE STANARP       ; .001 PARAMETERS FOR PRESAT
  IF STANARP
1 ZE
2 D1 HG S1
3 GO=2 DO
4 WR #1
  RE STANARP       ; .002 PARAMETERS FOR CPMG
  IF STANARP
5 ZE
6 D1 HG S1
7 P1 PH1
8 D2
9 P2 PH2
10 D2
11 LO TO 8 TIMES C
12 GO=6 DO PH3
13 WR #2
14 IF #2
15 VC
16 LO TO 5 TIMES 28
   RE STANARP      ; .003 PARAMETERS FOR COSY
   IF STANARP
17 ZE
18 D1 HG S1
19 P1 PH4
20 D0
21 D3
22 P1 PH5
23 D3
24 GO=18 PH6 DO
25 WR #3
26 IF #3
27 IN=17
   RE STANARP      ; .004 PARAMETERS FOR PRESAT
28 ZE
29 D1 HG S1
30 GO=29 DO
31 WR #4
32 IF #4
33 IN=28
EXIT
PH1=A0 A0 A2 A2 A1 A1 A3 A3
PH2=A1 A3 A3 A1 A0 A2 A2 A0
PH3=R0 R0 R2 R2 R1 R1 R3 R3
PH4=A0 A0 A0 A0 A1 A1 A1 A1
    A2 A2 A2 A2 A3 A3 A3 A3
PH5=A0 A2 A1 A3 A1 A3 A2 A0
    A1 A3 A2 A0 A2 A0 A3 A1
PH6=R0 R0 R2 R2 R1 R1 R3 R3
```

References

(1) Cadoux-Hudson, T. A. D., Blackledge, M. J., Rajagopalan, B., Taylor, D. J., Radda, G. K., Br. J. Cancer 60, 430, (1989).

(2) Maris, J. M. and Chance, B., Mag. Res. Ann. 213, (1986).

(3) Mountford, C. E., Delikatny, E. J., Dyne, M., Holmes, K. T., MacKinnon, W. B., Ford, R., Hunter, J. C., Truskett, I. D., and Russell, P., Mag. Res. in Med. 13, 324, (1990).

(4) Daly, P. F. and Cohen, J. S., Cancer Research 49, 770, (1989).

(5) Negendank, W. G., Crowley, M. G., Ryan, J. R., Keller, N. A. and Evelhock, J. L., Radiology 173, 181, (1989).

(6) Arnold, D. L, Emrich, J. F., Shoubridge, E. A., Villemure, J., and Feindel, W., J. Neurosurg. 74, 447, (1991).

(7) Treatment of Glioma, ed. Jiro Suzuki, (New York: Springer-Verlag, 1988).

(8) Mineura, K., "Statistical Considerations of Therapeutic Results in Glioblastoma" p. 17 in Treatment of Glioma, ed. Jiro Suzuki, (New York: Springer-Verlag, 1988).

(9) Leibel, S. A., and Sheline, G. E., "Radiotherapy in the treatment of cerebral astrocytomas" p. 193 in Neuro-Oncology primary malignant brain tumours ed. D. G. T. Thomas, (Baltimore: The Johns Hopkins University Press, 1990).

(10) Kallio, M., Sankila, R., Jaaskelainen, J., Karjalainen, S., and Hakulinen, T., Cancer 68: 1394, (1991).

(11) Shingai, J. and Kanno, M. "Clinical Analysis of Glioma: Anaplastic Astrocytoma and Glioblastoma" p. 153 in Treatment of Glioma, ed. Jiro Suzuki, (New York: Springer-Verlag, 1988).

(12) Ben-Shlomo, Y. and Smith, G. D., Lancet, November 25, 1989.

(13) Stedman's Medical Dictionary 21st Edition, (Baltimore: The Williams & Wilkins Company, 1966).

(13) Stedman's Medical Dictionary 21st Edition, (Baltimore: The Williams & Wilkins Company, 1966).

(14) Zulch, K. L., Histological Typing of Tumours of the Central Nervous System, (Geneva: World Health Organization, 1979).

(15) Barnard, R. O., "The classification of intracranial tumours" p. 77 in Neuro-Oncology primary malignant brain tumours ed. D. G. T. Thomas, (Baltimore: The Johns Hopkins University Press, 1990).

(16) Harrison's Principles of Internal Medicine 11th Edition, Ed. Eugenes Brawnwald et al, (Toronto: MacGraw-Hill Book Company, 1987).

(17) Duffy, P. E., Astrocytes: Normal, Reactive, and Neoplastic, (New York: Raven Press, 1983).

(18) Burger, P. C., "The Grading of Astrocytomas and Oligodendrogliomas" p.171 in Primary Brain Tumors A Review of Histologic Classification ed W.S. Fields (London: Springer - Verlag, 1989).

(19) Brucher, J. M., "Grading by WHO Classification" p. 181 in Primary Brain Tumors A Review of Histologic Classification ed. W.S. Fields (London: Springer - Verlag, 1989).

(20) Jellinger, K. A., "Biologic Behavior of Meningiomas" p. 231 in Primary Brain Tumors A Review of Histologic Classification ed W.S. Fields (London: Springer - Verlag, 1989).

(21) Cox, J. D., and Komaki, R., p.233 in Annual Clinical Conference on Cancer, Vol 28 Lung Cancer: Current Status and Prospects for the Future (The University of Texas, 1986).

(22) Sanders, J. K. M. and Hunter, B. K., Modern Spectroscopy A guide for Chemists (Oxford: Oxford University Press, 1987).

(23) Morris, P. G., Nuclear Magnetic Resonance Imaging in Medicine and Biology (Oxford: Oxford University Press, 1986).

(24) Sears, F. W., Zemansky, M. W. and Young, H. D., College Physics 5th edition (Don Mills: Addison-Wesley Publishing Company: , 1980).

(25) Madden, A., Leach, M. O., Sharp, J. C., Collins, D.J., and Easton, D., NMR in Biomed. 4, 1, (1991).

(26) Griffiths, J. R., Bhujwalla, A. Coombes, R. C., Maxwell, R. J., Widwood, C. J., Morgan, R. J., Nias, A. H. W., Perry, P., Prior, M., Prysor-Jones, R. A., Rodrigues, L. M., Stubbs, M. and Tozer, G. M., Annals New York Acad. Sciences 508, 183, (1987).

(27) Stubbs, M., Rodrigues, L. M. and Griffiths, J. R., Br. J. Cancer 60, 701, (1989).

(28) Ng, T., Majors, A. W., Vivjayakumar, S., Baldwin, N. J., Thomas, F. J., Koumoundouros, I., Taylor, M. E., Grundfest, S. F., Meaney, T. F., Tubbs, R. R. and Shin, K. H., Radiology 170, 875, (1989).

(29) Gadian, D., Eur. J. Cancer 27, 528, (1991).(22) Hida, K. et al, Mag. Res. in Med. 23, 31, (1992).

(30) Glonek, T., Kopp, S. J., Kot, E., Pettegrew, J. W., Harrison, W. H., and Cohen, M. M., J. Mag. Res. 67, 443, (1986).

(31) Kilby, P. M., Bolas, N. M. and Radda, G. K., Biochim. Biophys. Acta 1085, 257, (1991).

(32) Murphy, E. J., Rajagopalan, B., Brindle, K. M. and Radda, G. K., Rag. Res. in Med., 12, 282, (1989).

(33) Daly, P. F., Lyon, R. C., Faustino, P. J., Cohen, J. S., J. Biol. Chem., 262, 14875, (1987).

(34) Hida, K., Kwee, I. L. and Nakada, T., Mag. Res. in Med. 23, 31, (1992).

(35) Kwee, I. L. et al, NMR in Biomed. 4, 38, (1991).

(36) Glickson, J. D., Invest. Radiol. 24, 1011, (1989).

(37) Semmler, W., Gademann, G., Bachert-Baumann, P., Zabel, H., Lorenz, W. J. and van Kaick, G., Radiology 166, 533, (1988).

(38) Redmond, O. M., Stack, J. P., Dervan, P. A., Burson, B. J. Carney, D. N. and Ennis, J. T., Radiology 172, 811, (1989).

(39) Vogl, T., Peer, F., Schedel, H. Reiman, V., Holtmann, S. Rennschmid, C. Sauter, R. and Lissner, J. , Mag. Reson. Imaging 7, 425, (1989).

(40) McKenna, W. G., Lenkinski, R. E., Hendrix, R. A., Vogele, K. E. and Bloch, P., Cancer 64, 2069, (1989).

(41) Ackerman, J. J. H., Nature 283, 167, (1980).

(42) The Physics of Medical Imaging, ed. Steve Webb, (Bristol: IOP Publishing Ltd., 1988).

(43) Mareci, T. H. and Brooker, H. R., J. Mag. Res. 92, 229, (1991).

(44) Haselgrove, J. C., Subramanian, V. H., Leigh, J. S., Gyulai, L. and Chance, B., Science 220, 1170, (1983).

(45) Coutts, G. A., Bryant, D. J., Collins, A. G., Cox, I. J., Sargentoni, J. and Gadian, D. G., NMR in Biomed. 1, 190, (1989).

(46) Vigneron, D. B., Nelson, S. J., Nat, R., Murphy-Boesch, J., Kelley, D. A. C., Kessler, H. B., Brown, T. R. and Taylor, J. S., Radiology 177, 643, (1990).

(47) Pykett, I. L. and Rosen, B. R., Radiology 149, 197, (1983).

(48) Maudsley, A. A., Hilal, S. K., Simon, H. E. and Wittekoek, S., Radiology 153, 745, (1984).

(49) Lenkinsi, R. E., Holland and G. A., Allman, T., Radiology 169, 201, (1988).

(50) Cox, S. I. and Styles, P., J. Mag. Res. 40, 209, (1980).

(51) Styles, P. et al, Mag. Res. in Med. 2, 402, (1985).

(52) Ordridge, R. J., J. Mag. Res. 66, 283, (1986).

(53) Robitaille, P., Merkle, H., Sublett, E., Hendrich, K., Lew, B., Path, G., From, A. H. L., Bache, R. J., Garwood, M. and Ugurbil, K., Mag. Res. in Med. 10, 14, (1989).

(54) Nadler, J. V. and Cooper, J. R., J. of Neurochem. 19, 313, (1972).

(55) Lowry, O. H., Berger, S. J., Chi, M. M.-Y., Carter, J. G., Blackshaw and Outlaw, W., J. of Neurochem. 29, 959, (1977).

(56) Gill, S. S., Thomas, D. G. T., Van Bruggen, N., Gadian, D. G., Peden, C. J., Bell, J. B., Cox, I. J., Menon, D. K., Iles, R. A., Bryant, D. J. and Coutts, G. A., J. of Comp. Ass. Tomogr. 14, 497, (1990).

(57) Peden, C. J., Cowan, F. M., Bryant, D. J., Sargentoni, J., Cox, I. J., Menon, D. K., Dagian, D. G., Bell, J. D. and Dubowitz, J. of Comp. Ass. Tomogr. 14, 886, (1990).

(58) Peeling, J. and Sutherland, G., Mag. Res. in Med. 24, 123, (1992).

(59) Segebarth, C. M., Baleriaux, D. F., Luyten, P. R. and den Hollander, J. A., Mag. Res. in Med. 13, 62, (1990).

(60) Bruhn, H., Frahm, J., Gyngell, M. L., Merboldt, K. D., Hanicke, W., Sauter, R. and Hamburger, C., Radiology 172, 541, (1989).

(61) Arnold, D. L., Shoubridge, E. A., Villemure, J.-G. and Feindel, W., NMR in Biomed. 3, 184, (1990).

(62) Demaeral, P., Johannik, K., Van Hecke, P., Van Ongeval, C., Verellen, S., Marchal, G., Wilms, G., Plets, C., Goffin, J., Van Calenbergh, F., Lammens, M. and Baert, A. L., J. of Comp. Ass. Tomogr. 15, 67, (1991).

(63) Alger, J. R., Frank, J. A., Bizzi, A., Fulham, M. J., DeSouza, B. X., Duhaney, M. O., Inscoe, S. W., Black, J. L., van Zijl, P. C. M., Moonen, C. T. W. and Di Chiro, G., Radiology 177, 633, (1990).

(64) Sze, D.Y. and Jardetzky, O., Biochim. et Biophys. Acta 1054, 198, (1990).

(65) Sze, D.Y. and Jardetzky, O., Biochim. et Biophys. Acta 1054, 181, (1990).

(66) Mountford, C. E., Holmes, K. T. and Smith, I. C. P., Prog. in Clin. Biochem. and Med. 3, 74, (1986).

(67) Barrere, B., Peres, M., Gillet, B. Mergui, S., Beloeil, J. and Seylax J., FEBS 264, 198, (1990).

(68) Damadian, R., Science 171, 1151, (1971).

(69) Ling, G. N., Kolebic, T. and Damadian, R., Physiol. Chem. Phys. & Med. NMR 22, 1, (1990).

(70) Mountford, C. E., Wright, L. C., Holmes, K. T., Mackinnon, W. B., Gregory, P. and Fox, R. M., Science 226, 1415, (1984).

(71) Mountford, C. E., Mackinnon, W. B., Bloom, M., Burnell, E. E. and Smith, I. C. P., J. of Biochem. and Biophys. Meth. 9, 322, (1984).

(72) Mountford, C. E., May, G. L., Williams, P. G., Tattersall, M. H. N., Russel, P., Saunders, J. K., Holmes, K. T., Fox, R. M., Barr, J. R. and Smith, I. C. P., Lancet, March 22, 651, (1986).

(73) Bradamante, S., Barchiesi, E., Pilotti, S. and Borasi, G., Mag. Res. in Med. 8, 440, (1988).

(74) Negandank, W. G., personal communication.

(75) Brown, T. R. Buchthal, S. D., Murhy-Boesch, J., Nelson, S. J. and Taylor, J. S., 82, 629, (1989).

(76) Brown, T. R., Kincaid, B. M. and Ugurbil, K., Proc. Natl Acad. Sci. USA 79, 3523, (1982).

(77) Glazer, G. M., Smith, S. R., Chenevert, T. L., Martin, P. A., Stevens, A. N. and Edwards, R. H. T., NMR in Biomed. 1, 184, (1989).

(78) Mazzeo, A. R. and Levey, G. C., Mag. Res. in Med. 17, 483, (1991).

(79) Segebarth, C. M., Baleriaux, D. F., De Beer, R., Van Ormondt, D., Marien, A., Luyten, P. R., and den Hollander, J. A., Mag. Res. Med. 11, 349, (1989).

(80) Segebarth, C. M., Baleriaux, D. F., Arnold, D. L., Luyten, P. R., and den Hollander, J. A., Radiology 165, 215, (1987).

(81) Karczmar, G. S., Meterhoff, D. F., Speder, A., Valone, F., Wilkinson, M., Shine, N., Boska, M. D. and Weiner, Invest. Radiol. 24, 1020, (1989).

(82) Heindel, W., Bunke, J., Glathe, S., Steinbrich, W. and Mollevanger, L., J. of Comp. Assis. Tomogr. 12, 907, (1988).

(83) Oberhaensli, R. D., Bore, P. J., Rampling, R. P., Hilton-Jones, D., Hands, L. J. and Radda, G. K., Lancet, July 5, 1986.

(84) Ross, B. D., Tropp, J., Derby, K. A., Sugiura, S., Hawryszko, C., Jacques, D. B. and Ingram, M., J. of Comp. Ass. Tomogr. 13, 189, (1989).

(85) Hubesch, B., Marinier, S., Hetherington, H. P. Twieg, D. B., and Weiner, M. W., Invest. Radiol. 24, 1039, (1989).

(86) Thomsen, C., Jensen, K. E., Achten, E and Henriksen, O., Acta RAdiol. 29, 77, (1988).

(87) Merchant, T. E., Meneses, P., Gierke, L. W., Den Otter, W. and Glonek, T., Br. J. Cancer 63, 693, (1991).

(88) Kuesel, A. C., Kroft, T., Saunders, J. K., Prefontaine, M. Mikhael, M. and Smith, I. C. P., Mag. Res. in Med., in press, (1992).

(89) Delikatney, J., Hull, W. E. and Mountford, C. E., J. Mag. Res. 94, 563, (1991).

(90) Dr. H. Hugenholtz, personal communication.

(91) Feinden, W., Steude, U., Bise, K. and Gundisch, O., Neurosurg. Rev. 14, 51, (1991).

(92) Smith, I. C. P., Krot, T., Saunders, J. K. and Prefontaine, M., SMRM Abstract, 839, (1990).

(93) May, G. L., Wright, L. C., Holmes, K. T., Williams, P. G., Smith, I. C. P., Wright, P. E., Rox, R. M. and Mountford, C. E., J. of Biol. Chem. 261, 3048, (1986).

(94) Holmes, K. T. and Mountford, C. E., J. Mag. REs. 93, 407, (1991).

(95) Shagel, D. E., Dittmer, J. C. and Wilson, C. B., J. Neurochem. 14, 789, (1967).

(96) Remy, C., Von Kienlin, M., Lotito, S., Francois, A., Benabid, A. L. and Decorps, M., Mag. Res. in Med. 9, 395, (1989).

(97) Langkowski, J. H., Sieland, J., Bomdork, H., Leibfritz, D., Wesphal, M., Offermann, W., and Maas, R., Mag. Res. Imaging 7, 547, (1989).

(98) Luyten, P. R., Marien, J. H., Heindel, W., van Gerwen, P. H. J., Herholz, K., den Hollander, J. A., Friedmann, G., and Heiss, W., Radiology 176, 791, (1990).

(99) Henriksen, O., Larsson, H. and Jensen, K. M., Acta Raiologica 31, 181, (1990).

(100) Prinz, E. MSc. thesis, 1989.

(101) Smith, I. C. P., Princz, E. J. and Saunders, J. K., J. Can Assoc. Radiol. 41, 32, (1990).

(102) Evanochko, W. T., Sakai, T. T., Ng. T. C. Krishna, N. R., Kim, H. D., Zeidler, B., Ghanta, K., Brockman, R. W., Schiffer, L. M., Graunschwieger, P. G. and Glickson, J. D., Biochim. Biophys. Acta 805, 104, (1984).

(103) Fan, T. W.-M., Higashi, R. M., Lane, A. N. and Jardetzky, O., Biochim Biophys. Acta 882, 154, (1986).

(104) Petroff, O. A. C., Spencer, D. D., Alger, J. R., Prichard, J. W., Neurology 39, 1197, (1989).

(105) Arnold, D. L., Shoubridge, E. A. , Emrich, J., Feindel, W. and Villmure, J., Invest. Radiol. 24, 958, (1989).